2007

Development of the new physical method for real time spot weld quality evaluation using ultrasound

Andriy M. Chertov
University of Windsor

Development of the New Physical Method for Real Time Spot Weld Quality Evaluation Using Ultrasound

By

Andriy M. Chertov

A Dissertation
Submitted to the Faculty of Graduate Studies
Through Physics
In Partial Fulfillment of the Requirements for
The Degree of Doctor of Philosophy in Physics at the
University of Windsor

Windsor, Ontario, Canada

2007

© 2007 Andriy M. Chertov

Canada

Abstract

Since the invention of resistance spot welding, the manufacturers have been concerned about the quality assurance of the joints. One of the most promising directions in quality inspection is the real time ultrasonic nondestructive evaluation. In such a system, the acoustic signals are sent through the spot weld during welding and then analyzed to characterize the quality of the joint. Many research groups are currently working to develop a reliable inspection method.

In this dissertation the new physical method of resistance spot weld quality monitoring is presented. It differs from all other ultrasonic methods by the physical principles of inspection. The multilayered structure of the spot weld with varying physical properties is investigated with short pulses of longitudinal ultrasonic waves. Unlike other methods, the developed technology works in reflection mode. The waves bring back the information which, after careful analysis, can be used to evaluate the weld quality. The complex structure of the weldment modifies the waves in different ways which, makes it hard to accurately measure the physical properties of the weldment. The frequency-dependent attenuation of the sound, diffraction, and beam divergence – all contribute to the signal distraction. These factors are fully studied, and ways to minimize them are presented. After application of pattern recognition routines, the weld characteristics are submitted to fuzzy logic algorithm, and the weld is characterized.

The current level of the system development allowed the installation of two prototype machines at one assembly plant. The technology is now under thorough evaluation for robustness and accuracy in an industrial environment.

To My Family

Acknowledgements

I want to thank many people for their support and help in my pursuing the PhD Degree in Physics. Even if some of them are not mentioned here, their help is of great importance to me and sincerely appreciated.

I would like to express deep respect to my supervisor, Dr. Roman Gr. Maev, for his strong support and advice during my studies. His continuous belief in success and commitment in all endeavours encourage me and many other people he works with.

I express my gratitude to the members of the research team I am working with. Dr. Serge Titov, Dr. Alex Denisov, Dr. Fedar Severin, and many others continuously provide me the opportunity to get new experience and knowledge in different areas of physics and other sciences. The professionalism of the people making up the research team is really indisputable. This is truly a multidisciplinary community which is the pleasure to work in.

I would like to thank Dr. Randy Bowers (Dept. of Mechanical Engineering), Dr. Wladyslaw Kedzierski (Dept. of Physics), Dr. Elena Maeva (Dept. of Physics) for their role as my committee members.

I want to thank Mr. Vladimir Ekimov for his financial support which was provided throughout my studies for both Master and Doctoral degrees.

My special thanks to Mr. Lev Degtyar for his help during my first steps on the Canadian land.

I want to thank my parents for their belief, support and love they bring to me.

And I express my cordial thankfulness to my wife Yuliya and my sons Arseniy and Artyom for the inspiration, joy and love they bring in our home.

Table of Contents

List of Figures

x

List of Abbreviations

FT   Fourier Transform

HT   Hilbert Transform

TOF   Short Time Fourier Transform

STFT   Time of Flight

BUA   Broadband Ultrasonic Attenuation

CHAPTER I

Introduction

1. Foreword

Resistance spot welding is a common method of joining metal sheets. It is the cheap and easy-to-automate method of parts assembly. Spot welding is widely used in automotive industry to assemble auto bodies. The method employs two electrodes to squeeze the metal plates to be joined [1, 2, 3]. An electric current on the order of 10-20 kA runs through the electrodes and the plates and melts the bulk of the plates; the newly formed nugget upon solidification holds the plates together.

The assembly process is usually automated, and a single spot welder makes thousands of spot welds per day. Due to electrode cap degradation, the nugget size, which is the usual measure of the joint quality, slowly reduces from part to part. The weld produced in the beginning of the shift can be much bigger than that after several hours of welder operation. For this reason, selective quality check ups are the routine procedure at the plant.

There are many destructive and nondestructive ways to inspect the weld. Destructive testing is usually very labour intensive and does not allow use of the part after inspection. Nondestructive evaluation and testing (NDE and NDT) are much more beneficial and allow part usage after inspection. Also, they are faster and require less work. The use of ultrasonic methods for this purpose is widely accepted due to their simplicity and ease of application. The descriptions of many applications can be found in literature [3-25]. The newest direction in the research and development of the nondestructive methods for spot weld inspection is focused on real-time applications. Such applications are assumed to test every spot weld at the very moment of its manufacture. The realization of such methods promises considerable cost savings in time, labour and repairs. Implementation of such technology is very beneficial for the sheet assembly industry, and for this reason it is receiving significant attention from many R&D groups. Such well known organizations as Edison Welding Institute, GE, Bosch and others are developing resources to real time quality characterization.

1

The first attempts at real time weld characterization were made in 1960's when several research groups tried to implement the ultrasonic transducer to test the weld during its manufacture [26, 27, 28]. These attempts were abandoned due to the lack of proper electronics and technology at the time. Attempts continued in the late 1990's when the level of development of both computer and manufacturing technologies allowed the investigation processes to be handled more efficiently. The very nature of real time testing requires fast electronics and software, which became widely available only recently. The transducers are more powerful and efficient; the electronics is hundreds of times cheaper and readily available. The experimental setup with a PC, ADC board, pulser-receiver, and ultrasonic transducer can be readily assembled in any research lab; many kinds of setup configurations can be relatively easily designed. These improvements in all areas of technology became a major reason why such attempts have recently re-emerged and are being tried by different research teams.

The University of Windsor research group was one of many who attempted to solve such a challenging problem. After several years of intensive research, which started in 1997 the research group invented a revolutionary method of visualization of spot weld internal structure development at the moment of weld manufacturing. The method is currently covered by two US Patents [29, 30]. It allows one to see in real time the features that previously were possible to observe only implicitly through multiple destructive tests. Such features as the exact moment of melting start, degree of liquid metal penetration into the plates, and the thickness of the weld pool are made visible during the process of weld formation. The visualization of liquid pool growth and solidification speed is made real by this method; previously, these two features were not possible to observe or measure directly even through multiple destructive tests or other techniques. The method provides the means to observe several technologically important parameters either not available for measurement before or available only with enormous labour involvement. Both the sheet assembly industry and resistance spot weld research groups can benefit significantly from the method. For the former, it allows non-destructive and real time characterization of the weld quality; for the latter, it brings a completely new instrument to the research of spot weld formation processes.

The approach involves the integration of an ultrasonic transducer into the spot weld electrode to test the weld quality in real time. As the weld is produced, a series of ultrasonic waves is sent into the joint area. The wave reflected from the weld interior

returns information about both the interface locations and material properties at a specific moment. The analysis of the signals received at different moments allows one to build a picture of weld formation, which includes very important technological aspects of spot welding. Among the most critical are the moment of melting start, the thickness of liquid metal pool formed between the plates, the depth of liquid penetration, and the degree of electrode heating. The extraction of this information needs to be done completely automatically and virtually in real time in order to have control over the production process. If the average weld with gun positioning takes around 2-3 seconds, the weld quality interpretation needs to be done before the gun reaches the next weld spot, i.e. is faster than 2 seconds, and ideally within several milliseconds.

The investigated problem is a very challenging one from both academic and application standpoints. The physical picture of the process involves dynamic change of material properties, phase transformations, and sound propagation through the multilayered structure with inhomogeneous properties. Additionally, huge electric current and electromagnetic fields surround the investigated environment, which adds complexity to the studied setup. Deep understanding of many physical phenomena and their interactions is required to deal with the problem. The developed system for weld evaluation also brings many challenges for the developers from the engineering side. Specialists in microelectronics, software development, mechanical engineering, and ultrasonics are deeply involved in research and development of the technology. It is a very multidisciplinary problem which requires a broad knowledge in different areas of science.

The topic of the project is of high importance for both academia and industry. It helps develop a technology for which there is a very high demand in industry today. The problems being solved here are also in line with today's most studied branches of science and technology. For this reason the research is readily supported by institutions from both government and industry. The continued support received from NSERC and Chrysler for this project over many years confirms its importance and productivity.

3

2. Development of the Nondestructive Technologies

As the spot weld industry continues to develop and often use new materials, it requires methods of reliable nondestructive monitoring of spot welds. Numerous NDE methods are currently used in production, but new materials often require new evaluation approaches.

NDE technology is meant to replace time consuming and expensive destructive testing, which only provides selective inspection. The application of NDT equipment saves time, labour, and energy, and allows 100% joint testing instead of providing selective tests. As such, NDE is elevated to a completely new level of quality control in manufacturing. Such methods allow the operator to deal with the problem more efficiently and to find the flaw before it is too late to fix the part.

NDE methods for monitoring nugget formation include acoustic emission, ultrasonics, and monitoring of temperature and electrical properties such as resistance, voltage, and dissipated energy. Monitoring provides information about the quality of the product. The basic ideas of some techniques using measurements of temperature, linear expansion and acoustic emission signals, are reported in [31, 32]. Nondestructive methods such as thermal, electric, X-ray and eddy current are unable to distinguish "stick", or, poorly welded, welds from good quality welds. Ultrasonic methods using the pulse-echo technique have shown reliability in this matter and have been implemented in manufacturing operations since 1985. Development of high frequency broadband ultrasonic transducers enabled the extension of the method to test spot welds as thin as 0.5 mm.

Ultrasonic procedures for spot weld evaluation after welding on cold products are well described [33-37]. They consist of a pulsed elastic wave excitation directed perpendicularly to the surface of welded sheets and reception of a series of elastic pulses reflected at the acoustical interfaces. Conclusions about the weld quality are reached by analyzing acquired pulse-echo patterns. This technique makes it feasible to distinguish between 4 configurations (good weld, undersize weld, stick weld and no weld). The above method gives an integral *a posteriori* estimation of the spot weld quality, but does not allow feedback into the welding procedure. A modified pulse-echo technique using a masked broadband transducer is described in [37].

4

Advanced techniques based on the application of acoustic microscopy methods have been recently reported. A cylindrically focused 20 MHz contact pick-up linear array probe has been used [38] to monitor the spot weld diameter. The main advantage of the device is that instead of mechanical scanning, electronic scanning is implemented. However, the uneven state of the nugget surface usually affects the obtained results.

Scanning acoustic microscopy allows a two-dimensional map of the spot weld to be obtained [39, 40]. An immersion focused transducer performs a C-scan in the plane parallel to the welded metal sheet surface, and the corresponding reflected signal amplitude distribution is recorded and visualized with good resolution. The major advantage of the method is the visual character of the welded area presentation, clearly distinguishing 'stick weld' and 'no weld' areas and welding flaws.

Real time ultrasonic NDE techniques, which measure the weld parameters during welding, are particularly advantageous because they permit feedback to adjust the welding parameters. This approach was investigated in a series of papers [22, 24, 25, 30, 41-45]. In [41, 42] elastic Lamb waves were used to obtain information about the weld nugget configuration and size. The method is based on real-time weld monitoring by measuring the amplitude of ultrasonic Lamb wave signals transmitted through the weld region. The transmitted signal is affected by temperature changes in the weld region during cooling and solidification of the molten pool. The time from weld current cutoff to the attenuation maximum, which corresponds to the temperature of the austenite-pearlite transformation, depends on the heat capacity of the molten pool and therefore can be related to the nugget size and the weld strength. The nugget size in this method is estimated indirectly, and various physical factors, such as the electrode pressure, acoustical and thermal damping of the electrodes, and steel sheet thickness variations can modify the cooling and in consequence give erroneous results.

Normal incidence ultrasonic transducers, i.e., those generating an acoustic beam perpendicular to the metal sheet surface, mounted in the welding electrodes may have some advantages in comparison to the Lamb wave technique, due to the direct estimation of the nugget configuration (cross section and thickness). The scheme using the through-transmitted signal was first applied in 1965 for the monitoring of aluminum spot weld nugget growth [43]. Two 5 MHz X-cut quartz elements were glued directly inside the electrodes, and the through-transmitted signal amplitude was monitored during welding. Initially the transmitted signal is close to zero; then it increases due to the applied

5

pressure, and then remains constant until the welding current starts. The signal drops abruptly due to the increase in the ultrasonic wave attenuation in heated metal. As the molten pool starts to grow, so does the through-transmitted signal. As the temperature of the molten metal increases, the attenuation of the signal increases again. After the current cutoff, the welded metal begins to cool and the ultrasonic amplitude first increases; when crystallization begins, the ultrasonic attenuation grows again. The maximum height of the signal was plotted with respect to the measured nugget diameter; a good correlation between the ultrasonic signal height and the nugget diameter has been obtained. Similar technical aspects of the same method are also discussed [44-46].

Transmission techniques can, in theory, be particularly advantageous when using normal incidence shear waves. The advantages in employing shear waves are:

• Lower sound velocity and thus higher spatial (frontal and lateral) resolution;

• Total reflection of normal incidence shear waves from the 'solid-liquid' interface;

• Better sensitivity to stick weld interface detection.

The molten nugget should primarily reflect the normal incidence shear wave beam created by one of the transducers and thus produce an intense shadow on the receiver, which drastically diminishes the received signal. It is important to note that a stick weld does not shadow the beam. However, some researchers have reported no significant advantage of shear waves despite the theoretical 100 percent reflectivity at the interface [47, 48]. Reduced reflected ultrasonic signals and the 'liquid-solid' interface roughness have been also observed. Apparently two factors are present: temperature attenuation effects are more severe for shear than for longitudinal waves, and due to dendritic grain growth the solid-liquid interface appears to be rough, which significantly modifies reflection-refraction coefficients.

A pulse-echo technique was applied for molten pool geometry evaluation using longitudinal waves [18]. No significant difference was observed in reflected signal amplitude between shear and longitudinal waves. The shear wave attenuation coefficient in metals is about 3-5 times greater than that of longitudinal waves, so that shear waves are usually used at lower frequencies rather than longitudinal waves.

Direct implementation of the above mentioned techniques in the manufacturing process is not straightforward, due to extremely severe thermal and mechanical exposures of welding electrodes, technical constraints of the welding electrode-holder assembly, and possible pressure and temperature variations during welding time. Only a few techniques

6

have been implemented on the industrial floor and their accuracy still needs to be improved.

The research and development of the ultrasonic weld quality monitoring system started in University of Windsor lab in 1998. The approach to solving this problem involves installation of the ultrasonic transducers in the weld gun electrodes in order to test the weld in real time. The ultrasonic waves penetrate the welded plates during welding and are modified by the medium on their way through it.

Initially, the attempts of the research team concentrated on the study of through-transmission mode using longitudinal waves. They involved the use of one transducer as an emitter of the waves and another as the receiver. The delay of the transmitted signal is modified by the heated medium. The signal time of flight (TOF) is directly proportional to the degree of material heating. The creation of the correlation curves based on the comparison of the weld size and corresponding TOF value allowed the prediction of the weld size.

Later, the reflection mode was tried in an attempt to reduce the setup complexity (less one transducer) and to find new characteristic parameters. The research on the reflection mode led to the invention of a totally new way of weld quality characterization. Besides the ability to measure the TOF parameter and predict the weld size, the method allowed the visualization of the formation of the liquid nugget. This discovery brought the method to the next step on the reliability hierarchy. The visibility of the nugget formation changes the status of the method from prediction to measurement method. In the first case, the TOF can only implicitly predict the size based on the integral delay on the way through the heated plates. In the second, reflection mode, the visibility of the liquid nugget allows direct measurement of the degree of nugget penetration into the welded plates. The method no longer predicts but sees and measures the weld size.

Currently, the technology is protected by two US patents. The beta version of the real time weld quality monitoring system has been undergoing extensive trials at the DaimlerChrysler assembly plant in Windsor, Ontario since February 2005.

7

3. Scope of the Dissertation

In my MSc thesis, I have already investigated several aspects of the studied problem. The physics of weld nugget formation and sound wave propagation through it were fully studied and presented using both analytic and numerical approaches.

The investigations during my PhD program remain in the same vein of research. They form a logical continuation of the work done during my studies for the MSc degree. Though the basic subject and conceptual approaches are similar, the dissertation describes a new physical method of weld quality characterization. In particular, a very important part of my research is the development of a new way of monitoring the dynamics of spot weld formation using ultrasound in the reflection mode. The transition from transmission to reflection mode is an important step forward in the research. I have spent most of my time as a PhD researcher studying and developing this approach because it brings much more information about the investigated physical processes.

Chapter II provides the description of the setup. Typical ultrasonic scans of the weld are analyzed and the most informative parameters are discussed. The extracted ultrasonic parameters are used by special decision making algorithm to qualify the weld. These parameters reflect the physical processes taking place within the weldment. Most of the physical changes taking place in the material modify the ultrasonic wave one way or another. The wave that passes through such media "picks up" these changes and brings them back to the computer.

On top of "conventional" noise, which includes the white noise and unwanted reflections from the walls, the physical properties of the transducer and the media create additional mechanisms of signal distortion which affect correct localization of the signals and thus proper weld quality testing. Chapter III describes such mechanism, namely the frequency dependent attenuation, which changes the frequency content of the original wave.

Another effect arising due to the diffraction of the sound beam is considered in chapters V and VI. The analysis of the field created by a transducer of finite dimensions precedes these derivations in chapter IV. Both taking into account these considered effects as well as trying to suppress them increases the accuracy of measurements and weld characterization.

8

The process of weld quality interpretation based on the ultrasonic scan analysis involves several major software steps. These steps include signal filtering and image processing of the 2-dimensional B-scan, pattern recognition, pattern feature extraction and weld quality characterization. Chapter VII describes the major concepts of scan filtering and the pattern recognition procedure. The way of mapping multiple parameters characterizing the weld quality into a simple red-yellow-green scheme is presented. The mapping can be done using a fuzzy logic algorithm, and the example of applying this technique to two-parameter input is presented.

Conclusions and suggestions for future work for integrating the new technology into production summarize the paper.

References

1. *Review of resistance spot welding of steel sheets Part 1. Modelling and control of weld nugget formation*, by N. T. Williams and J. D. Parker. International Materials Reviews 2004, Vol. 49 No. 2.
2. *Review of resistance spot welding of steel sheets Part 2 Factors influencing electrode life*, by N. T. Williams and J. D. Parker. International Materials Reviews 2004, Vol. 49 No. 2.
3. H. Zhang, J. Senkara, *Resistance Welding: Fundamentals and Applications*. ISBN 0-8493-2346-0, CRC Press.
4. Pittaway R. G. Ultrasonic Testing of Resistance Spot Welds, Weld. Met. Fabr., 35, 1967, pp. 443-447.
5. Ultrasonic Testing Applications in Welding. Nondestructive Testing Handbook. Vol. 7, technical eds. A. S. Birks, R. E. Green, Jr., and ed. P. McIntire, ASNT (1991).
6. Nondestructive Evaluation and Quality Control. ASM Handbook Vol. 17, ASM International, (1989), pp. 597-600.
7. Mansour T.M. Ultrasonic Inspection of Spot Welds in Thin-gage steel. Materials Evaluation, 46 (1988) pp. 650-658.
8. J. Krautkramer, H. Krautkramer. Ultrasonic Testing of Materials. New York: Springer-Verlag, 1969.
9. H. Yuasa and K. Masazumi. Inspection Device for Spot Welded Nugget. Acoustical Imaging, Vol. 22, P. Tortoli and L. Masotti, eds. NY Plenum Press (1996), pp. 771-778.
10. T. Adams. Ultrasonic Microscope Aids In Spotting Unsound Welds. Welding Journal, Aug. 1984, pp. 47-48.
11. R. Gr. Maev, D. F. Watt, R. Pan, V. M. Levin, and K. I. Maslov. Development of High Resolution Ultrasonic Inspection methods for Welding Microdefectoscopy.
12. Acoustical Imaging, Vol. 22, P. Tortoli and L. Masotti, eds. NY Plenum Press (1996), pp. 779-783.

9

13. S.I. Rokhlin, M.C. Chan and L. Adler. Quantitative Evaluation of Spot Welds by Ultrasonic Waves. Review of Progress in QNDE, Vol. 3B, eds. D. O. Thompson and D. E. Chimenti, NY Plenum Press (1984), pp. 1229-1241.

14. S.I. Rokhlin, R. J. Mayhan and L. Adler. On-Line Ultrasonic Lamb Wave Monitoring of Spot Welds. Mater. Eval., 43, (1985), pp. 879-883.

15. G. E. Burbank, and W. D. Taylor. Ultrasonic In-Process Inspection Of Resistance Spot Welds. Supplement to the Welding Journal, May 1965, pp. 193-198.

16. Murray E. E. Ultrasonic in-Process Control of Spot Welding Quality. Materials Evaluation, 25 (1967) pp. 226-230.

17. Hall E. T., Crecraft D. I. NDT of Resistance Spot, Roll Spot Stitch and Seam Welds. Non Destructive Testing, 4 (1971) pp. 181-191.

18. D. I. Crecraft and G. Warner. Ultrasonic Evaluation of Electrical Resistance Spot Welds. Non-destructive Testing, February (1969), pp. 40-43.

19. C. Lynnworth, and E. H. Carnevale. Ultrasonic Testing of Solids at Elevated Temperatures. Proceedings of the Fifth International Conference on Nondestructive Testing, Queen's Printer, Ottawa (1969), pp. 300-307.

20. Lott, Ultrasonic Detection of Molten/Solid Interfaces of Weld Pools. Materials Evaluation, 42, March,1984, pp. 337-341.

21. **Andriy M.Chertov**, Roman Gr. Maev and Fedor M. Severin, *Acoustic Microscopy of Internal Structure of Resistance Spot Weld.* In IEEE Transactions on Ultrasonics, Ferroelectrics, and Frequency Control special Edition. Accepted for publication.

22. **Andrey M. Chertov**, Roman Gr. Maev, *Real-Time Quality Monitoring of Resistant Spot Weld Using Integrated Ultrasonic Weld Analyzer (RIWA)*. Poster at 29th International Symposium on Acoustical Imaging, April 16th-18th, 2007, Shonan Village Center(http://www.shonan-village.co.jp/english), Kanagawa, Japan.

23. Roman Gr. Maev, **Andrey M. Chertov**, Elena Maeva, Fedar M. Severin, *Acoustic Microscopy of Resistance Spot Welds.* Paper at 29th International Symposium on Acoustical Imaging, April 16th-18th, 2007, Shonan Village Center(http://www.shonan-village.co.jp/english), Kanagawa, Japan.

24. R.Gr. Maev, **A. M. Chertov**, L.Barsanti, G. Shu, *Real-Time Quality Monitoring of Resistance Spot Weld Using Integrated Ultrasonic Weld Analyzer (RIWA)*. The Automotive Industry Advancements with NDT Topical Conference will be held in Dearborn, Michigan, 16-17 May 2007.

25. **A. M. Chertov**, J. Norman, D. Gavrilov, R. Gr. Maev, *Evaluation of Spot Weld Formation as a Function of Degradation and Electrodes Relative Position Using Longitudinal Acoustic Wave Reflection Mode.* The Automotive Industry Advancements with NDT Topical Conference will be held in Dearborn, Michigan, 16-17 May 2007.

26. *Ultrasonic Method and Apparatus for Spot Weld Control.* Bilge at al. US Patent 4,711,984, 1987.

27. G. E. Burbank at al, *Ultrasonic In-Process Inspection of Resistance Spot Welds,* 4/1966.

28. A. Stiebel et al, *Monitoring & Control of Spot Weld Operations,* 1968.

29. *Transducer Built Into an Electrode.* R. Maev, A. Ptchelintsev, J. Mann., US Patent Number 6,297,467 B1, Date of Patent Oct.2, 2001.

30. *Ultrasonic In-Process Monitoring And Feedback Of Resistance Spot Weld Quality* submitted to the US Patent Office in June 2004, R. Gr. Maev, **A. M. Chertov** et al. US Patent Application 20060076321.

31. D.V. Dickinson. *Resistance Spot Welding in Metals Handbook.* 9th edition, ASM, 1983.

32. S. Gedeon, C. D. Sorensen, K. T. Ulrich, and T. W. Eagar, *Measurement of Dynamic Electrical and Mechanical Properties of Resistance Spot Welds.* Welding Journal, Dec. 1987, pp. 378-385.

33. Pittaway R. G. *Ultrasonic Testing of resistance Spot Welds*, Weld. Met. Fabr., 35, 1967, pp. 443-447.

34. *Ultrasonic Testing Applications in Welding.* Nondestructive Testing Handbook. Vol. 7, technical eds. A. S. Birks, R. E. Green, Jr., and ed. P. McIntire, ASNT (1991).

35. *Nondestructive Evaluation and Quality Control.* ASM Handbook Vol. 17, ASM International, (1989), pp. 597-600.

36. Mansour T.M. *Ultrasonic Inspection of Spot Welds in Thin-gage steel.* Materials Evaluation, 46 (1988) pp. 650-658.

37. J. Krautkramer, H. Krautkramer. *Ultrasonic Testing of Materials.* New York: Springer-Verlag, 1969.

38. H. Yuasa and K. Masazumi. *Inspection Device for Spot Welded Nugget.* Acoustical Imaging, Vol. 22, P. Tortoli and L. Masotti, eds. NY Plenum Press (1996), pp. 771-778.

39. T. Adams. *Ultrasonic Microscope Aids In Spotting Unsound Welds.* Welding Journal, Aug. 1984, pp. 47-48.

40. R. Gr. Maev, D. F. Watt, R. Pan, V. M. Levin, and K. I. Maslov. *Development of High Resolution Ultrasonic Inspection methods for Welding Microdefectoscopy.* Acoustical Imaging, Vol. 22, P. Tortoli and L. Masotti, eds. NY Plenum Press (1996), pp. 779-783.

41. S.I. Rokhlin, M.C. Chan and L. Adler. *Quantitative Evaluation of Spot Welds by Ultrasonic Waves.* Review of Progress in QNDE, Vol. 3B, eds. D. O. Thompson and D. E. Chimenti, NY Plenum Press (1984), pp. 1229-1241.

42. S.I. Rokhlin, R. J. Mayhan and L. Adler. *On-Line Ultrasonic Lamb Wave Monitoring of Spot Welds.* Mater. Eval., 43, (1985), pp. 879-883.

43. G. E. Burbank, and W. D. Taylor. *Ultrasonic In-Process Inspection Of Resistance Spot Welds.* Supplement to the Welding Journal, May 1965, pp. 193-198.

44. Murray E. E. *Ultrasonic in-Process Control of Spot Welding Quality.* Materials Evaluation, 25 (1967) pp. 226-230.

45. Hall E. T., Crecraft D. I. *NDT of Resistance Spot, Roll Spot Stitch and Seam Welds.* Non Destructive Testing, 4 (1971) pp. 181-191.

46. D. I. Crecraft and G. Warner. *Ultrasonic Evaluation of Electrical Resistance Spot Welds.* Non-destructive Testing, February (1969), pp. 40-43.

47. C. Lynnworth, and E. H. Carnevale. Ultrasonic *Testing of Solids at Elevated Temperatures.* Proceedings of the Fifth International Conference on Nondestructive Testing, Queen's Printer, Ottawa (1969), pp. 300-307.

48. Lott, *Ultrasonic Detection of Molten/Solid Interfaces of Weld Pools.* Materials Evaluation, 42, March,1984, pp. 337-341.

A. Chertov Publications List

1. **A. M. Chertov**, R.Gr. Maev, *Inverse Problem Solution to Find Real-Time Temperature Distribution Inside the Spot Weld Medium Using Ultrasound Time of Flight Methods.* Review of Progress in Quantitative Nondestructive Evaluation. 2003, pp. 1492-1498.

2. **Andriy Chertov**, Roman Gr. Maev, *Determination of Resistance Spot Weld Quality in Real Time Using Reflected Acoustic Waves. Comparison with Through-Transmission Mode.* 16th World Conference on Nondestructive Testing held in August 30 – September 3 2004 in Montreal, Canada.

3. **A. Chertov**, R. Maev, *Extraction of Straight Line Segments from Noisy Images as a Part of Pattern Recognition Procedure.* Advances in Signal Processing for NDE of Materials, Aug. 2-4 2005, University of Laval, Quebec City, Quebec, Canada.

4. **Andriy M. Chertov** and Roman Gr. Maev, *A One-dimensional Numerical Model of Acoustic Wave Propagation in a Multilayered Structure of a Resistance Spot Weld.* IEEE Transactions on Ultrasonics, Ferroelectrics, and Frequency Control Oct. 2005, Vol. 52, No. 10, pp. 1783-1790.

5. **Andriy M.Chertov**, Roman Gr. Maev and Fedor M. Severin, *Acoustic Microscopy of Internal Structure of Resistance Spot Weld.* In IEEE Transactions on Ultrasonics, Ferroelectrics, and Frequency Control special Edition. August 2007 VOLUME 54 NUMBER 8, pp. 1521-1529.

6. R. Gr. Maev, **A. M. Chertov** et al. *Ultrasonic In-Process Monitoring And Feedback Of Resistance Spot Weld Quality* submitted to the US Patent Office in June 2004, US Patent Application 20060076321.

7. **Andrey M. Chertov**, Roman Gr. Maev, *Real-Time Quality Monitoring of Resistance Spot Weld Using Integrated Ultrasonic Weld Analyzer (RIWA).* The Proceeding of the 29th International Symposium on Acoustical Imaging, (Ed. Iwaki Akiyama) April 16th-18th, 2007, Shonan Village Center(http://www.shonan-village.co.jp/english), Kanagawa, Japan. Springer Verlag GmbH (in print).

8. Roman Gr. Maev, **Andrey M. Chertov**, Elena Maeva, Fedar M. Severin, *Acoustic Microscopy of Resistance Spot Welds.* The Proceeding of the 29th International Symposium on Acoustical Imaging, (Ed. Iwaki Akiyama) April 16th-18th, 2007, Shonan Village Center(http://www.shonan-village.co.jp/english), Kanagawa, Japan. Springer Verlag GmbH (in print).

9. R. Gr. Maev, **A. M. Chertov**, L.Barsanti, G. Shu, *Real-Time Quality Monitoring of Resistance Spot Weld Using Integrated Ultrasonic Weld Analyzer (RIWA).* The book of the Automotive Industry Advancements with NDT, ASNT Topical Conference, Dearborn, Michigan, 16-17 May 2007. Published by American Society of Nondestructive Testing.

10. **A. M. Chertov**, J. Norman, D. Gavrilov, R. Gr. Maev, *Evaluation of Spot Weld Formation as a Function of Degradation and Electrodes Relative Position Using Longitudinal Acoustic Wave Reflection Mode.* The book of the Automotive Industry Advancements with NDT, ASNT Topical Conference, Dearborn, Michigan, 16-17 May 2007, Published by American Society of Nondestructive Testing.

CHAPTER II

Problem Statement and Systematization of the Experimental Results

1. Spot Weld Formation Process

Spot welding is a common and cheap way of joining two or more metal sheets together. The sheets are squeezed between two copper electrodes with the force in the range of 2-5 kN. Electric current (either AC or DC) is then sent through the electrodes. The typical values for current in steel welding lie in the range of 5-15 kA; for aluminum welding the current can reach 25-30 kA. The metal plates close the circuit and the current flows through them. As the electric resistance of the steel (steel is used in most cases, only limited number of aluminum plates) is about 8 times higher than that of copper, the Joule heat developed in the materials carrying electric current will be much higher in welded plates than in the copper electrodes. The developed heat is sufficient to melt the metal and form a liquid pool within the plates. The highest resistance along the current path is usually at the steel-steel interface. This resistance is even higher than the bulk steel resistance. This fact makes the faying interface a center of heat generation. Heat is also lost through conduction into the electrodes. These two effects ensure that the liquid pool is formed inside the plate stack-up. The pool grows from the faying interface; if the process is stopped in time, solidification of the molten region welds the plates together. The heating takes from 80 ms to 500 ms depending on plate thickness. Often, the weld time is measured in the units of $1/60^{th}$ s, cycles. The whole process with heating and cooling usually takes about 500-700 ms, which is less than a second per joint.

Only careful combination of welding parameters such as current, weld time, squeeze time and electrode force can ensure the production of good weld. Too low of a force will develop too high of a contact resistance, which can lead to the expulsion of molten metal from the joint. Too high of a force will prevent heat from being developed in the required amount. Too long or too short of a heating time can also degrade the weld formation. For these reasons, different destructive techniques are widely used today in production to ensure the good quality of the joints. Figure 1 shows several metallographic sections of spot welds obtained at different weld settings. Figure 2 presents another method of

13

destructive testing – the peel test. In either of these approaches, the diameter of the nugget is measured to qualify the joint. On the metallographic section, one can also see the penetration of the nugget into the welded plates. It is another measure of quality but is used less often due to the greater amount of labour involved in the inspection process.

14
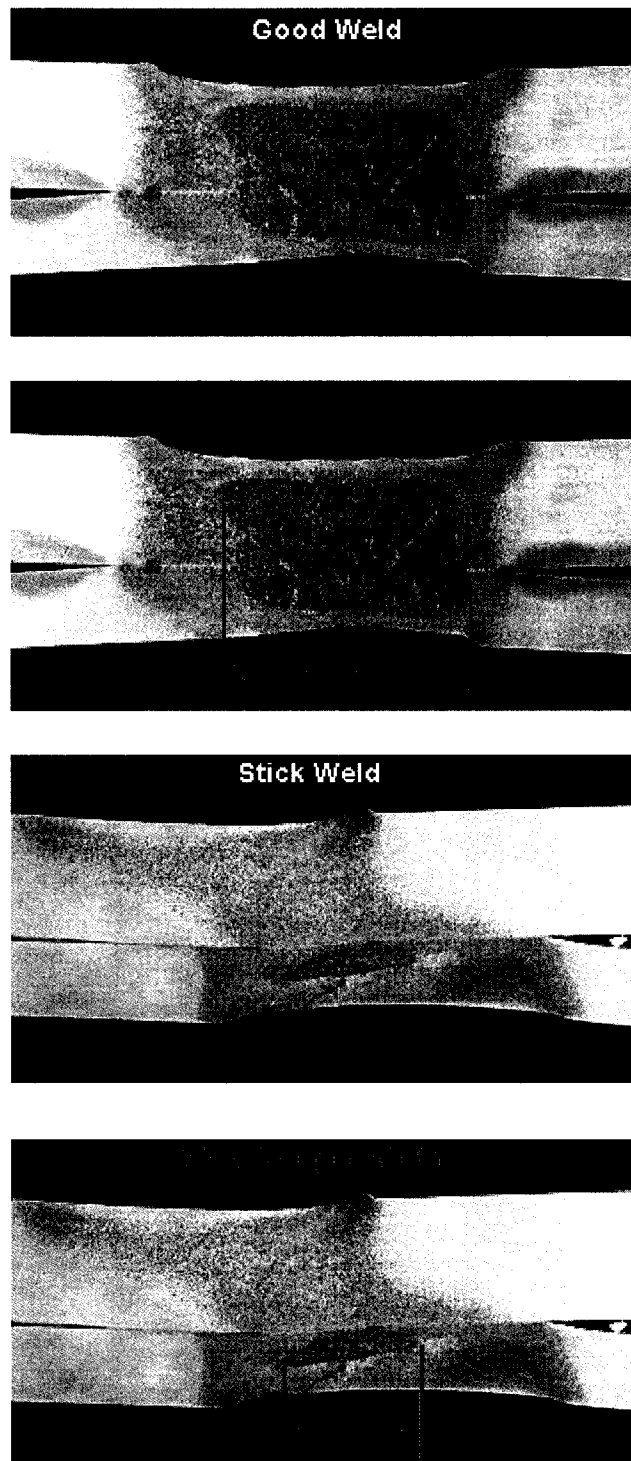
Figure 1. Metallographic cross-sectional views of welds. The top two pictures show a good weld and its effective size; the bottom two pictures show a bad weld with weak adhesion strength.
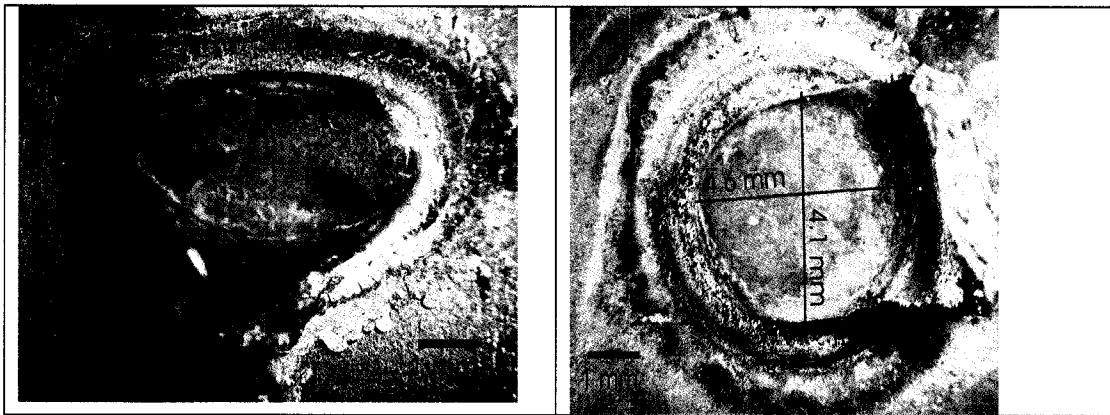
Figure 2. Peeled welds.

The numerical model of spot weld growth described in great detail in my MSc Thesis [3] helps visualize the process with 2-dimensional heat distribution patterns in such a setup, see Figure 3.

Cycle 1 Cycle 6 Cycle 11

Temperature, K

300   515   730   945   1160   1375   >1723
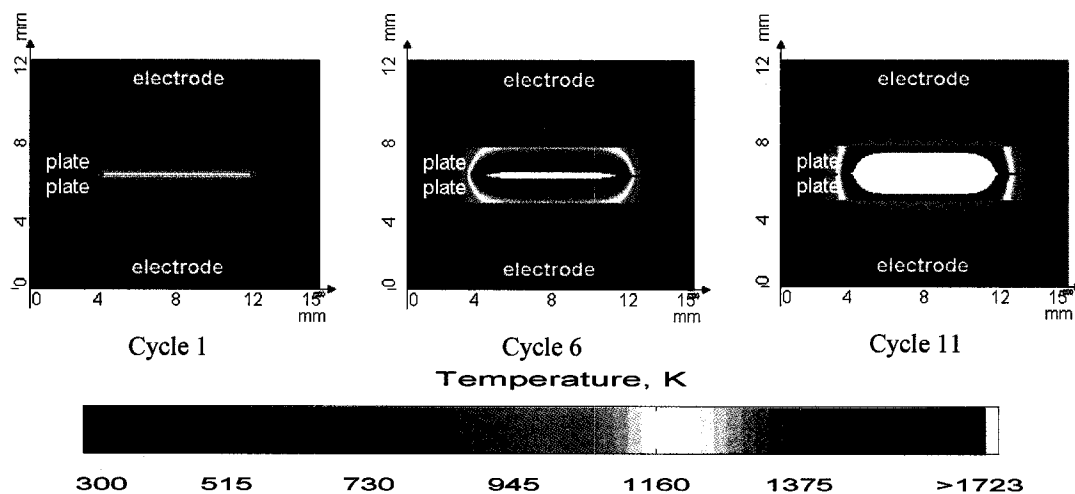
Figure 3. Finite difference model of heat distribution in electrodes and welded plates. Parameters used in the model: 1.5 mm thick mild steel plates., welding current – 14.5 kA, welding time – 12 cycles (60 Hz), tip diameter – 7.9 mm, electrode force – 900 lbs. Melting point of mild steel is taken 1723 K.

Upon turning off the current, the developed heat begins to dissipate into the surrounding plate material and electrodes. The molten metal solidifies and forms a nugget holding the plates together. The diameter of the nugget is often used as a measure of joint strength. Some standards define the acceptable diameter to be $4\sqrt{t}$, t being the thinnest plate thickness in millimeters.

In certain circumstances, the weld nugget can be produced undersized or no nugget can be formed at all. The common reasons for such a result include low current, insufficient weld time, electrode degradation or mushrooming caused by aging and

16

alloying. In the latter case, the current density drops due to tip face increase and does not provide enough heat within the volume.

The developed ultrasonic method is intended to detect the nugget formation and the nugget penetration degree into the plates in order to classify the weld as acceptable or unacceptable.

2. Description of the Method

The ultrasonic transducer is integrated into the weld gun electrode to send short pulses into the welded area. The ultrasonic transducer is immersed in the electrode cooling water, which is fed under pressure to the welding tip. It is mounted in a special housing, coaxially with the electrode, to send pulses through the water column, the copper weld cap, and right into the welded plates. The schematic view of the full arrangement is shown on Figure 4 (a). A PC controls the specially designed board capable of generating short electric pulses, which are later converted into mechanical oscillations by a piezoeffect, receiving the analog electric oscillations, converting them into digital form, and sending them to the computer. Figure 4 (b) presents a drawing of the transducer housing, which works as a part of the electrode body and conveys the cooling water to the weld cap. The housing secures the transducer and protects it from mechanical impact from the outside. The water flow is not altered upon transducer housing installation, and the cooling water reaches the weld cap without any complications. The design of the transducer developed by the University of Windsor research group is protected by a US patent [1]. Figure 4 (c) shows a photograph of the actual transducer installed in the upper weld gun jaw. In general, it makes no difference whether to install it on the upper or lower jaw, because the sound waves are not affected by gravity. The transducer housing is made of class 2 copper, which works as a part of the electric circuit conveying an electric current of some 10 kA to the welded plates. Also, the housing must be strong enough to withstand hundreds of thousands mechanical cycles of 3 to 5 kN. Thus, this transducer that is used in everyday work is virtually a state of the art piece of hardware, having enormous mechanical strength, conducting huge electrical currents, conveying cooling water to the tip, and containing a tiny piezoelectric crystal. This crystal converts an electrical pulse of around 200 V into sound waves, receives hundreds of times weaker vibrations, and converts them back into a weak electrical signal. This entire process

17

occurs while, on the outside of the transducer, an alternating electrical current of 10 kA with all of its associated electromagnetic fields.
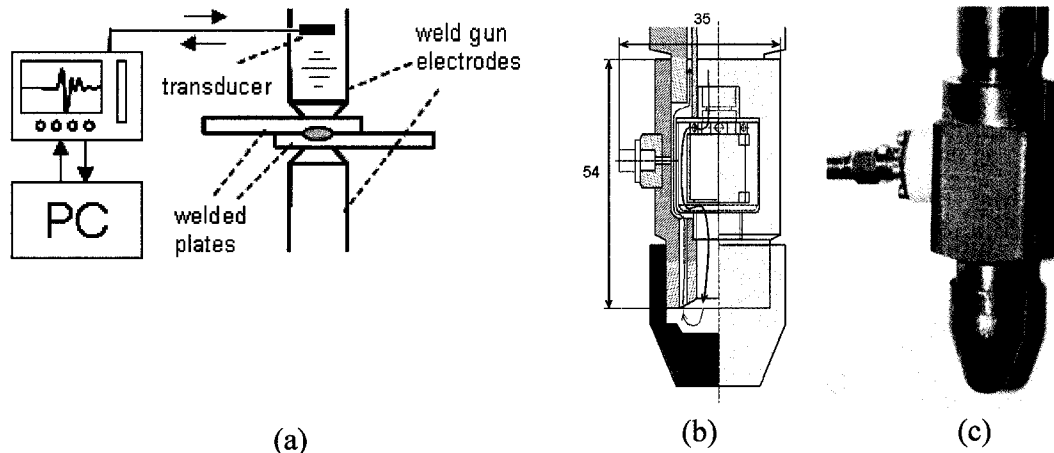
Figure 4. The view of the setup. (a) Schematic view of the arrangement; (b) schematic view of the transducer housing; (c) photo of the installed transducer.

A specially designed PC card is used as a pulser-receiver to generate and receive the ultrasonic pulses. The same card converts the received analog signal into digital format. A special software package runs the board and allows transfer of the data to the PC for further processing.

Mechanical oscillations, which are initiated by the piezo-crystal when it is excited by electrical oscillations, propagate through the cooling water, which acts as a couplant between the transducer and the investigated sample. Such mechanical oscillations are called sound or ultrasonic waves. The waves travel through the water column, they enter the copper layer of the welding cap, and then the welded plates. Within the welded plates (most frequently, two or three) the sound waves encounter a series of reflections from the internal structure of the weldment. Part of the acoustic energy goes further into the second electrode and is lost there. Another part reflects and brings back the information about the weld structure. These reflected waves need to repeat their way in the reverse order before they reach the receiver. In our setup the reflection mode is used; the same transducer is used as both emitter and receiver of the waves. It proved to be more practical to use the reflection mode, though the transmission mode is also a possible arrangement. The transmission mode, which was studied extensively [2-5], requires two transducers, which is often not possible to arrange due to the weld gun geometry, and does not carry as much information as the reflection mode. The reflection mode makes it possible to see the

18

interior of the spot weld at the exact moment of weld formation. This feature was previously available only through computer simulations. This invented method, which is protected by the US Patent [6], brought a completely new way both to monitor the processes within the welded plates during manufacturing, as well as to interpret the weld quality in real time.

3. Sound Waves within the Welded Plates

The resistance spot weld stack-up is a multilayered structure which includes the copper electrodes and welded plates as separate layers. When welding begins, the structure becomes even more complex as an additional layer of liquid metal forms, and each layer becomes highly inhomogeneous due to uneven temperature distribution. High temperature gradients create material properties gradients because all of the properties are the functions of temperature. Thus, the density, electric and thermal conductivity, sound speed, etc., are very unevenly distributed along the weldment profile.

As the sound wave penetrates the weldment it encounters a series of reflections. These reflections come from different interfaces between different media within the weldment. In general, for the 2-plate stack-up there can be up to five different reflections of interest. The reflected pulses come from copper-steel interface **1**, solid-liquid interface **2**, liquid-solid **3**, steel-copper **4**, steel-steel **5**. Thus, a series of reflections appear on the oscillogram also called the A-scan, part (b) of the Figure 5. Initially there are going to be reflections from the copper-steel interface, the steel-steel interface and the steel-copper interface. When melting starts, the steel-steel interface disappears, effectively splitting into two solid-liquid and liquid-solid interfaces. This happens because the highest rate of heat generation is at the steel-steel (faying) interface. It has the highest contact resistance, exceeding both the copper-steel contact resistance and also the bulk resistance of steel. The central contact begins to melt first, and the liquid steel spreads towards the outer boundaries of the plates.

19
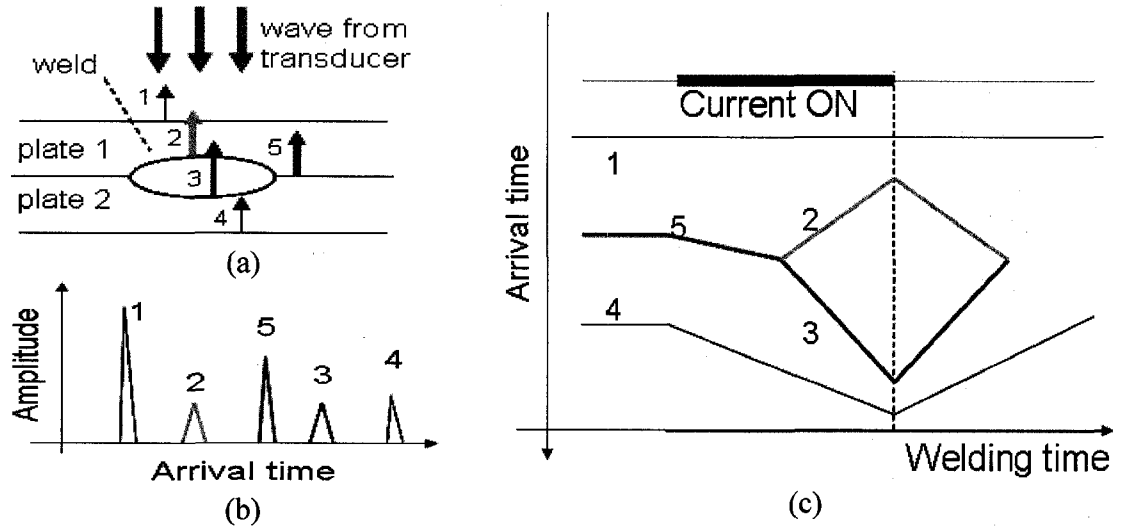
Figure 5. Formation of the weld signature. (a) reflecting interfaces of the spot weld; (b) A-scan of weldment reflections; (c) B-scan (combination of A-scans).

In my MSc thesis, the finite difference model of the sound wave propagation within the multilayered system of the spot weld was developed [3, 8], Figure 6. It was developed in order to better understand the nature of the wave propagation and possible complications that might arise in such system due to interference of multiple reflections. The analysis has shown that the reverberations within the welded plates can be separated from the pattern of interest by proper setting of the time gates on the A-scans. Also, the interference should not cause too many problems in the weld investigation as long as the secondary and succeeding reflections lose a considerable amount of energy and do not modify the primary reflections much. The model shows the initial wave emitted by the transducer into the water, coming from the left and progressing to the right. Multiple reflections of different amplitudes arise from the acoustic impedance mismatch at the boundaries of different media. The equations for determining the transmission and reflection coefficients for wave pressure, T and R, respectively are shown below:

$$T = \frac{2Z_2}{Z_1 + Z_2}, \quad R = \frac{Z_2 - Z_1}{Z_2 + Z_1} \qquad Z_1, Z_2 \ \textit{are acoustic impedances of mediums.} \quad (1)$$

The transmission coefficient for pressure can be greater than 1 when the wave enters a medium with higher acoustic impedance. Upon reflection from a medium with lower impedance, the wave flips its phase. In this case, the reflection coefficient has negative sign as $Z_2 < Z_1$.

In the setup used, the ultrasonic pulses are sent one after another with some time separation. This time gap between adjacent A-scans is long enough for all reverberations

20

to die out before the next pulse is sent. The usual time gap is around 2-3 ms, while the process of pulse attenuation below the noise level takes an order of tens of microseconds. Thus, the adjacent A-scans do not overlap or interfere in any way. The A-scans can be put together to form a 2-dimensional image of the process of weld formation, Figure 5 (c), called an acoustical signature of the weld, sometimes, the B-scan or M-scan. The scans are arranged vertically, so that the horizontal axis represents welding time, and the vertical axis is the arrival time of different pulse reflections.
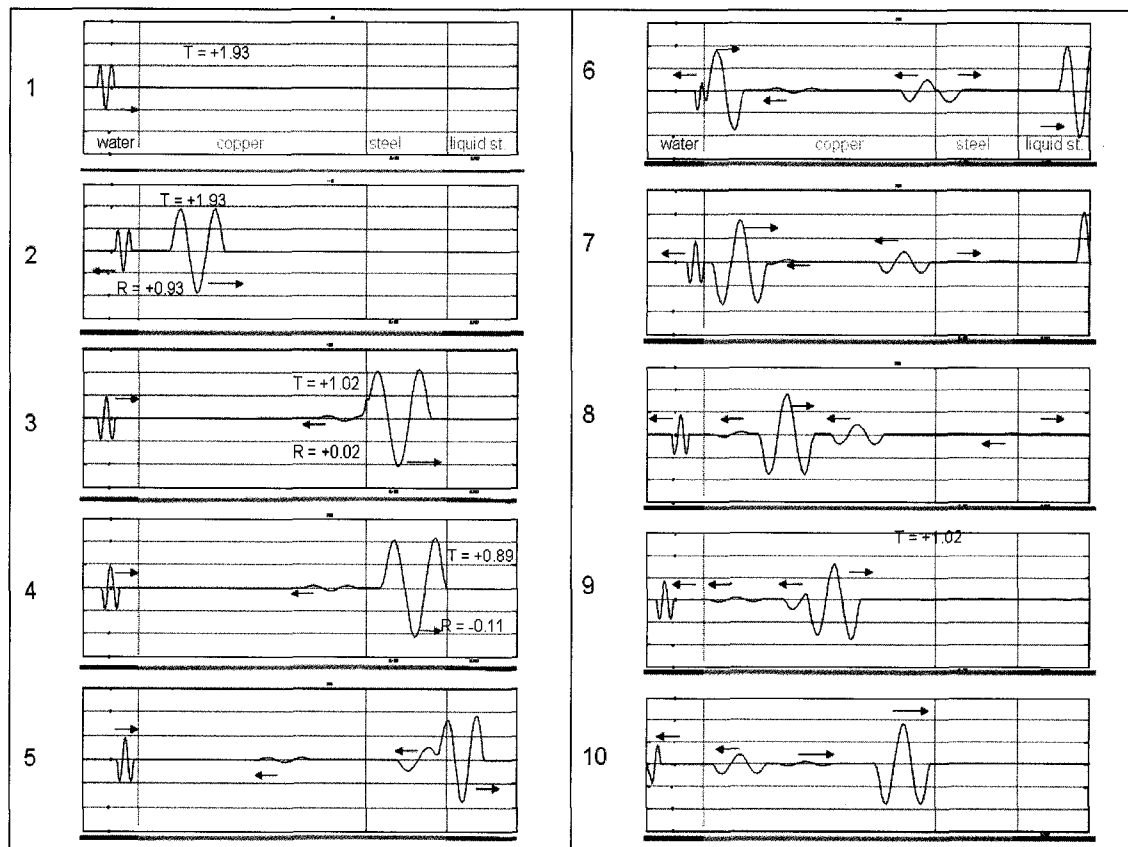
Figure 6. 1D model of the wave pressure passing through the stack-up of cooling water, electrode copper, solid steel layer and liquid steel layer. Minus in reflection coefficient denotes phase inversion on reflection.

The horizontal axis covers time of around 300-500 ms, which encompasses heating and cooling time, while the vertical one covers several microseconds. The scans are greyscale with a color resolution of 256. As the wave is quantized by 256 different voltage levels, every level is assigned its greyscale color. The highest peak will be white, and the lowest valley of the signal will be black. Noise in the level of 127-128 is represented by grey. A typical 2D scan is shown on Figure 7 (a). It is often called a B-scan, even though this term is more frequently used for mechanical scanning of the sample.

21
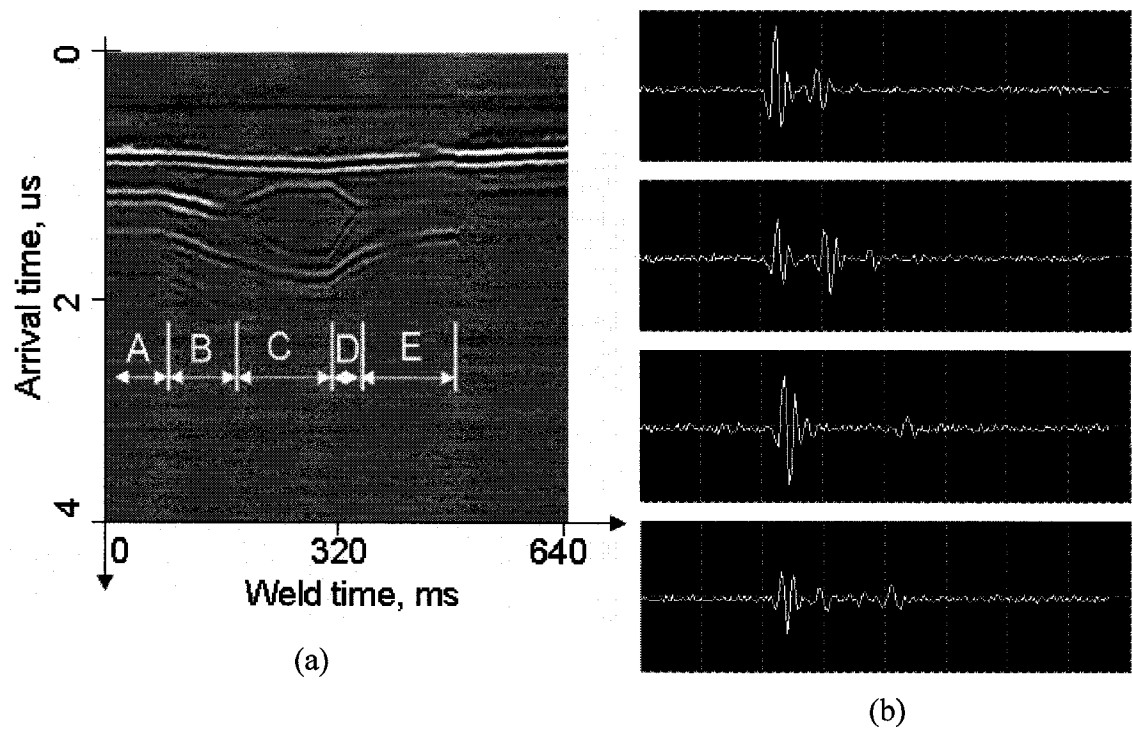
Figure 7. (a). Typical ultrasonic signature of the weld with five characteristic zones; (b). A-scans from zones A, B, C, D.

Figure 7 (a) shows the real image of the ultrasonic signature of the weld. One can make direct comparison of this figure with the schematic one on Figure 5 (c). The schematic figure does not use colors to define the signal amplitude, but only uses lines to show the relative positions of interfaces. The actual figure depicts the signal amplitude with color, thus showing some interfaces less clearly, though they exist and reflect the waves. Similar to the schematic picture, the upper interface represents the copper-steel contact; this is the first boundary that the signal strikes. The lowest, curved interface is the steel-copper contact, the last boundary in the sequence. Everything between these two curves takes place within the welded plates and brings information about the weld joint formation.

The first logical part of the signature, A, is referred to the time prior to the welding when the electrodes are already squeezed but no current is being sent yet. For this reason one can see only three lines arise from reflections off the copper-steel, steel-steel and steel-copper boundaries. One of the A-scans from this area is shown at the top of Figure 7 (b). The first reflection is the strongest and the following ones lose power as the signal energy splits into reflection and transmission parts at every boundary. As the current starts (border of zones A and B), the speed of sound in the heated metal gradually drops. Also, the thermal expansion of the metal makes the electrodes move apart. These two

22

effects make the ultrasonic wave return later as it requires more time to travel back and forth through the welded plates. This is reflected on the second logical part of the B-scan, *B*, – the longer we heat the plates the bigger the delay between the pulses on the vertical axis. One of the A-scans from the area *B* is presented on Figure 7 (b), second from the top. The rate of heating changes the slope of the lower curve. The higher the heating rate the bigger the slope; in the part *A* there is no heating and thus the slope is zero – the line is horizontal. According to calculations [3], the contribution of thermal expansion to the signal delay constitutes about 10-15% of the total delay. The rest is provided by the sound velocity drop caused by heating. Temperature increase in the mild steel reduces the longitudinal speed of sound by ~20% between room temperature and the melting point – from 5900 m/s to 4800 m/s [7].

The next interesting and informative part is the moment when melting initiates, beginning of zone *C*. Melting splits the steel-steel central interface into two boundaries. It is no longer a solid-solid steel-steel interface - there are now two solid-liquid interfaces along the path of the wave. The longer the heating lasts, the deeper the liquid pool penetrates into the welded plates – approaching the plate's outer surfaces towards the electrodes. The process of weld growth is visualized in real time. One of the A-scans from this area is the third from the top on Figure 7 (b). After the current is off, (beginning of zone *D*) the reverse process of cooling and solidification begins, areas *D* and *E*. The slope of the lower line changes its sign due to the thermal contraction and the increase of the sound speed in the cooler material. The liquid weld pool is shrinking towards the center as the majority of heat is usually lost into the electrodes, part *D*. Some part of the heat is lost by conduction into lateral areas of the plates; however, this rate is lower due to the much smaller cross-sectional area for heat flow and lower temperature gradients. The A-scan from area *D* is presented on the bottom of Figure 7 (b). Upon solidification, the lines 2 and 3 (see Figure 5 (c) for reference) meet and disappear as there is nothing to reflect from within the weld after solidification. Further cooling (area *E*) makes the lower curve approach the horizontal orientation. The abrupt disappearance of the lower curve at the end of zone *E* is due to the opening of the jaws on the spot welder. At this moment no signal penetrates the welded plate; thus only reflection off the copper-air interface is visible. The signature of the weld is acquired.

23

4. Analysis of the Weld Ultrasonic Scan

The signature of the spot weld (the B-scan) obtained in reflection mode carries significant information about the process taking place within the welded plates. Extensive research has been conducted on the analysis of different features extracted from the weld signature.

4.1. Time of Flight

One of the well studied parameters is the delay of the signal that passes through the welded plates and comes back to the receiver. Such a wave penetrates the welded plates and travels through the joint area twice, thus increasing its own delay and emphasising the effect. As was mentioned above, the main mechanisms causing this delay are the velocity drop and the thermal expansion of the plates. Statistical studies conducted on both transmission and reflection modes have shown very high correlation of the signal delay with the nugget diameter. This information can be directly used to provide an estimate of the weld nugget diameter without breaking the weld. Studies have been conducted both in the lab and in production at the DaimlerChrysler assembly plant in Windsor, Canada.

In the lab, the correlation of TOF with nugget diameter was tested with electrode misalignment and with different stages of cap degradation. The results are presented on Figure 8 and Figure 9. The correlation curves show the error in weld size prediction about 0.8 mm. For the nominal sizes of regular welds in the range of 4.0 to 6.0 mm this error in prediction is acceptable for reliable quality inspection. Figure 10 presents the results of the correlation tests obtained at the industrial floor. The auto body parts were removed from the line and destructively tested to check the nugget size. The corresponding measured diameters were related to the obtained ultrasonic data. Due to the irregular part geometry, the error in size prediction was a little higher – around 1.1 mm. The tests have shown good repeatability of the results with multiple tests performed for both applications.

24
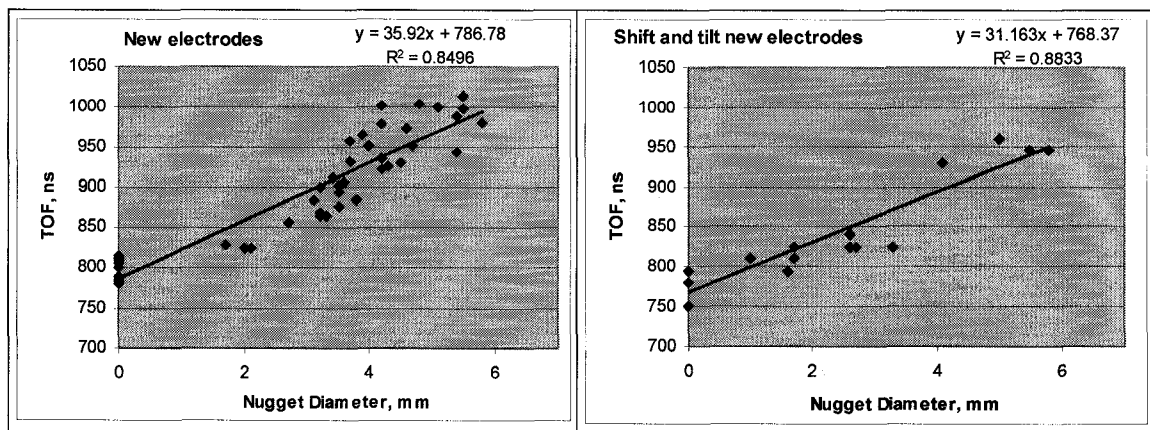
Figure 8. Correlation of nugget diameter with time of flight. Lab results. New well aligned electrodes and tilted electrodes (to model misalignment common at the plant).
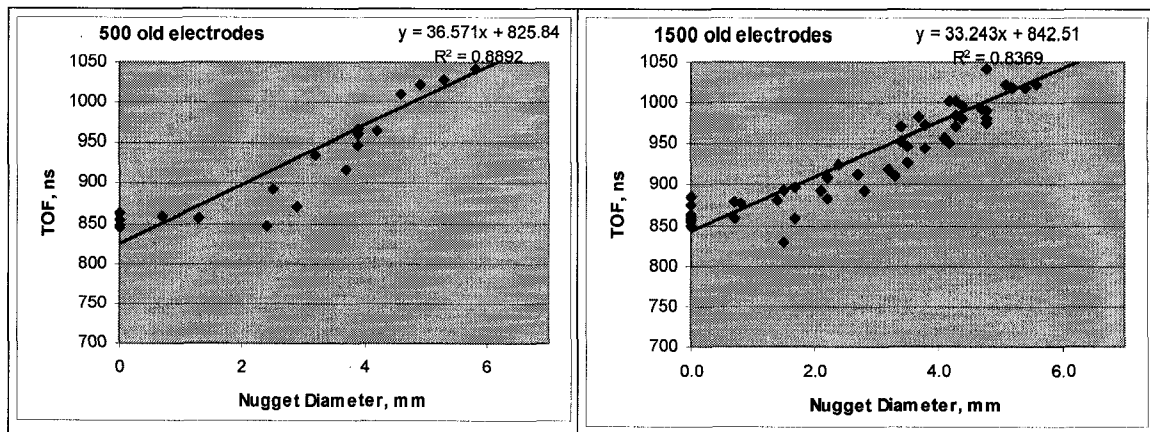
Figure 9. Correlation of nugget diameter with time of flight. Lab results. Degradation experiment.
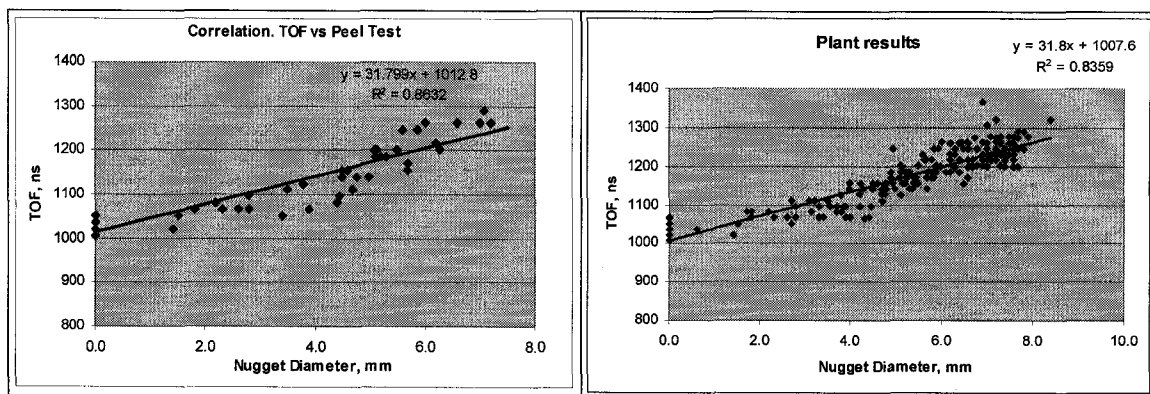
Figure 10. Correlation of nugget diameter with time of flight. Plant results. Two different weld guns.

4.2. Liquid Nugget Penetration

The second important parameter used in weld quality characterization is the degree of liquid penetration into the welded plates. The method enables the user to easily

25

distinguish the upper and lower boundaries of the liquid nugget as their large surface areas provide a good reflected signal. These reflections arise due to the acoustic impedance mismatch between the solid and liquid metals. Simple calculations can help predict the reflection coefficient of such an interface. The reflection coefficient defined in (1) requires the knowledge of impedances from both sides of the boundary.

$$Z = \rho \cdot c \tag{2}$$

where ρ is the density and c is the speed of sound in the medium. Assuming equal temperature from both sides of the boundary (T_{melt-}, T_{melt+}) and that the metal is solid from one side and liquid from another, the impedances take the following values:

$$Z_{solid} = 3.41 * 10^7 \text{ kg/m}^2 \text{/s}, \quad Z_{liquid} = 2.75 * 10^7 \text{ kg/m}^2 \text{/s}.$$

These values have been obtained using the following values for the mild steel density and sound speed near the melting point: $\rho_{solid} = 7100 \text{ kg/m}^3$, $\rho_{liquid} = 6800 \text{ kg/m}^3$, $c_{solid} = 4800 \text{ m/s}$, $c_{liquid} = 4050 \text{ m/s}$ [7]. Based on these data, the reflectivity coefficient for sound pressure at the mild steel solid-liquid interface can be estimated to be ~0.11. If the wave hits this interface from the solid steel side, the phase of the wave experiences a 180 degree shift. This feature can be observed on any B-scan when the interfaces are visible. For example, on Figure 7 (a) the solid-liquid interfaces in zone D with opposite phases are well visible.

In most of the cases, the maximum penetration of the liquid pool into the welded plate thickness occurs at the final moment of heating. This moment is routinely used to measure the liquid thickness. Upon solidification, the nugget takes the shape of the liquid to a big extent. There is of course, some shrinkage and post-welding deformation of the joint. But according to the studies using metallographic sections, the measured depth of liquid penetration corresponds very closely to the solid nugget penetration. Figure 11 (a) shows the schematic pattern of the weld signature and three distances which are directly related to the weld geometry in vertical direction. This geometry is presented at Figure 11 (b). Three d values determine the nugget state: $d1$ and $d2$ are the penetration levels. The lower these values the higher the penetration. $d3$ is the metal pool thickness. It defines the size of the nugget in vertical direction.

26
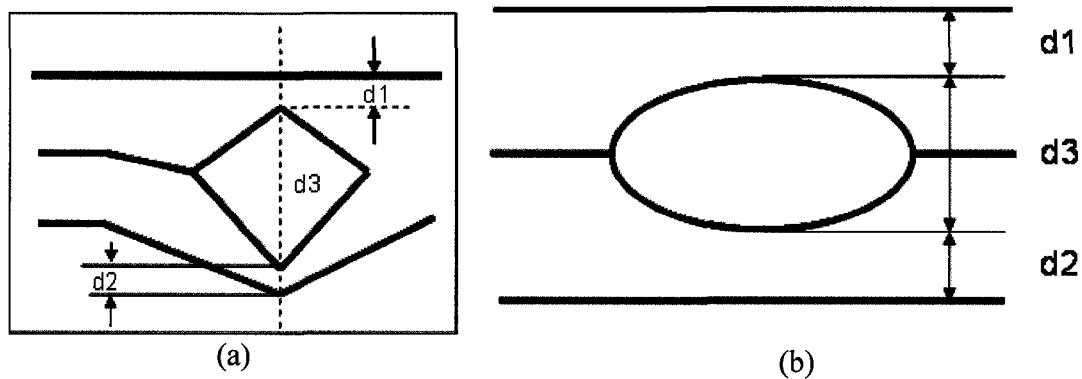
Figure 11. (a) schematic pattern of the weld signature; (b) schematic view of vertical weld geometry.

A set of tests was conducted in order to establish the direct correspondence of the weld signature penetration to the actual nugget size. 25 welds with different nugget penetrations have been manufactured and ultrasonic B-scan has been acquired for each of them. Metallographic sections were then made for all the joints, and measurements were performed. The following equipment for sample preparation was used: Buehler Delta AbrasiMet 1000 for cutting, Buehler SimpliMet and Buehler PowerPro 3000 for sample positioning and polishing. The photomicrographs were obtained using a Leica DMI 5000M microscope. Figure 12 and Figure 13 show the cross-sections and corresponding ultrasonic signatures of the welds. For every metallographic section three pictures have been made: the central and the two side parts. The geometry of the ultrasonic pulse positions is directly related to the nugget geometry. The error in measurement lies in the range of 7-10%. This error comes from both uncertainties in B-scan interface positioning and the uncertainties in establishing the nugget boundary, which may not be exactly parallel to the surface. Figure 14 shows the section of "cold" or stick weld. There was no melting involved in the process. The heat developed was not high enough to melt the base metal. One can easily distinguish the heat affected zone but the nugget was not formed here. Also, on the B-scan no evidence of internal solid-liquid interfaces is found.

Figure 12. B-scan and metallographic section of the good weld. Crystalline structure of the former liquid is well visible. The thickness of the nugget is measured 1.52 mm

27
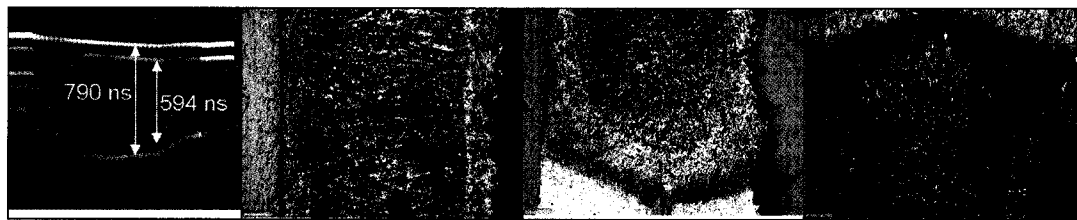
Figure 13. B-scan and metallographic section of the good weld. Crystalline structure of the former liquid is well visible. The thickness of the nugget is measured 1.47 mm
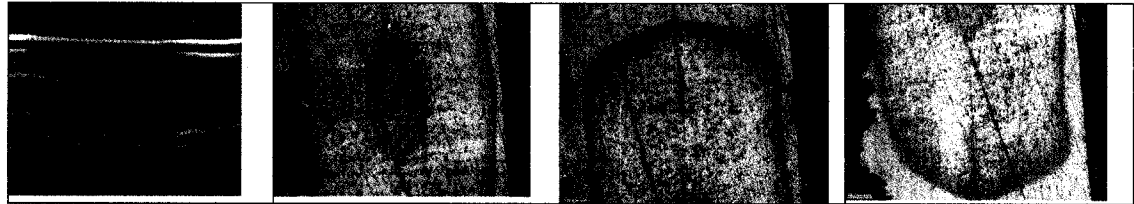
Figure 14. B-scan and metallographic section of the stick weld. Heat affected zone is well visible, but no nugget is formed.

According to the automotive standards, the minimum thickness of the nugget into the plate should be 35%. This value varies to some extent for different materials and stack-ups. The current study has established correlation between the nugget diameter and the liquid penetration into the plates. The diameter was measured with the standard peel test and the penetration was measured using ultrasonic scans. In the case of small nuggets, usually less than 3.0 mm, the reflections from the liquid pool are not strong enough to be registered on the B-scan. For this reason, the penetration of small nuggets is not well visible. Figure 15 shows two plots for relation of nugget size and the penetration of the liquid into the plate in per cent. The penetration is measured as the height that the liquid pool entered into the plate. The higher the pool the bigger the penetration. The percent value is calculated with respect to the plate thickness. Thus, 10% would correspond to a very shallow pool, and 90% would mean a very deep penetration into the plate.
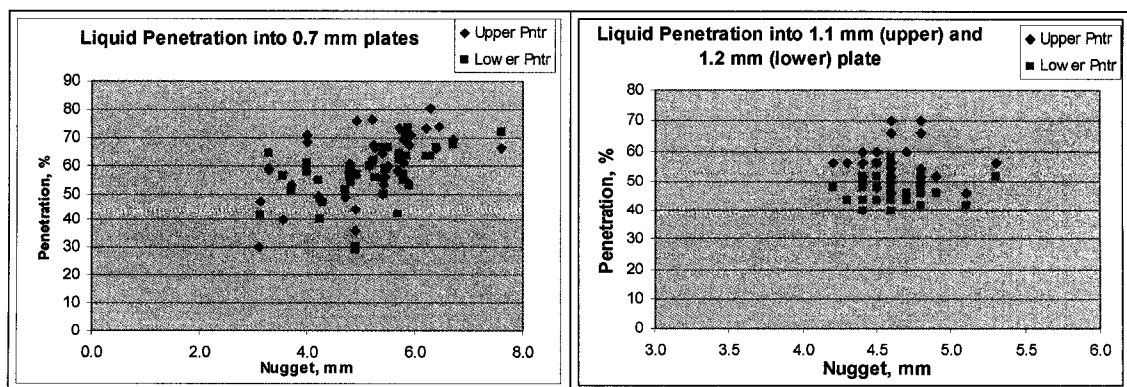
Figure 15. Liquid penetration versus nugget size. Penetration is the ratio of liquid penetration into the plate to the plate thickness; 0% - no penetration, 100% - liquid went through the whole plate.

As pictures show, there is very poor correlation between the nugget diameter and the nugget penetration degree. One can easily have two welds with 4.0 mm and 5.5 mm

28

and the same penetration into the plate. The interesting feature of these two graphs is the fact that for both 0.7 mm plate and 1.2 mm plate, a 70% thickness difference, the penetration for good welds is almost always above 40%. The minimum acceptable nugget diameter for 0.7 mm plate is 3.1 mm and for 1.1 mm plate is 4.3 mm. All welds with such corresponding nuggets have visible solid liquid interfaces, and liquid penetration is at or above 40%. This observation supports the accepted automotive standard of 35%. It is important to note that the single measurement of the liquid penetration with the acoustic method can determine whether the nugget is at or above the minimum acceptable value.

4.3. Central (Steel-Steel) Interface

The weld signature described in the previous section represented a good weld. There are, of course, other scenarios that depict the development of undersized welds and stick welds (no weld). When the heat developed within the plates is insufficient, the metal does not melt. If the plates are covered with zinc, the plates stick together by a thin layer of molten zinc. In other cases there is no adhesion at all and the plates fall apart once the electrodes are removed. The signature of such a no-bond weld is presented in Figure 16 (a). The central (steel-steel) interface never disappeared during welding, meaning that there was no fusion at it. In Figure 16 (b), the stick weld experienced some minor fusion at the very end of heating process. The steel-steel interface faded out close to the current OFF moment. The plates separated when only a slight force was applied to tear them apart. In Figure 16 (c), the signature of a 2.5 mm weld is shown. The surface area of the liquid nugget was still too small to provide a strong reflection of the signal. Thus, no solid-liquid interfaces are visible. An implicit evidence of melting is the fact that the steel-steel interface faded out somewhere in the middle of welding. This means the melting started at this interface, although no signal can reflect from it because of the lack of impedance mismatch or gap in this area.

29
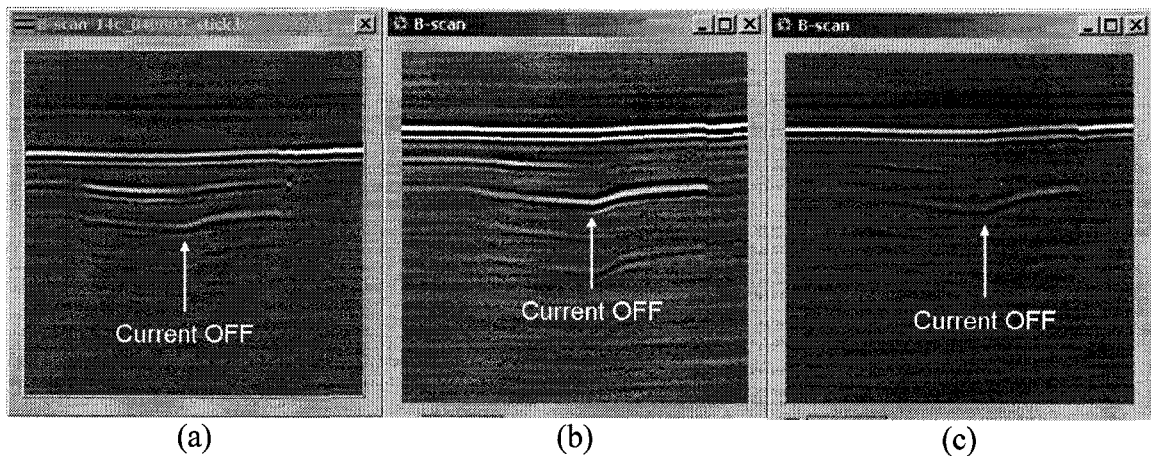
Figure 16. Signatures of undersize welds. (a) stick weld; (b) stick weld with minor melting; (c) 2.5 mm nugget; solid-liquid interfaces are too small to show visible reflection.

On Figure 17 (a) and (b) the developed nugget was small. The penetration into the plates was 25-35%. Also, the signature allows the determination of the initial moment of melting. This feature can be very important for those involved in technological development and control of welding new materials. Also, setting up the new welding schedules can dramatically benefit from the knowledge of the melt start; it provides information on the weld growth speed and thus possible deformations and cracks in the surrounding metal. This new technology provides valuable information without the need to conduct multiple destructive tests at different weld times. Figure 17 (c) presents the signature of the weld produced with the excessive current. The change of the slope (sign reversal) of the lower curve is due to indentation formation – pressing the electrodes into the base material of the plates. It has been noted that this indent formation happens only with good welds, which allows this feature to be used as a parameter for weld quality characterization. Presence of such positive slope of the lower curve before the current shutdown indicates the good quality of the weld.
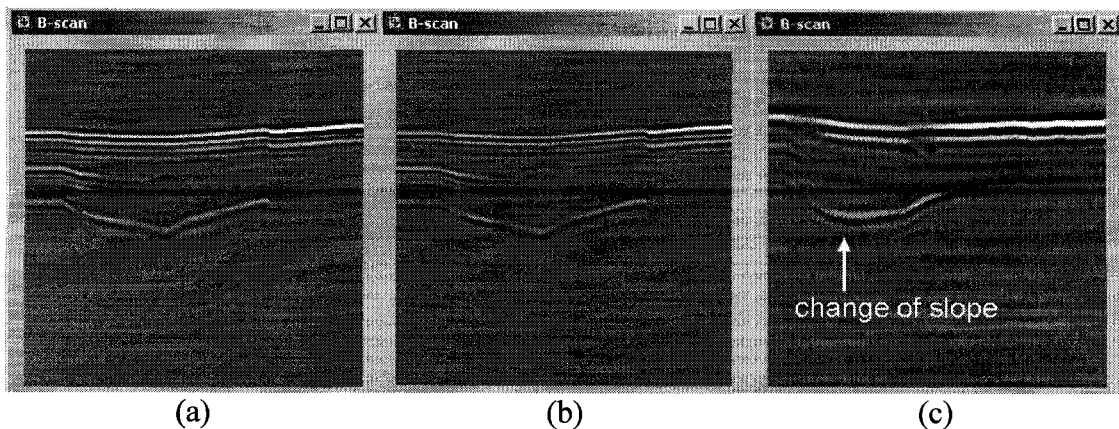
Figure 17. Signatures of the welds when melting took place.

30

The welding electrode conveying the electric current to the welded plates also provides most of the cooling for the joint. It removes the excess heat and helps keep the nugget within the plates, preventing the liquid from approaching too close to the surface. In cases of improper cooling of the welding electrode, heat is not removed from it efficiently. The electrode cools slower and heats up to a greater extent. In such cases, it is possible to observe the phenomenon of temporary signal disappearance. The reflection off the steel-copper interface fades out and disappears, then, it reappears later. Figure 18 shows such dynamics with the region of interest pointed with the arrow.
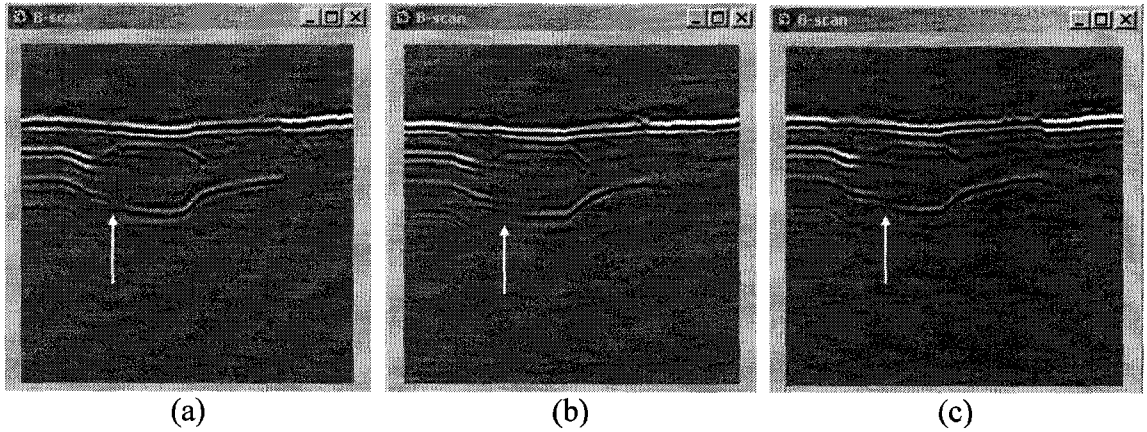
Figure 18. Temporary disappearance of the reflection from the second steel-copper interface.

The explanation of this effect comes from the nature of the reflectivity coefficient at the boundary. As the sound speed and density of the media are the functions of temperature, so is the acoustic impedance. As the temperature goes up, both the sound speed and density of metals drop. The acoustic impedance drops too, as long as it is just the product of speed and density:

$$Z(T) = \rho(T)c(T) \tag{3}$$

The published data for density as a function of temperature is not difficult to find. The more challenging task was that for sound speed. There are some measurements conducted for steels [7], but none has been found for copper. For this reason the sound speed for copper as a function of temperature was derived based on temperature dependence of Young modulus [9, 10] and density. Using temperature dependence of Young modulus and density it is possible to obtain the temperature dependence of longitudinal sound speed:

31

$$c(T) = \sqrt{\frac{E(T)}{\rho(T)}} \qquad (4)$$

Based on these calculations, the acoustic impedance for copper was calculated and compared to that of steel. The results are presented on Figure 19. It is clear that as the materials in contact heat up, their impedance mismatch reduces thus leading to a reduction in interface reflectivity. When the impedances become equal, the interface becomes 100% transparent to the longitudinal sound waves. All the energy is transmitted, and the steel-copper interface disappears on the B-scan. As there is a difference in the temperature of copper and steel at the boundary, and the copper temperature is usually lower than that of steel, this situation does not necessarily happens at around 1000° C where the curves intersect. There is a temperature jump at the copper-steel interface (see Figure 3). The zero-reflectivity situation can happen when the copper and steel temperatures yield the same acoustic impedance. Any horizontal line crossing both of the curves at the plot of Figure 19 defines two temperatures – for copper and steel, which provide the zero-reflectivity condition.

There are several scenarios possible. If the interface temperature continues to rise, the copper impedance can exceed that of the steel and the phase of the reflected wave will experience 180 degrees shift, and the reflection coefficient will go up. If the temperature reduces, the impedance mismatch will increase, and the reflection coefficient will also increase. The signal will become visible again, as is usually observed on the scans. In some situations, the reflectivity may continue to be low and the interface visibility will be low. The same situation can be observed with the upper copper-steel interface. But as long as the wave intensity at this interface is much higher, the variations in reflectivity will be seen on the B-scan as variations of interface intensity.

32
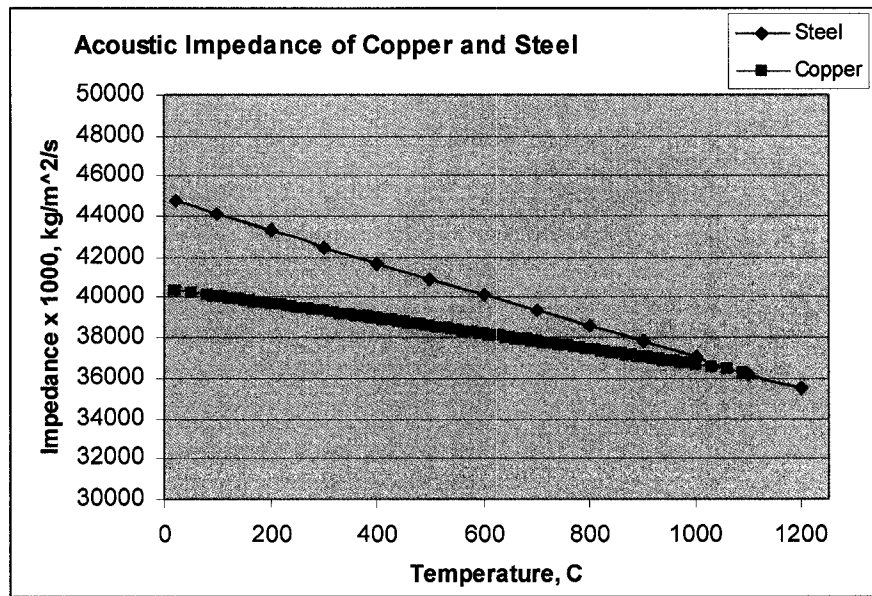
Figure 19. Acoustic impedances of copper and steel as functions of temperature.

4.5. The Liquid Pool Growth and Solidification Speeds

The observation of the dynamics of solid-liquid interfaces allows a determination of the speed of liquid penetration into the plate. Also, the rate of solidification is easily observable once the current is shut off. In Figure 20 the beginning of melting starts at the boundary of zones *B* and *C* – when the central interface disappears. The liquid reaches some depth and then the penetration stops. A thermal balance between the electrodes, which work as a heat sink, and the plates, which work as heat source, is established. During this time, the solid-liquid interfaces are almost parallel to the copper-steel ones, and the developed heat is spent for the lateral growth of the nugget. The lateral growth is not visible, a statement that is made based on multiple peel tests performed during the research. By making cross-sections of multiple welds produced with the same current settings but different welding times, it is possible to construct a similar picture of the average weld growth. The current method provides this information for a single weld in real time without destruction.

The process of liquid solidification is also visualized on the B-scan, zone *D*. The speed of liquid pool shrinkage can tell a lot about the cooling processes taking place in the plates. This kind of information is not available with any method currently used.

33

Though, the information provided can be valuable for the welding process engineers and research labs developing welding schedules for new metals and metal combinations.
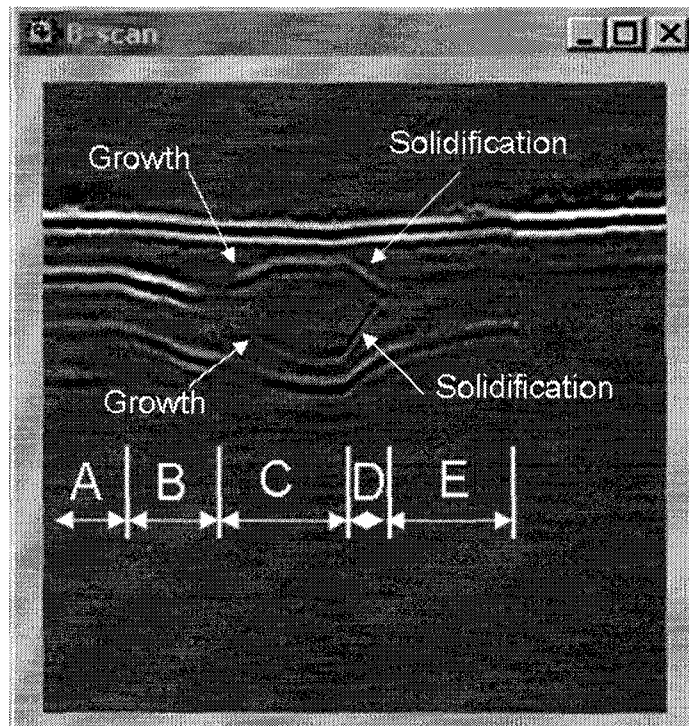
Figure 20. Liquid nugget growth and solidification.

5. Conclusions

This new method of real time spot weld growth monitoring provides significant information about weld development. Both industry and welding research labs can benefit from this technique.

In order to automate the process of weld characterization, however, a special processing software package still needs to be developed. The purpose of such software is to eliminate the noise from the image, recognize the pattern described in detail above, extract the previously mentioned parameters, and analyze the weld based on the extracted information. The research has seen progress towards making the software automatically recognize the weld pattern. What seems primitive for the human can make a hard time for the computer. The recognition of the patterns is not a trivial task; it requires considerable work before the system can recognize the features on the noisy scan. This work is primarily complete, and the results will be presented briefly in the chapter VII. The same chapter presents the principles of the fuzzy logic algorithm that is employed for the weld characterization. Besides these issues there are also other challenges which require the

34

attention of a software developer involved in signal processing and pattern recognition routine development. The signal received by the transducer is altered by the induction noise and unwanted reflections from the walls which overlap the useful signal. There are also additional physical mechanisms affecting the wave, which bring additional changes to the waveform and the time of flight measurements, both of which are critical for the proper interface location.

The frequency-dependent attenuation and diffraction effects arising due to the finite size of the transducer will be considered in the following two chapters as additional sources of wave distortion. These mechanisms of wave distortion will be studied and the correction techniques to counteract these effects will be presented.

References

1. *Transducer Built Into an Electrode.* R. Maev, A. Ptchelintsev, J. Mann., US Patent Number 6,297,467 B1, Date of Patent Oct.2, 2001.
2. *Experimental Study and Theoretical Modelling of Ultrasonic Wave Propagation in Resistance Spot Welds,* MSc Thesis, **Andriy M. Chertov,** Department of Physics, University of Windsor, Canada, 2003.
3. **A.M. Chertov,** R. Gr. Maev. "Determination of Resistance Spot Weld quality in Real Time Using Reflected Acoustic Waves. Comparison with Through-Transmission Mode." 16th World Conference on Nondestructive Testing, August 30 – September 3, 2004, Montreal, Quebec.
4. R. Gr. Maev, A. Ptchelintsev. "Monitoring of Pulsed Ultrasonic Waves' Interaction With Metal Continuously Heated to the Melting Point", in *Quantitative Nondestructive Evaluation-2000,* edited by D. O. Thompson and D.E. Chimenti., AIP Conference Proceedings 557. Melville, New York, 2000, pp. 1517-1524.
5. A. Ptchelintsev, and R. Gr. Maev. "Method of Quantitative Evaluation of Elastic Properties of Metals at Elevated Temperatures", in Quantitative Nondestructive Evaluation-2000, edited by D. O. Thompson and D.E. Chimenti, AIP Conference Proceedings 557. Melville, New York, 2000, pp. 1509-1516.
6. *Ultrasonic In-Process Monitoring And Feedback Of Resistance Spot Weld Quality* submitted to the US Patent Office in June 2004, R. Gr. Maev, **A. M. Chertov** et al. US Patent Application 20060076321.
7. Von W. Kurz, B. Lux. *Lokalisierung der Erstarrungsfront beim Stranggieben von Stahl.*
8. **Andriy M. Chertov** and Roman Gr. Maev, Senior Member, IEEE, A One-Dimensional Numerical Model of Acoustic Wave Propagation in a Multilayered Structure of a Resistance Spot Weld. IEEE Transactions on Ultrasonics, Ferroelectrics, and Frequency Control, vol. 52, no. 10, October 2005, pp. 1783-1790.
9. V. A. Levchenko and V. A. Borisenko, *Temperature Dependence of the Elastic Modulus of Copper and its Alloys.* Khimicheskoe i Neftyanoe Mashinostroenie, No. 7, pp. 11-12, July, 1978.
10. H. M. Ledbetter and W. F. Weston, *Low-Temperature Elastic Properties of Some Copper-Nickel Alloys.* Cryogenics Division, National Bureau of Standards, Boulder, Colorado 80302.

CHAPTER III

Investigation of the Effects of Frequency-Dependent Attenuation and Dispersion on Time of Flight Measurements

1. Introduction

Measurements of the time of flight of the reflected signal provide valuable information about the location of reflecting interfaces. Knowing the delay between the pulses and the speed of sound between reflecting interfaces allows calculation of the travel distance, or, the thickness of the layer. For precise measurements of the distance, the "speed of sound" and "delay between pulses" will need to be defined more clearly.

Frequency-dependent attenuation and phase velocity (dispersion) impose some ambiguity on the measurements, as these two factors modify various frequency components of the broadband signal differently. Thus, transit time measurements are complicated by the fact that pulses contain a range of frequencies, and in dispersive media each frequency will propagate at its own velocity, which lead to the elongation of the pulse in both time and space.

2. Attenuation of Sound Waves in the Medium

For a liquid ideal continuous media without viscosity and thermal conductivity, the Newton's Second Law will have the following form [1]:

$$\rho \frac{d\vec{v}}{dt} = -\nabla p + \rho \vec{f}, \tag{1}$$

where v is the velocity of the moving liquid in the given point, ρ is the density, p is the pressure, and f is the force acting on the unit mass of the liquid. In the absence of discontinuities in the liquid, there is mass conservation within a volume of the media presented by continuity equation:

$$\frac{\partial \rho}{\partial t} + \nabla(\rho \vec{v}) = 0. \tag{2}$$

37

In the absence of a mass source, the second term of this equation is equal zero. For an incompressible medium, the density is constant and

$$\nabla \vec{v} = div(\vec{v}) = 0.$$ (3)

All these equations are valid for infinitely small oscillations. For such oscillations, the superposition principle can be applied with a high degree of precision. According to modern classification, this area is considered by linear acoustics. In linear acoustics approximation, the velocity of disturbance propagation in the media is independent of the disturbance magnitude.

In acoustics, rot(v) = 0, the velocity represents an irrotational field, and it is possible to introduce the scalar potential of the velocity of the oscillating particle: $\vec{v} = \nabla \varphi$. Thus, the wave equation for the velocity potential can be presented as:

$$\frac{\partial^2 \varphi}{\partial t^2} - c^2 \nabla^2 \varphi = 0.$$ (4)

For the simplest example of the wave motion – the plane wave moving in the positive x-direction – the one-dimensional solution of this equation will have the form

$$\varphi(x,t) = \varphi_0 \exp(i(\omega t - kx)).$$ (5)

The sound pressure will take the form $p = p_0 \exp(i(\omega t - kx))$, where $p_0 = -i\rho_0 \omega \varphi_0$, and the velocity of the oscillating "liquid particles" will be $v = v_0 \exp(i(\omega t - kx))$ with $v_0 = -ik\varphi_0$. From these expressions the velocity and pressure can be related using the medium density and speed of sound:

$$v = \frac{p}{\rho_0 c}.$$ (6)

As the sound propagates through the medium, the amplitude of wave oscillations decreases. There are several reasons: reduction of the wave energy density due to increase of the wave-front surface (spherical, cylindrical and other divergent waves), absorption of the energy due to dissipation caused by media viscosity and heat conductivity, and scattering. For a plane wave the amplitude reduction due to the dissipation is characterized by the attenuation coefficient, α, showing the distance through which the amplitude drops by e times:

$$p = p_0 \exp(-\alpha x).$$ (7)

38

To define the attenuation coefficient as a function of the media properties, one needs to take into account all of the dissipation mechanisms taking place during wave propagation. In order to take into account viscosity and heat conductivity, another term for dissipation needs to be added into the wave equation (4). This term can be derived from the hydrodynamic equations for a viscous, heat conductive medium. In linear approximation they will take a form of (4) but with c being complex value:

$$c^2 = \frac{\omega^2}{\overline{k}^2} = \frac{\omega^2}{(k^2 - j\alpha)^2}$$

The sources of dissipation may be divided into two general categories: those intrinsic to the medium, and those associated with the boundaries of the medium [2]. For broadband attenuation studies the second group can be considered as frequency-independent in the absence of contact clamping or other nonlinearity generating effects. This category of boundary losses thus can be ignored while studying wave shape transformation. Losses in the medium may be further subdivided into three basic types: viscous losses, heat conduction losses, and losses associated with internal molecular processes. Viscous losses occur whenever there is relative motion between adjacent portions of the medium, such as during compressions and expansion that accompany the transmission of a sound wave. Heat conduction losses result from the conduction of thermal energy from higher temperature condensations to lower temperature rarefactions. Heat conduction losses occur only in longitudinal waves, since shear waves do not produce changes in size of the elementary volume elements. Molecular processes leading to absorption include the (1) conversion of the kinetic energy of the molecules into potential energy (clustering of molecules), (2) rotational and vibrational energies, and (3) energies of association and dissociation between different ionic species and complexes in ionized solutions.

3. Forces Acting on a Liquid

In an idealized, nonviscous fluid, only hydrostatic pressure exists. A uniform hydrostatic pressure would not yield a resultant force on any part of the liquid [3, 4]. Thus, the force results only from differences in pressure. For example, if pressure varies

39

in the x direction only, the resultant force on a thin, liquid sheet of area $dydz$ and thickness dx is determined by the difference in pressure on the two sides of the sheet, and the resultant force in the x-direction is

$$(p(x) - p(x + dx))dydz = -\frac{dp}{dx}dxdydz.$$ (8)

In general, the resultant force on a volume element dv is $-\textbf{grad(p)}dv$.

For a less idealized fluid, however, it is necessary to describe the stresses in the liquid by a more complicated quantity than the scalar hydrostatic pressure, namely, by a symmetrical stress tensor P_{ij}.

The stresses in the deformed media are defined in terms of forces acting on surfaces of the limited volume of the medium. The stress tensor is a quantity which enables the determination of such a force on any arbitrarily oriented surface within this volume. If the surface within an infinitely small volume can be defined by the unit vector normal to the surface then the traction force can be defined by

$$\begin{bmatrix} P_{xn} \\ P_{yn} \\ P_{zn} \end{bmatrix} = \begin{bmatrix} P_{xx} & P_{xy} & P_{xz} \\ P_{yx} & P_{yy} & P_{yz} \\ P_{zx} & P_{zy} & P_{zz} \end{bmatrix} \begin{bmatrix} n_x \\ n_y \\ n_z \end{bmatrix}.$$ (9)

Here, the left side is the traction force vector represented by the three components of the force acting on the surface with normal vector n in x, y and z directions. The 3x3 matrix on the right side is the stress tensor which uniquely defines the traction force on any surface within the volume and the 1x3 matrix represents the components of the unit normal vector of the surface.

Consider a vibrating particle of arbitrary shape, with volume dV and surface area dS. The forces associated with its vibration are a body force $\mathbf{F}dV$ and traction forces applied to its surface by the neighbouring particles:

$$\int_{dS}(P \cdot \vec{n})dS + \int_{dV}\vec{F}dV = \int_{dV} \rho \frac{\partial^2 \vec{u}}{\partial t^2}dV.$$ (10)

Using the divergence theorem, the first term can be converted into the volume integral of the stress divergence, and the translational equation of motion will take form:

$$\nabla \cdot P = \rho \frac{\partial^2 \vec{u}}{\partial t^2} - \vec{F}, \text{ where}$$ (11)

40

$$\nabla \cdot P = \hat{x}\left(\frac{\partial}{\partial x}P_{xx} + \frac{\partial}{\partial y}P_{xy} + \frac{\partial}{\partial z}P_{xz}\right) + \hat{y}\left(\frac{\partial}{\partial x}P_{yx} + \frac{\partial}{\partial y}P_{yy} + \frac{\partial}{\partial z}P_{yz}\right) + \hat{z}\left(\frac{\partial}{\partial x}P_{zx} + \frac{\partial}{\partial y}P_{zy} + \frac{\partial}{\partial z}P_{zz}\right). \tag{12}$$

For an ideal liquid, only diagonal terms exist, meaning there are no shear components of stress. Only compressional waves can propagate in an ideal liquid. It is useful to take the hydrostatic pressure out of the stress tensor P. The remainder shall be called P'. This means

$$P_{ii} = -p + P'_{ii}$$
$$P_{12} = P'_{12}, \quad P_{23} = P'_{23}, \quad P_{31} = P'_{31} \tag{13}$$

The force per unit volume is then

$$div(P) = -grad(p) + div(P'). \tag{14}$$

4. Stress-Strain Relations

It is necessary to establish a connection between the elastic restoring forces and material deformation. For small deformations, the strain is linearly proportional to the applied stress (Hooke's law). In 3-dimensional space, the general form for linear case will be

$$T_{ij} = c_{ijkl}S_{kl}, \quad i,j,k,l \text{ run through } x,y,z \tag{15}$$

where on the left side one can see the stress tensor T connected with the strain tensor S by the "microscopic spring constants" called elastic stiffness constants, c.

5. Attenuation due to viscosity

Acoustic vibrations described by $T = cS$ equation are completely undamped. It means that wavelike vibrations propagate without any decrease, or attenuation, of amplitude, and that resonant oscillations persist infinitely. This is an idealization, and real-world situations need to be described more precisely by introducing the damping into

41

the elastic constitutive relations. Elastic damping usually depends on temperature, frequency, and type of vibration. There is a rather impressive number of physical mechanisms that contribute to the attenuation, but in many cases acoustic losses may be adequately described by a viscous damping term.

In an ideal lossless medium, Hooke's Law corresponds to a force-displacement relation, i.e., $f=Kx$, where applied force corresponds to stress and the displacement to strain. Damping is added to this system by placing a viscous element, with response

$$f = K' \frac{\partial x}{\partial t},$$ (16)

in parallel with the force-displacement. The response of the damped system is then specified by the differential equation

$$f = Kx + K' \frac{\partial x}{\partial t}.$$ (17)

The damping, or resistance, of the media to the motion is proportional to the velocity of motion. The higher the velocity the bigger the drag. The ideal Hooke's Law is modified to include damping by adding terms containing time derivatives of the strains:

$$P_{ij} = c_{ijkl} S_{kl} + \eta_{ijkl} \frac{\partial S_{kl}}{\partial t}.$$ (18)

Figure 21 shows the way the shear viscosity is visualized. In general, in any flow, layers move at different velocities and the fluid's viscosity arises from the shear stress between the layers that ultimately opposes any applied force. Isaac Newton postulated that, for straight, parallel and uniform flow, the shear stress, P, between layers is proportional to the velocity gradient, $\partial v / \partial y$, in the direction perpendicular to the layers, in other words, the relative motion of the layers.
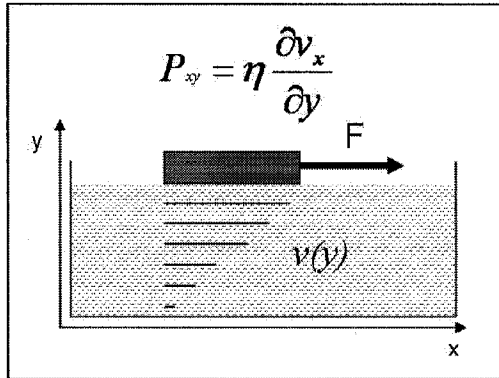
Figure 21. Force applied to the viscous medium.

42

The abbreviated notation allows reduce the complexity of tensor calculations. This notation takes advantage of the fact that the shear components of the stress such as P_{xy} equal to P_{yx}. It allows reduce the number of stress and strain tensor components from 9 to 6, the first three representing compression and the remaining three representing shearing deformation. In such notation the stiffness matrix c_{ijkl} and viscosity matrix η_{ijkl} will take a form

$$\begin{bmatrix} c_{11} & c_{12} & c_{12} & 0 & 0 & 0 \\ c_{12} & c_{11} & c_{12} & 0 & 0 & 0 \\ c_{12} & c_{12} & c_{11} & 0 & 0 & 0 \\ 0 & 0 & 0 & c_{44} & 0 & 0 \\ 0 & 0 & 0 & 0 & c_{44} & 0 \\ 0 & 0 & 0 & 0 & 0 & c_{44} \end{bmatrix} \text{ and } \begin{bmatrix} \eta_{11} & \eta_{12} & \eta_{12} & 0 & 0 & 0 \\ \eta_{12} & \eta_{11} & \eta_{12} & 0 & 0 & 0 \\ \eta_{12} & \eta_{12} & \eta_{11} & 0 & 0 & 0 \\ 0 & 0 & 0 & \eta_{44} & 0 & 0 \\ 0 & 0 & 0 & 0 & \eta_{44} & 0 \\ 0 & 0 & 0 & 0 & 0 & \eta_{44} \end{bmatrix}. \tag{19}$$

The stress due to viscosity can be divided into two components: $P = P' + P''$. These two components will be responsible for shear and bulk viscosity contributions respectively.

$$P'_{ii} = 2\eta \left(\frac{\partial v_i}{\partial x_i} - \frac{1}{3} div(v) \right) \tag{20}$$

$$P'_{ij} = \eta \left(\frac{\partial v_i}{\partial x_j} + \frac{\partial v_j}{\partial x_i} \right) \tag{21}$$

$$P''_{ii} = \eta' div(v) \tag{22}$$

$$P''_{ij} = 0. \tag{23}$$

These equations separate shear viscosity, η, from bulk (compression) viscosity, η', by subtraction diagonal terms from the stress tensor. In this case, $P'_{11} + P'_{22} + P'_{33} = 0$.

η is usually measured in cases where the velocity varies in a direction normal to that of the flow, in which case shear stresses arise. However, the shear viscosity also contributes to the normal stresses even in compressional waves. For example, in a one-dimensional compressional flow, as in a plane sound wave propagating in the x-direction, where only the x-component of the velocity is non-zero, there are contributions of the shear viscosity to the normal stresses.

43

$$P'_{11} = 2\eta\left(\frac{\partial v_x}{\partial x} - \frac{1}{3}\frac{\partial v_x}{\partial x}\right) = \frac{4}{3}\eta\frac{\partial v_x}{\partial x}$$

$$P'_{22} = P'_{33} = -\frac{2}{3}\eta\frac{\partial v_x}{\partial x}$$

and $P'_{ij} = 0$. (24)

To understand this concept the unidimensional compressional flow described by $\partial u_x / \partial x$ can be considered. It can be seen as the superposition of the two flows. One, isotropic and purely compressional (expansional), is equal to

$$\frac{1}{3}\left(\frac{\partial v_x}{\partial x} + \frac{\partial v_y}{\partial y} + \frac{\partial v_z}{\partial z}\right). \qquad (25)$$

This does not contribute to shear loss. The second flow is pure shear, noncompressional, and has the components

$$\frac{2}{3}\frac{\partial v_x}{\partial x}, \quad -\frac{1}{3}\frac{\partial v_y}{\partial y}, \quad -\frac{1}{3}\frac{\partial v_z}{\partial z}. \qquad (26)$$

The flow of the second kind is equivalent to a pure shear flow along the axes rotated 45°, see Figure 22.

longitudinal = pure expansion + pure shear
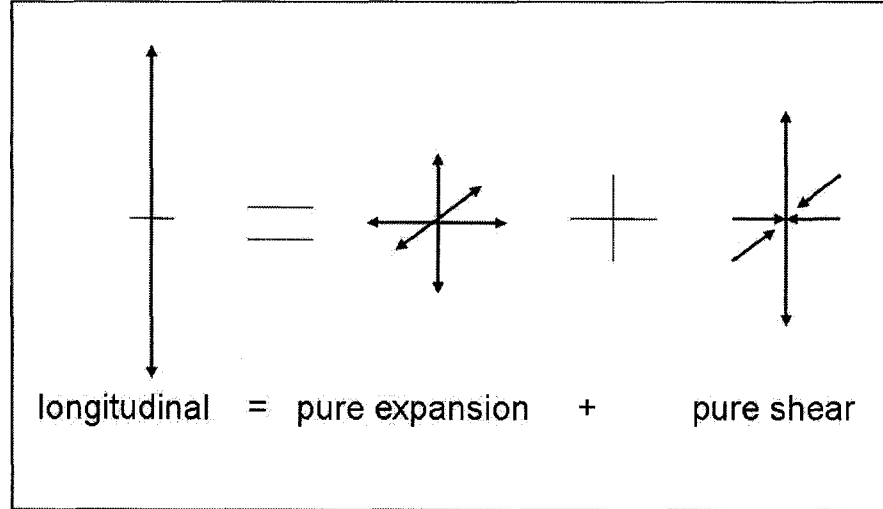
Figure 22. Longitudinal wave, considered as superposition of pure extension and pure shear.

The P'' is a scalar like a hydrostatic pressure, and defines the compressional stress due to the volume viscosity. In one dimension, the linearized equation of motion $\rho_0\frac{\partial v}{\partial t} = div(P)$ has the form

$$\rho_0\frac{\partial v}{\partial t} = -\frac{\partial p}{\partial x} + \frac{4}{3}\eta\frac{\partial^2 v}{\partial x^2} + \eta'\frac{\partial^2 v}{\partial x^2}. \qquad (28)$$

44

Using this equation the absorption coefficient defining the distance through which the amplitude decreases by e times will take the form

$$\alpha_\eta = \frac{\omega^2}{2\rho_0 c^3}\left(\frac{4}{3}\eta + \eta'\right). \tag{29}$$

6. Attenuation and Dispersion Due to Heat Conduction. Total Attenuation

In order to calculate the effect of dissipative mechanisms on sound propagation in metallic liquid, heat conduction must be included, as long as it has high value in metals. Considering the picture of a sound wave at a given time, the density crests will have temperatures above the average; the density troughs will have temperatures below the average. Heat conduction will tend to equalize the temperature. Accordingly, the compressed regions will, upon re-expanding, return less work than was expended in compressing them. Similar statement applies to the recompression of rarefaction regions. The result is loss, i.e., sound absorption [4].

From kinetic theory, the kinetic energy of translation is proportional to the temperature. The molecules in hotter regions have greater kinetic energies, which diffuses into surrounding cooler regions through intermolecular collisions. As energy leaves the region, it is lost from the acoustic process, converted to the random thermal energy of molecular motion. The change in thermal energy is related to the change in temperature by

$$\frac{\Delta q}{\Delta t} = c_P \rho_0 \frac{\partial T}{\partial t}, \tag{30}$$

where c_P is the specific heat at constant pressure and Δq is the gain in thermal energy of a unit volume. The diffusion process is described by a diffusion equation, which can be written for temperature as

$$\frac{\partial T}{\partial t} = \frac{\kappa}{c_P \rho_0}\nabla^2 T \tag{31}$$

where κ is the thermal conductivity. Combining these, one obtains

$$\frac{\Delta q}{\Delta t} = \kappa \nabla^2 T \tag{32}$$

45

Integrating over the volume of the medium gives the instantaneous rate of loss of acoustic energy in the volume. The time average of this rate of loss over a period of the motion will give the average rate of heat (and thus acoustic energy) loss. This loss is proportional to the spatial rate of temperature change. For short wavelengths (high frequencies) the temperature gradient is higher which leads to the higher losses (heat dissipation) within the compressed region.

To take into account heat conduction in the process of dissipation, one should consider

$$\rho_0 T_0 \frac{\partial s}{\partial T} = \kappa \Delta T$$ where s is the entropy of the system. The increase of entropy s' will

take the form [1]

$$s' = -\frac{\kappa}{T}\left(\frac{\partial T}{\partial p}\right)_S div(v) \tag{33}.$$

Using thermodynamic relations, the increase of the pressure can be derived as

$$p' = c^2 \rho' - \kappa(1/C_V - 1/C_P)div(v). \tag{34}$$

The relations used to derive these formulas are valid for the ideal medium. Use of those relations is possible only when the heat conduction and viscosity have a small influence on sound propagation: $\alpha \lambda \ll 1$ - meaning that sound experiences a very small change over the distance of one wavelength. Using this concept the Stokes-Navier equation will take the form

$$\rho_0 \frac{\partial v}{\partial t} = -\frac{\partial p}{\partial x} + \left(\frac{4}{3}\eta + \eta' + \kappa(1/C_V - 1/C_P)\right)\frac{\partial^2 v}{\partial x^2}. \tag{35}$$

Converting to velocity potentials, it is possible to write the solution to this wave equation in the form

$$p = p_0 \exp(-\alpha x)\exp(i(\omega t - kx)) \text{ where} \tag{36}$$

$$\alpha = \frac{\omega^2}{2\rho_0 c^3}\left[\frac{4}{3}\eta + \eta' + \kappa\left(\frac{1}{C_V} - \frac{1}{C_P}\right)\right]. \tag{37}$$

This equation takes into account the most influential processes affecting the amplitude and shape of the wave [13].

In liquid metals, the volume viscosity has the same order of magnitude as the shear viscosity. [9]. The classical attenuation coefficient does not include the volume viscosity and takes into account only shear viscosity and attenuation due to heat conduction:

46

$$\alpha = \frac{\omega^2}{2\rho_0 c^3}\left[\frac{4}{3}\eta + \kappa\frac{(\gamma-1)}{C_p}\right]$$ (38)

Here, the C_V was replaced using $\gamma = C_p / C_V$.

For liquid metals the contribution of heat conductivity to sound absorption is comparable to that of the viscosity and needs to be taken into account. Calculations have been performed for liquid mild steel with the following values: $\eta = 0.004$ Pa-s; $\kappa = 28.4$ W/m/K; $C_p = 848.25$ J/kg/K.

In this case, the first term in the brackets of (38) is 0.0053 Pa-s, and the second term is 0.0133 Pa-s. It shows that contribution of heat conductivity is about 70% and plays the dominant role in the process of sound attenuation.

In general, the volume, or bulk, viscosity cannot be measured directly. The attenuation which is predicted above by this equation is explained by the existence of the volume viscosity η' and is defined as

$$\alpha' = \alpha_{MEASURED} - \alpha_{CLASSICAL}.$$ (39)

Thus,

$$\eta' = \frac{4}{3}\eta\frac{\alpha - \alpha_{CLASSICAL}}{\alpha_{SHEAR}}.$$ (40)

In liquid metals, the attenuation due to the heat conduction is 5-12 times higher [9] than that of the shear viscosity. It is considered as the main contributor to the attenuation.

The frequency dependence of the attenuation and also phase velocity is quite complex and is defined by different relaxation phenomena taking place in the liquid.

The attenuation above that of (38) can be explained by relaxation mechanisms of sound energy transfer during inelastic collisions of the atoms. In this situation, the kinetic energy of the particle is transferred into rotational and vibrational energies and visa versa. Relaxation process can be explained as a lag of the deflection of the macroscopic system from its equilibrium state or return to this state. The entropy of the system will increase as the sound propagates through the medium, and part of the energy will be lost as heat. As a result, dispersion of the sound velocity will be observed.

Qualitatively, it can be explained as follows. The full energy of medium is the sum of the kinetic energy of advancing particles (atoms, molecules) – external degrees of freedom, and rotational and oscillating energies – internal degrees of freedom.

47

Correspondingly, the heat capacity, C_V, will be the sum of heat capacities due to internal and external degrees of freedom. If the sound is of low frequency, and the period of oscillations is much greater than the relaxation time (time when deviation from an equilibrium state of heat capacity and particle energies decreases by e times), then the equilibrium between excited and unexcited particles goes in step with the change of pressure in the sound wave. In this case, for an ideal gas

$$c_0 = \left[\frac{p}{\rho}\left(1 + \frac{R}{C_{V\,internal} + C_{Vexternal}} \right) \right]^{1/2} \quad \text{for low frequencies.} \qquad (41)$$

At high frequencies, the equilibrium between internal and external degrees of freedom will not follow in time the changes imposed by the wave and $C_{V\,internal} \rightarrow 0$. In this case

$$c_\infty = \left[\frac{p}{\rho}\left(1 + \frac{R}{C_{Vexternal}} \right) \right]^{1/2}. \qquad (42)$$

In this case, the lag between the changes imposed by the wave and reaction of the medium to these changes will cause sound velocity dispersion. The velocity increases, or, it can be said that effectively the stiffness of the media increases for higher frequencies.

Also, the processes of energy exchange between internal and external degrees of freedom of the molecules generate not only dispersion but also additional attenuation of the sound. Other relaxation phenomena include translational relaxation, in which some time is required for establishing Maxwell's distribution of particle velocities (requires several collisions between the particles); and structural relaxation which involves the changes of fluid structure in the vicinity of compressed or sheared areas.

However, this happens when the frequencies are comparable with relaxation times of the specific phenomenon. For liquid steel, the estimated relaxation time for thermal conduction has the order of 10^{-13} s, relaxation of volume viscosity $\sim 10^{-14}$ s. For the sound pulses with central frequency of 10 MHz and bandwidth of 5-10 MHz these times are too short to be influential.

The phase velocity of the sound wave can be approximated by

$$c = c_0 \left(1 + \frac{3}{8}(\omega\tau)^2 \right) \qquad (43)$$

48

which shows that for $\omega\tau \ll 1$ (10 MHz satisfies this inequality) the dispersion is negligible. It only becomes considerable when the wave frequency is comparable to relaxation time in the medium.

7. Theoretical Estimation of the Frequency-Dependent Attenuation

Application of equation (38) and consequently (36) allows the estimation of the sound attenuation as a function of frequency. The medium was considered as liquid mild steel at a temperature of 1900 K with the following properties:

Physical Quantity	Value	Units
ρ_0 (density)	6500	kg/m^3
c (sound speed)	3600	m/s
η (viscosity)	0.004	Pa-s
κ (thermal conductivity)	28.4	W/m/K
C_P (heat capacity)	848.25	J/kg/K

The frequency range is taken as 5 through 15 MHz. The result of calculating the α coefficient as a function of frequency are shown on Figure 23. Application of (36) using the data presented on Figure 23 yields the attenuation coefficient of a sample of the thickness of 4.0 mm. The stack-up of two 1.0-mm plates makes sound effectively travel 4.0 mm in the sample in the reflection mode. This value is also called normalized broadband ultrasonic attenuation. This attenuation yields average pressure losses of 0.97 dB/MHz [10].

49
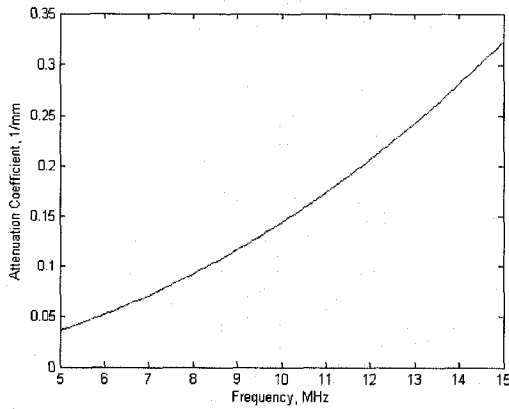
Figure 23. Attenuation coefficient in liquid mild steel.
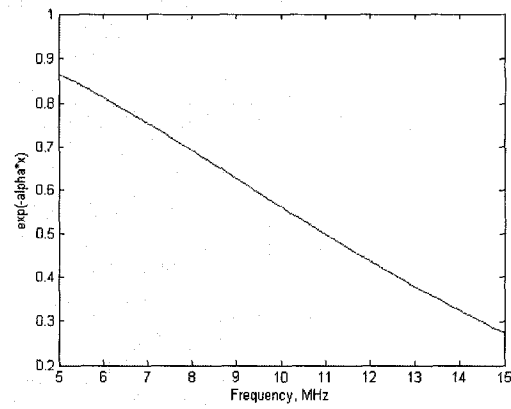
Figure 24. Normalized broadband ultrasonic attenuation. x=4.0 mm.

8. The effects of Frequency-Dependent Attenuation and Dispersion on Time-of-Flight Measurements

Precise measurement of the reflected signal delay, or time-of-flight, is of great importance in ultrasonic non-destructive testing. The delay describes the distance the signal has travelled if the sound speed is known. In some processes it is necessary to only measure the change of the travel time to get an insight into the process being tested. The change of travel time can be due to geometric changes of the sample and also due to the changes taking place in the medium. Heating cause both geometry changes due to thermal expansion (contraction) and velocity changes due to material stiffness, and density changes.

As the wave reflects from the back wall or the obstacle it comes back to the receiver and needs to be registered. There are many ways to detect the wave and to determine its arrival time. Due to the spreading in time of the finite-band wave, there is no standard procedure to detect the exact moment of the wave arrival. The most widely used are:

- Marking the first zero crossing of the wave after hitting the predetermined threshold;

- Marking the first moment the wave crosses the threshold;

- Marking the second, third and so on zero-crossing (depending on the application and physics of the setup);

- Enveloping of the signal and determining the peak position of the envelope;

50

- Cross-correlation of the received signal with the reference signal;

- Determining the phase slope of the arrived signal and comparing it with the phase slope of the reference signal. The difference can be recalculated into the delay (if needed).

- Digital overlap method.

- Leading edge detection (first detectable deviation from zero).

- Thresholding at three times the noise standard deviation.

- First and second maxima and minima.

All of these methods have their advantages and drawbacks. The zero-crossing and digital overlap methods can suffer from the signal phase inversion upon the wave reflection from some interfaces. In this case, the threshold that was set to a certain level with respect to the maximum amplitude could point to the wrong zero-crossing. Enveloping and phase-slope are not good at low signal-to-noise ratio (SNR) situations.

Another serious issue which affects the preciseness of the time-of-flight measurements is the frequency-dependent attenuation and dispersion, which distort the signal shape. When different harmonic components of the broadband signal travel at different velocities, they spread out in time domain and deform the signal shape. Similar shape deformation happens when different harmonics attenuate differently. This is almost always the case when a high-frequency sound wave travels through the medium.

9. Attenuation of the Signals on the Acoustic Signature of the Weld

In order to check for wave frequency content change, the short-time Fourier transform (STFT) technique was used. Its purpose is to cut a small part of the long signal and perform its Fourier transform to see the frequency content of a wave at different points in time, or at different parts of an oscillogram (the A-scan). As the wave propagates through the medium it will lose or weaken some of its frequency components so that the longer the wave travels the more it will lose. The STFT allows one to visualize the spectrum of the wave which has undergone multiple reflections within the sample.

The idea of STFT is to swipe the envelope of the form

$$y = \exp\left(\left(\frac{x-a}{D}\right)^N\right)$$ (44)

through the A-scan, where a changes as the envelope progresses in time; D defines width of the envelope and N – its steepness. The choice of the variables D and N is defined by the signal shape and by attempt to separate closely spaced waveforms reflected from closely spaced interfaces. Too high a value of N (greater than 4) could produce too steep of a rise of the bell-shaped envelope, which will lead to generation of an artificial high-frequency noise. Too small a value of N (less than 3) will stretch the envelope and make it very non-localized. Still, the envelope should cover most of the waveform when positioned at the center of gravity of the waveform. These considerations made the numbers to be as follows: $N = 4$, $D = 8.5$ with the total scan length of 256 points. The Figure 25 shows how these two numbers modify the envelope shape.

(a)   (b)   (c)
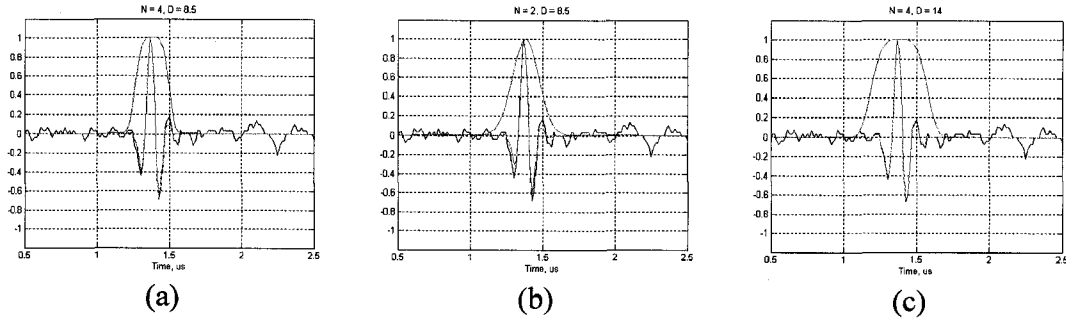
Figure 25. Different types of possible envelopes.

Figure 25 (a) shows the optimal envelope shape with $N = 4$ and $D = 8.5$. In (b) $N = 2$ which makes the tails go too far and in (c) $D = 14$ which makes the bell too wide; in this case the spatial resolution is too low to distinguish closely spaced reflections.

(a)   (b)
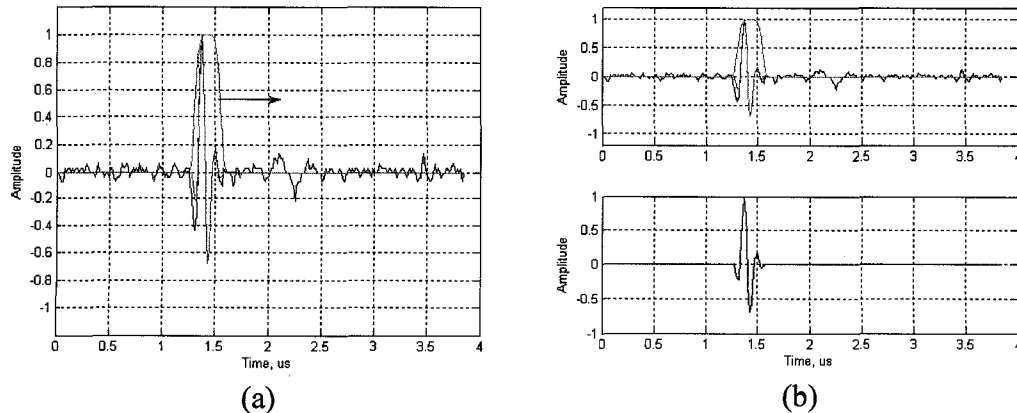
Figure 26. STFT method explained. Sliding window to cut part of the waveform from the raw signal. (a) the window is sliding along the time axis; (b) the window is overlapped with the signal (top) and the signal is multiplied by normalized window (bottom).

52

Figure 26 demonstrates the general idea of the technique. Running parameter a from 1 to 256 makes the envelope move along the full A-scan from left to right. The Fourier transform (FT) is performed on the partial signal cut from the original signal (the lower waveform of Figure 26 (b)). As the envelope slides along the A-scan, the 2-dimensional image is formed by the FT vectors (put vertically) obtained at every new point of the envelope center, Figure 27 (a). The horizontal axis of such an image presents the center position of the envelope, and the vertical axis presents the frequency from 0 Hz to half the sampling frequency (33 MHz). It is composed of the vertically positioned FT vectors; typical vector is shown at Figure 27 (b) being a section at position 60 of the STFT image. The amplitude of the FT vector is presented by color on the STFT image with blue standing for the lowest amplitude and brown – for the highest.
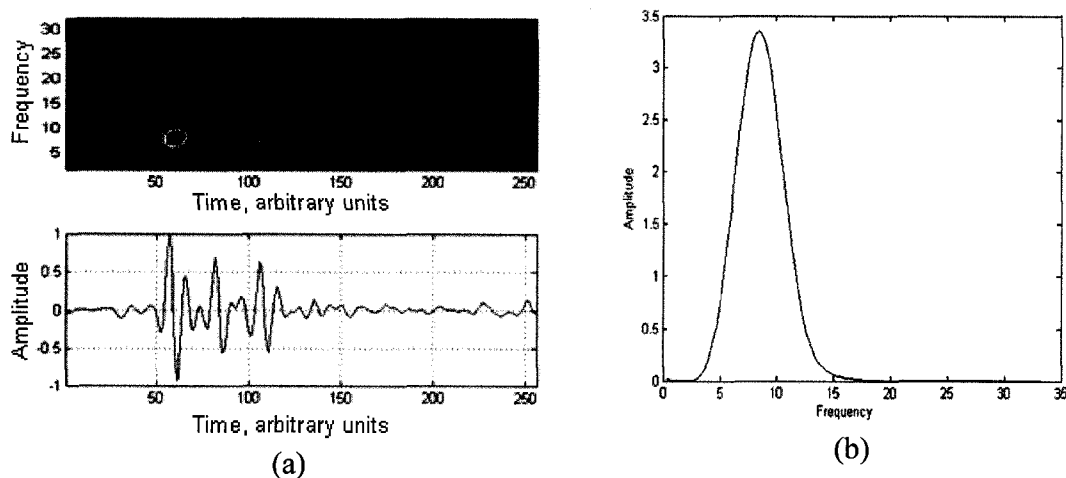
Figure 27. STFT method explained. (a) A-scan and its STFT picture consisting of Fourier spectrums put vertically along the horizontal axis; (b) one of the vertical components (FT spectrum) of 2-dimensional STFT image.

Such a method allows the easy visualization of the difference in the spectral content for the different reflections within the specimen. The round purple markers on the STFT image position the local maximum of the frequency for every reflection. Every subsequent waveform is separately analyzed for its frequency content. Such a local maximum shows the position of the central frequency of the waveform.

Such a procedure allows one to examine every A-scan within the B-scan. The following pictures of Figure 28 demonstrate such an analysis for three characteristic A-scans obtained before the current is on (A-scan 22), during heating process but still no liquid present (A-scan 65) and at the end of the welding when the liquid pool thickness is

53

the biggest (A-scan 140). The first two scans demonstrate no change of the central frequency for the three reflections coming from copper-steel, steel-steel and steel-copper interfaces. The third one is somewhat different – only the copper-steel and steel-copper interfaces (external ones) can be seen. The difference in central frequency for these two reflections is obvious – the second reflection having a value some 2 MHz lower than the first one. This effect can be explained by broadband ultrasonic attenuation (BUA) taking place in the liquid steel. This attenuation is frequency-dependent and attenuates higher frequencies stronger than the lower ones. Effectively, removal of the high frequency components of the bell-shaped FT signal will shift the central frequency toward the lower values.

(a)

(b)

(c)

(d)
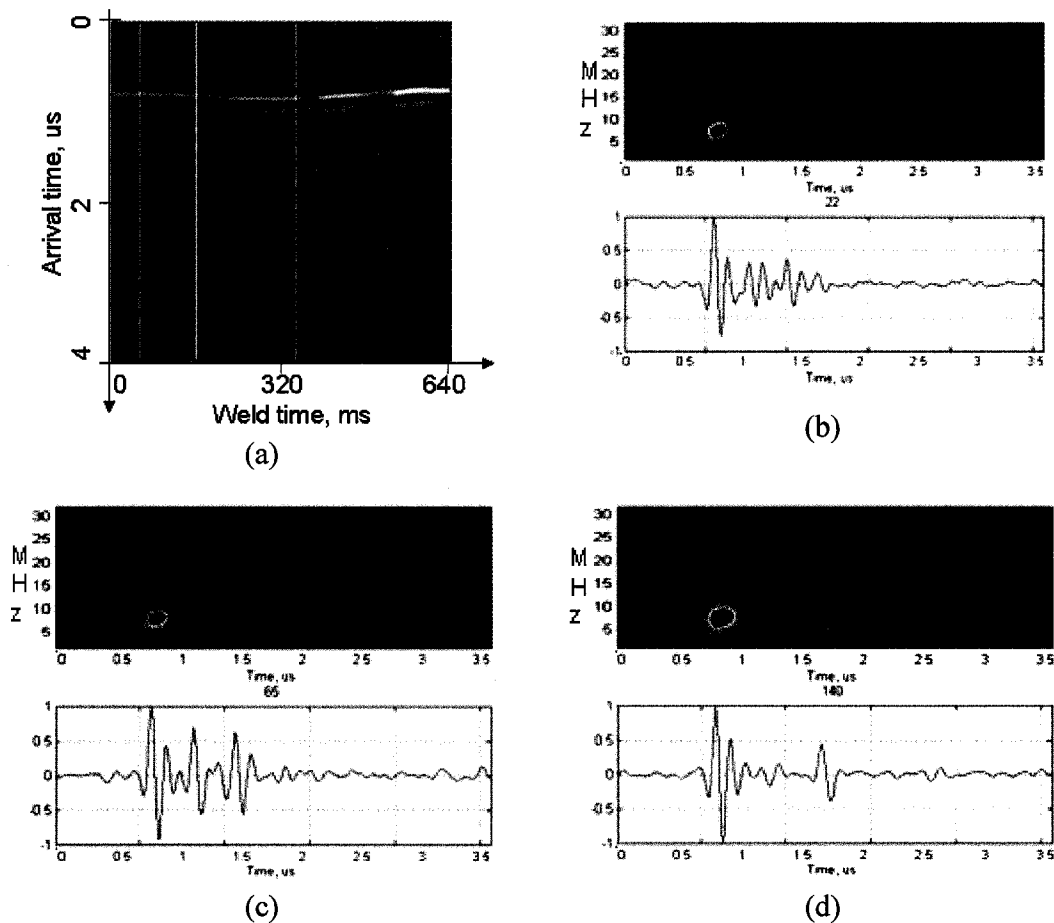
Figure 28. STFT of three A-scans from different parts of the B-scan. (a) B-scan of the good weld; the white vertical lines define the positions of three analyzed A-scans; (b) A-scan 22 and its STFT; the local maxima are depicted with the purple circles - their vertical positions are the same; (c) A-scan 65 and its STFT; (d) A-scan 140 and its STFT; the central frequency of the first interface is higher than that of the last one. Due to wave passing through liquid metal, high frequency components attenuate faster.

Another four pictures represent another scan with the solid-liquid interfaces better visible. Also, on these STFT pictures, every FT signal was normalized before putting it

54

into the STFT picture. It somewhat changes the perception of the same process and brings a different view to it. The local maxima are not marked on these pictures as they make little sense in two dimensions when every vertical component (every column) of the picture is normalized. One can see here that there is no visible frequency attenuation happening in the cold steel plates or even in the heated ones. Only when liquid metal is present within the sample, can it be observed that the frequency attenuation shifts every subsequent reflection more and more towards the lower frequencies.

(a)   (b)

(c)   (d)
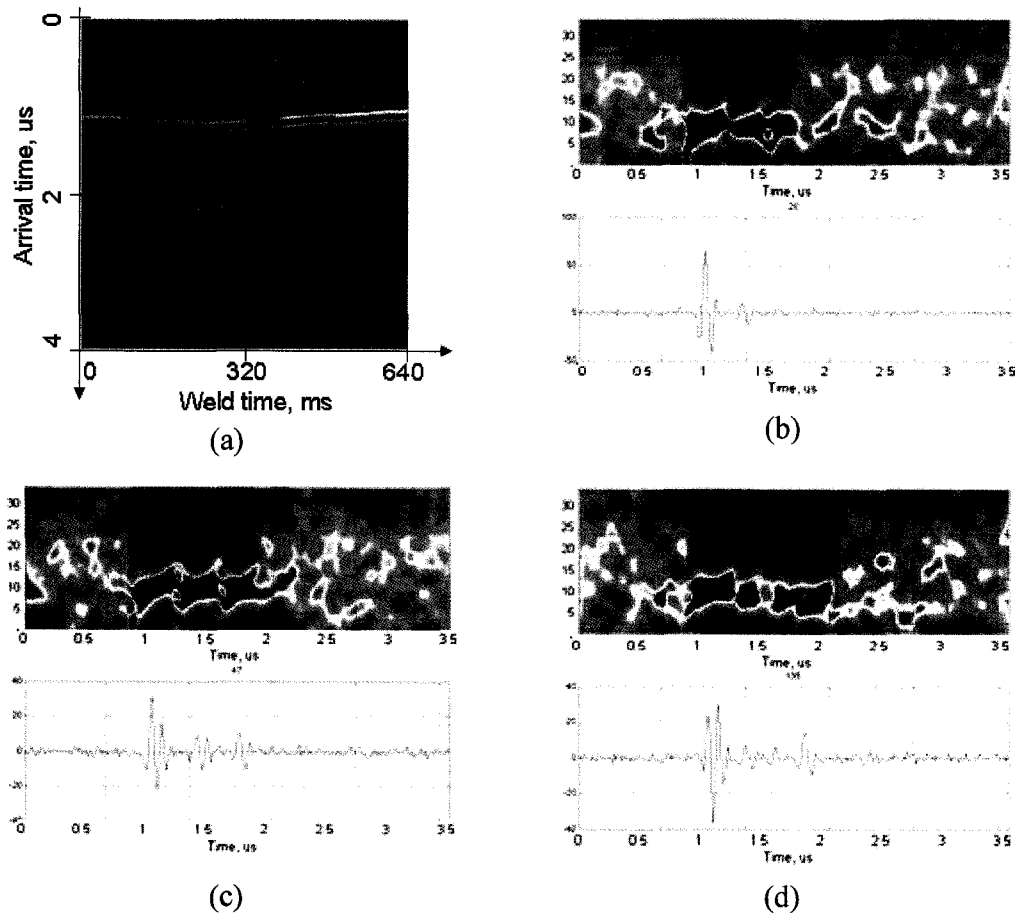
Figure 29. STFT of three A-scans from different parts of another B-scan. (a) B-scan; (b) STFT of A-scan 20; (c) STFT of A-scan 47; (d) STFT of A-scan 135. Every FT vector of the STFT image is normalized to show another way of looking at the STFT image.

10. Estimation of the BUA in the Liquid Steel Layer

The STFT method provides the possibility of determining the frequency content of different signals within a single A-scan. The method was used to separate the first

55

reflection coming from the copper-steel interface (not affected by the liquid layer) and the last one, which has passed through the liquid steel and reflected at the far end of the stack-up from the steel-copper interface. Figure 30 shows the original A-scan and the windowed signals of interest.

(a)

(b)
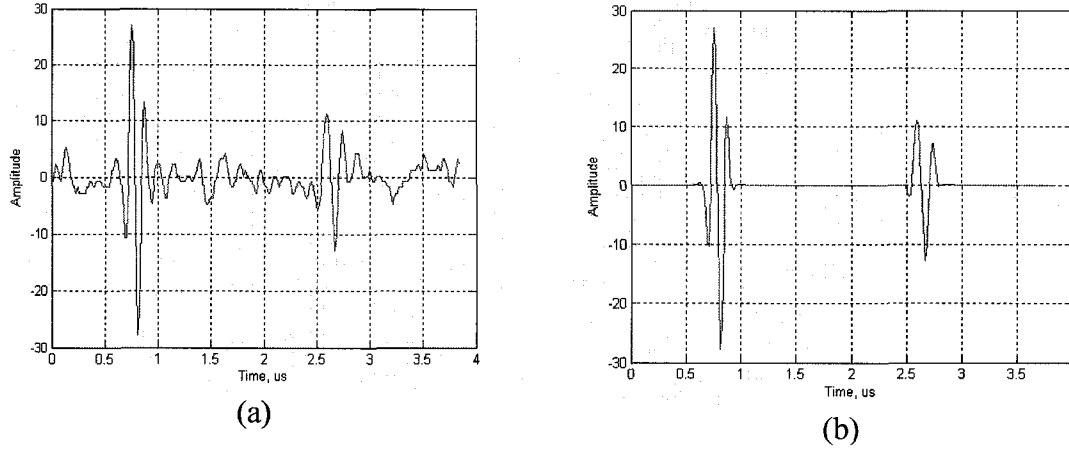
Figure 30. Original (a) and corresponding windowed (b) signals.

For each of the two windowed signals, a separate Fourier transform was obtained. The absolute values of the transforms were divided to obtain the frequency response of the medium. The results are presented at Figure 31. The upper part shows the spectrum of original pulse (left, or, earlier in time domain) in blue, and the spectrum of the pulse transmitted through the liquid steel area twice – on its way forth and back, in red. It can be easily seen that the pulse has lost its higher frequency components more than its lower ones. The ratio of the spectra is presented at the lower part of the Figure 31. Only the range between 3 MHz and 12 MHz is of interest as it represents the bandwidth of the original pulse. The ratio going above one in the lower frequency range is of no interest as it is affected by signals with low signal-to-noise ratios and may present erroneous data. The same thinking is applied for the frequencies above 12 MHz – the ratio of spectrums present meaningless data and are not considered.

The curve in the range of 3-12 MHz is very well approximated by the quadratic function having the attenuation as a function of ϖ^2, the same as predicted theoretically. The linear approximation of this curve (green dashed line) yields the linear frequency response of the medium for the signal travelling through the welded plates and back to the receiver. This approximation will be used to compensate the reference signal as will be shown later in this work.

56

The usual representation of the attenuation rate is given in the form Db/MHz which is simply the slope of the linear approximation of the signal pressure attenuation. For a given case the rate is estimated to be 1.2 dB/MHz. This very closely corresponds to the theoretically estimated value of 0.97 dB/MHz presented in section 7.
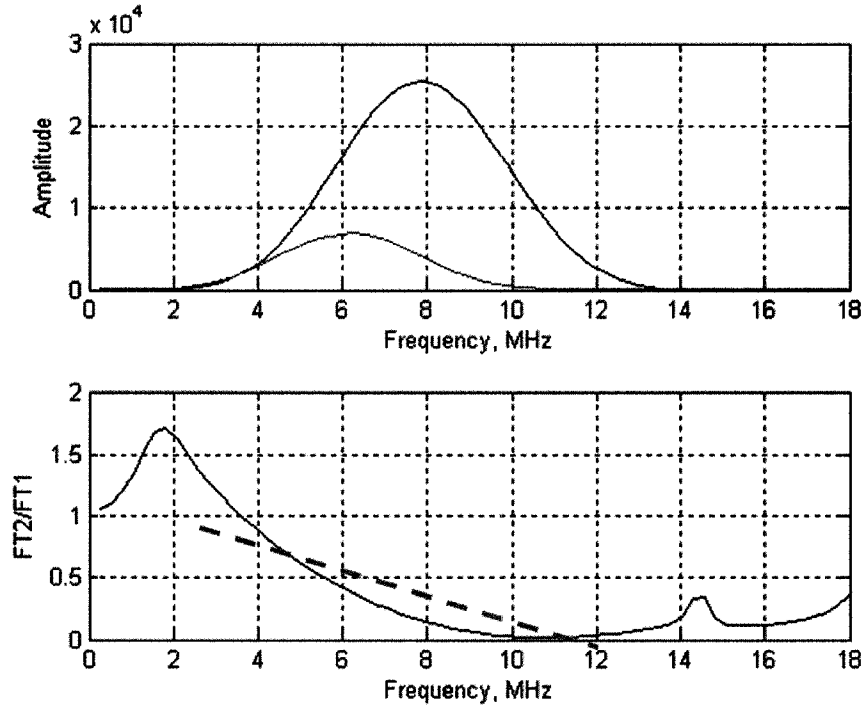
Figure 31. The Fourier transforms of the first and last interface reflections (top); the second reflection passed through the liquid steel layer twice (back and forth). Bottom picture – ratio of spectra; green dashed line is the linear approximation of the spectra ratio in the frequency range 3-12.5 MHz.

11. Modelling the BUA and its Effect on the Signal Shape

The simulation model has been developed in order to predict how waveform shape is changed with variations in attenuation [5, 6]. In this model, it was assumed that attenuation varied linearly with frequency (the attenuation coefficient was varied), and the dispersion was held fixed. This model also visualizes the waveform change due to the possible dispersion. A new signal processing technique [7], which compensates for the influence of frequency-dependent attenuation on the measurement of time-of-flight, was applied in order to overcome the artefacts caused by attenuation [8].

57

The attenuation causes losses of some frequency components and yields a signal shape change. Figure 32 shows the modelled shape change due to attenuation. The upper (blue) waveform is the original undistorted Gaussian pulse, and the lower (red) one is the signal after attenuation. Spreading of the signal can easily be seen. If, for example, the first zero-crossing was chosen as a marker to locate the wave, the error will shift the measurements towards the earlier times. If the last zero-crossing is used, the error will contribute towards propagation time increase. The same thing would happen for various peak tracing techniques. Thus, the transit time differential will depend on which reference point pair is used.

The following mathematical approach will show the way such an attenuation process is modelled. To model the process, the effects of attenuation are presented as a linear filtering process. The calibration signal (the reference signal) is denoted by $x(t)$. The impulse response of the linear filtering process is denoted by $h(t)$. The signal passed through attenuating media is $y(t)$

$$y(t) = h(t) * x(t) .$$

Here the $*$ sign means convolution – the effect of the passing of the signal through the filter. The transfer function, the Fourier transform of $h(t)$, may be modeled as follows:

$$H(f) = \exp(-\beta(f)fd)\exp(-2\pi f \Delta t) \tag{45}$$

where f is frequency, β is the frequency-dependent attenuation coefficient of the sample (sometimes referred to as normalized broadband ultrasonic attenuation), d is the thickness of the sample, and Δt is the time delay (relative to the reference signal).

The input or reference signal, $x(t)$, may be assumed to be a Gaussian-modulated sinusoid. The analytic signal representation is given by

$$x(t) = A\exp\left(-\frac{t^2}{2\sigma^2}\right)\exp(i2\pi f_0 t)\exp(i\varphi_0), \tag{46}$$

where A is the amplitude, σ is a measure of the duration of the pulse, f_0 is the center frequency, and φ_0 is the initial phase. The dispersion is assumed to be negligible according to different researchers [9] and the current investigation in the 3-15 MHz frequency range.

58
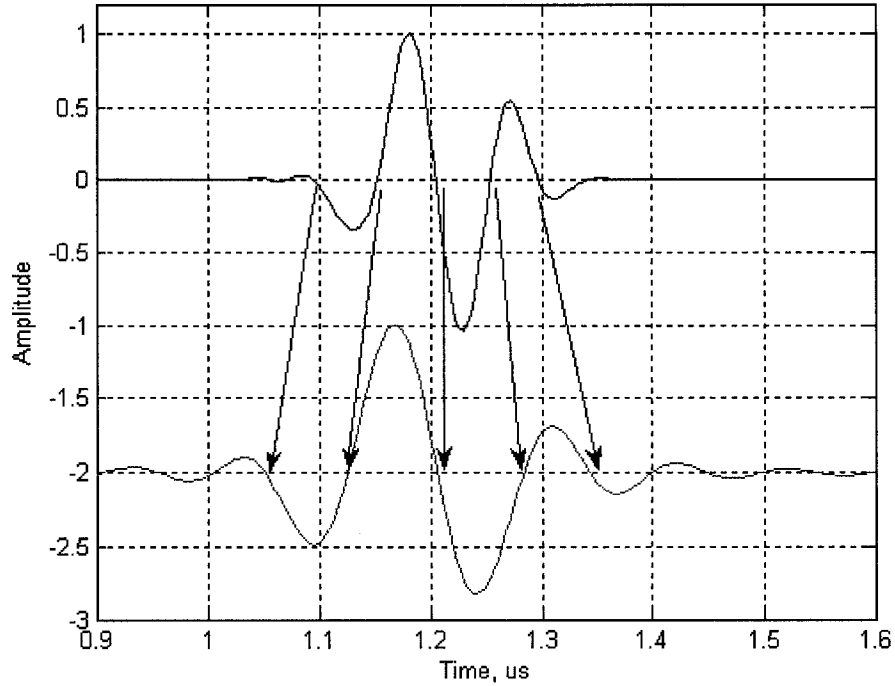
Figure 32. The original waveform (blue) and attenuated one (red). It can be seen how different zero-crossings change their relative positions.

As β runs from lower to higher values the signal changes more noticeably as more frequency components are attenuated. In Figure. 33 the sequence of six different attenuation slopes shows the dynamics of waveform modification. The attenuated signal resembles the original one less and less and the precision of the measurements reduces considerably.

In order to compute $Y(f) = H(f)X(f)$, it was necessary to define the attenuation. This function had to be modified from $\exp(-\beta f d)$ to $\exp(-\beta|f|d)$ since the Fourier transform corresponding to any real signal contains negative as well as positive frequency components.

The simulated received time-domain signal, $y(t)$, was obtained from the inverse Fourier transform of the product $H(f)$ and $X(f)$. Six different degrees of attenuation were tested based on the real attenuation measurements described above. The attenuation slope was ranged from 0.46 dB/MHz to 1.2 dB/MHz, which covers the measured value from the experiment.

59
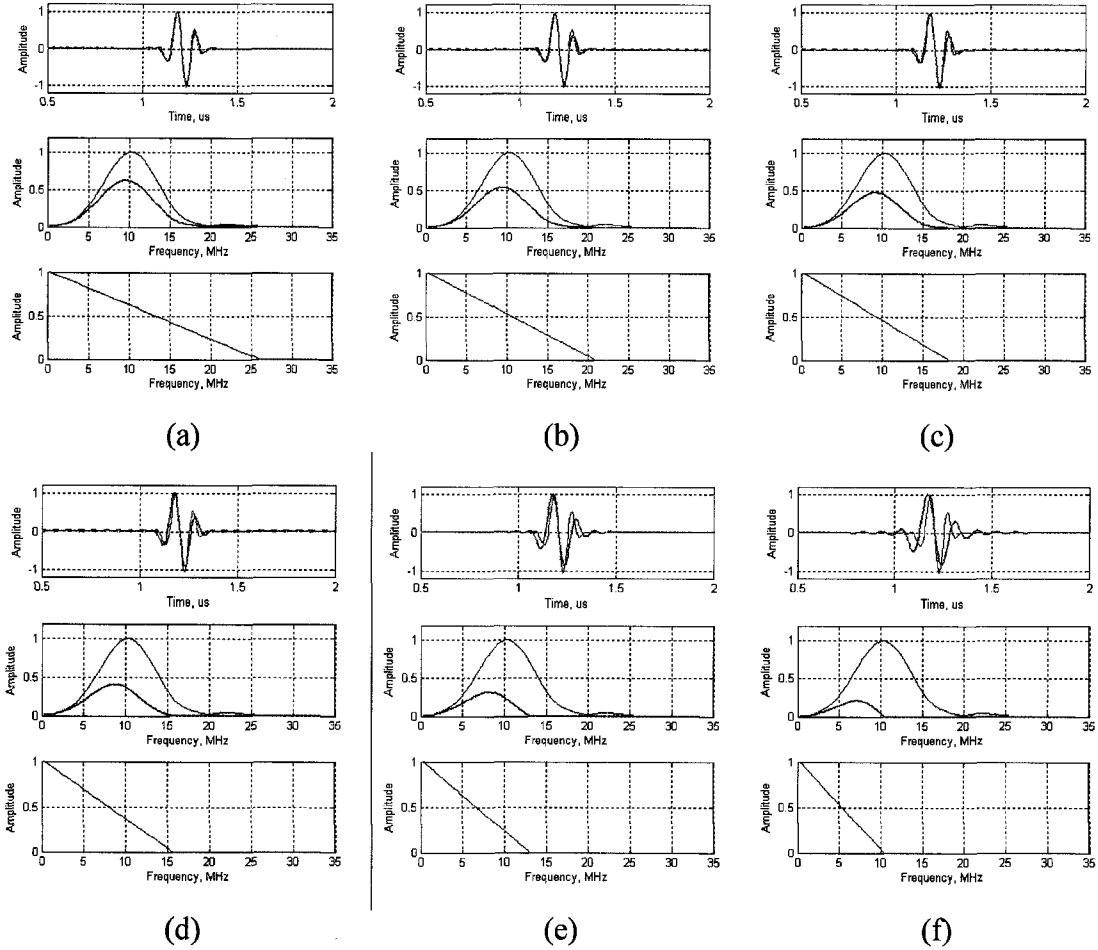
Figure. 33. Waveform shape change as the attenuation slope increases. Each 3-graph set is made of (from top to bottom) time-domain waveform, its Fourier transform (absolute value), and frequency response of the transfer function. Attenuation slope is changed gradually from 0.46 dB/MHz to 1.2 dB/MHz.

Each of the images consists of three sub-images depicting from top to bottom: the time-domain signal, its Fourier spectrum and the frequency response of the modelled medium. The blue line in the time and frequency domains of the upper two sub-images represents the original reference signal. The red line corresponds to the attenuated one. The attenuated signal in the time domain was normalized to have the same amplitude as the reference signal (even though it is always smaller as the part of the energy is lost) in order to better visualize the waveform change. In the frequency domain the spectrum of the attenuated signal is not normalized and has the actual relative amplitude compared to the reference signal.

The obtained results were used to determine the error introduced by the frequency-dependent attenuation on the measurement of time separation between the signals.

60

Different markers in the time domain and phase slope in the frequency domain were used to determine the effect of the waveform change.

12. The Effect of Frequency-Dependent Attenuation on Different Measuring Approaches

Several different time- and frequency-domain techniques have been tried to establish the most precise measuring technique for a given application. Among the time-domain methods, the maximum peak tracing, and envelope maximum tracing, and the first-zero-crossing after 10% threshold tracing were chosen. For the frequency-domain approach the cross-correlation and the group velocity using the phase slope in the frequency range of the signal were tested. The reference signal has undergone a series of modifications to model the attenuation as shown is the previous section. The only difference is in representation of the signal location in time domain. In the previous section the signal was not shifted in time but only attenuated in order to ease the comparison of reference and attenuated signals, i.e. the $\exp(-2\pi f\Delta t)$ term in (45) was omitted. Now, the formula (45) was applied without omissions to model the time shift and attenuation, see Figure 34.

(a)
(b)
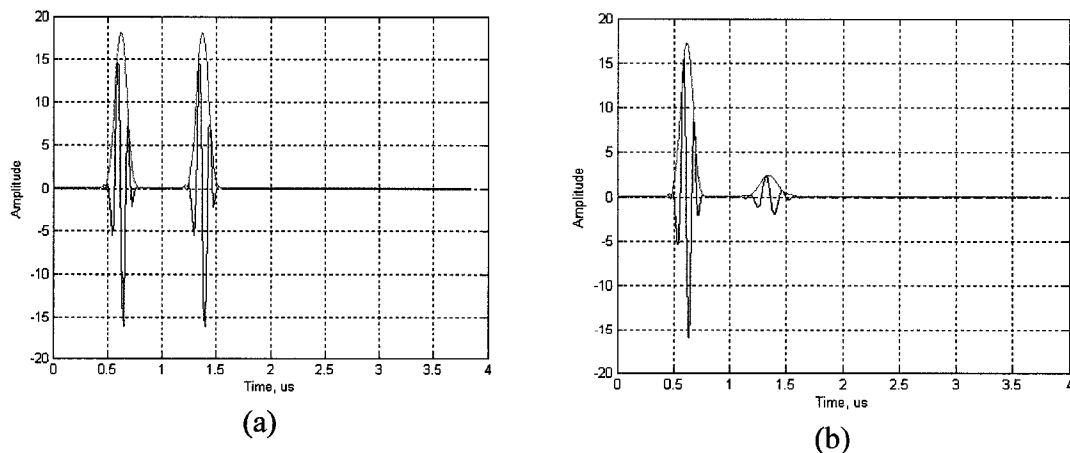
Figure 34. (a) modelling the signal shift in time domain; (b) modelling both the shift and attenuation of the signal using relation (45) for every frequency component.

The attenuated modelled signal was shifted by 0.75 μs with respect to the reference one. It was also gradually attenuated in the range from 0.46 dB/MHz up 1.2 dB/MHz. The

cutoff frequency was introduced to show where the filter frequency response crosses the horizontal frequency axis – i.e. what is the highest frequency the signal contains, as shown on Figure. 33 above.

The time separation was measured by both time- and frequency-domain techniques most widely used today.

The peak tracing technique allows the operator to choose a specific peak on the waveform and measure the distance between analogous peaks of the two signals, Figure 35 (a). As the signal progresses and reflects off the interfaces, the phase of the waveform can flip by π and an error of half the wavelength can easily occur. For that reason, the first zero-crossing after hitting a certain threshold level (say, 10% of the max amplitude) can be considered as a more robust and phase-inversion-safe technique, Figure 35 (b). Still, the shape is changing and the next level of complexity and robustness can be considered by the enveloping the signal using the Hilbert Transform (HT). The absolute value of the signal HT wraps around the positive half of the waveform having its peak in the waveform center of gravity, Figure 35 (c). The separation between the envelope peaks can be considered the time distance between the pulses. If the travelled distance is divided by this time, the group velocity of the signal can be determined.

<center>(a)   (b)   (c)</center>
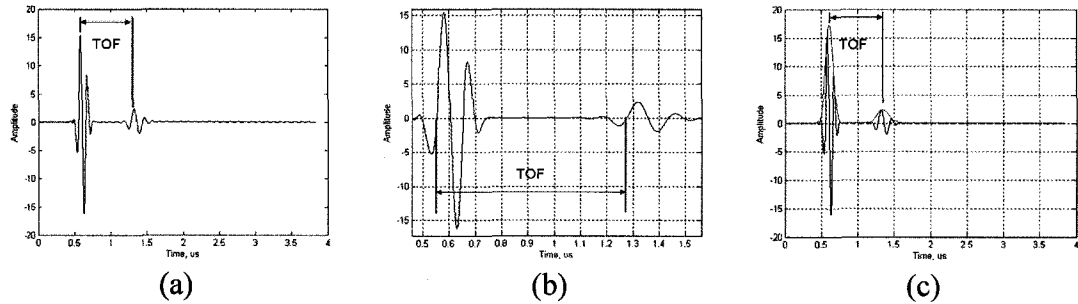
Figure 35. Different time-domain markers. (a) maximum peak marker; (b) first zero-crossing; (c) envelope peak.

The frequency domain can also be used to determine the separation between the signals. The cross-correlation of the reference and the test signal provides information about their separation. The cross-correlation is generally defined by the relation

$$h(t) * x(t) = \int h^*(t)x(x+t)dt .$$ (47)

The cross-correlation can be thought of as a convolution of the same signals when one of them is flipped front to back. The cross-correlation operation can be performed in the frequency domain as well. In cases when the signals are longer than 60-70 points, it is more calculation-efficient to perform it in the frequency domain. Convolution of the

<center>62</center>

signals in time domain is equivalent to the multiplication of their Fourier spectrums. The opposite is also true – convolution of signal spectra is equivalent to signal multiplication in time domain:

$$F|h * x| = (F|h|) \cdot (F|x|). \tag{48}$$

Cross-correlation enables the determination of the separation between the similar signals. The closer in shape they are the sharper the peak. The location of the peak determines how far apart the signals are. Figure 36 (a) shows a close-up of the results of the cross-correlation of the reference signal with the two shifted and attenuated. The height of the peak changes as the signal is attenuated, but the location stays the same.

Another frequency domain method employs the phase information contained in the signal. The usual spectrum of the Gaussian signal in noise is presented on Figure 36 (b), upper part. The phase at each frequency of the broadband signal for both reference and attenuated signals was calculated using the Fourier transform (FT):

$$phase = \arctan\left(\frac{\text{Im}(FT)}{\text{Re}(FT)}\right). \tag{49}$$

Due to the fact that the *arctan* is 2π-periodic, the raw phase is contained within the $-\pi...+\pi$ region. The real phase often goes far beyond these limits. A special routine has been used to unwrap the phase – it keeps track of the phase jumps which are over π and corrects these jumps to fit a continuous pattern. Figure 36 (b) shows that within the frequency range of the signal, the phase is close to the linear function and can be approximated by straight line. The slope of the line – the phase slope – can be used to determine the location of the signal. On Figure 37 one can see two identical pulses shifted in time. The Fourier transform applied to each of these signals separately allows the determination of their phase slopes. The later the signal arrives, the bigger the phase delay, or slope, will be. The difference between these phase slopes is the time delay between the signals, *time = phase / frequency* .

Application of STFT technique allows the visualization of the phase slope dynamics while moving along the A-scan. As the window of general form $\exp\left(-\frac{(x - shift)^N}{D}\right)$ slides along the A-scan and cuts short potions of the signal (Figure 38 (a)), the Fourier transform, phase angle and the slope of phase angle at every signal point can be calculated. The phase slope values are plotted against every location along the A-scan to

63

show the dynamics of this parameter (Figure 38 (b)). The areas of constant values of the slope correspond to the location of the reflected pulses; they are emphasized by horizontal green dashed lines. The wider the scanning window in time domain, the more pronounced the horizontal portions of the phase slope, Figure 39. At the same time, the time resolution drops as the wide envelope covers too much of an A-scan. Some compromise should be reached when selecting the width of the envelope to provide an acceptable time resolution and distinct plateaus of the phase slope.

(a)   (b)
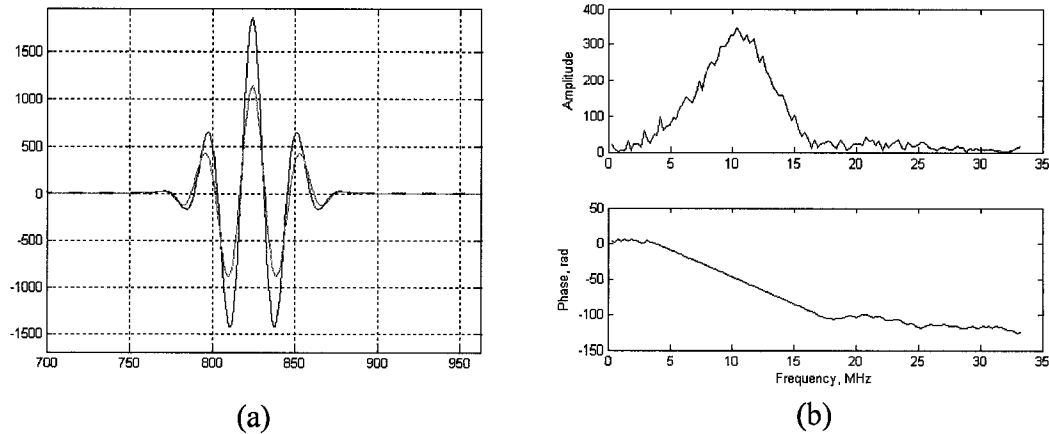
Figure 36. (a) cross-correlation of the first reflection and last reflection with the reference signal; (b) Fourier spectrum and the phase slope of the back-wall reflection.

(a)   (b)   (c)
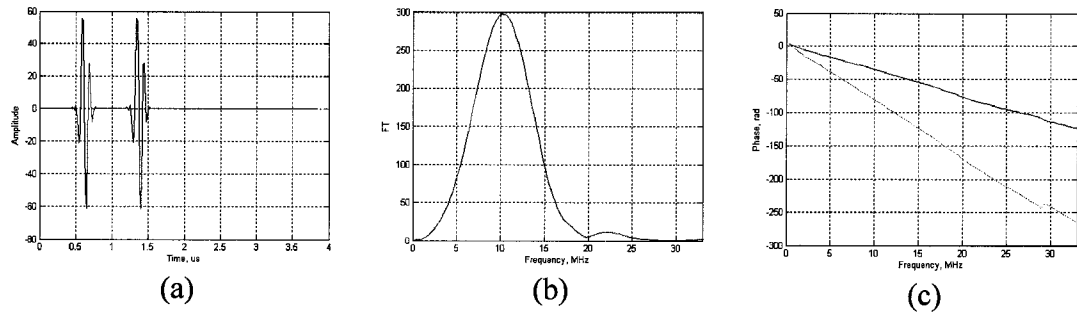
Figure 37. (a) two pulses shifted in time; (b) Fourier spectrum of separate pulse; (c) phase slopes of separate pulses; blue – for the first (left) pulse, red – for the second (right) pulse. Slope difference is the time delay between the signals.

(a)   (b)

64
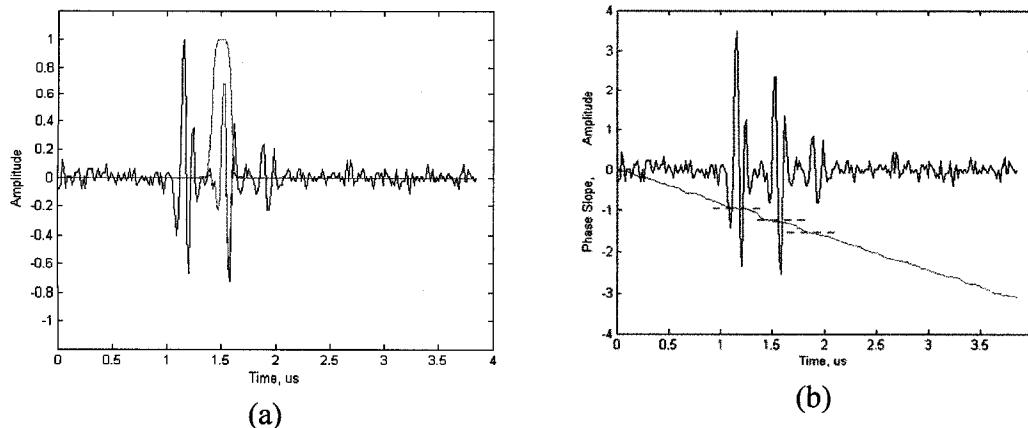
Figure 38. (a) window is sliding along the A-scan; (b) the A-scan and corresponding phase slope.
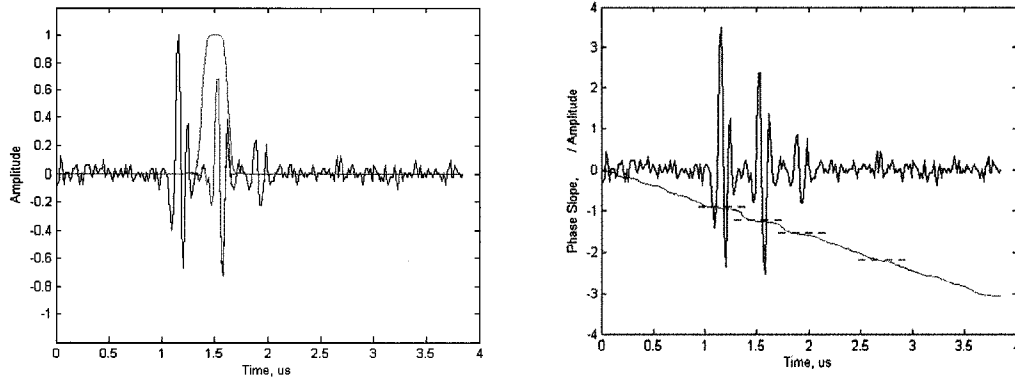
Figure 39. (a) wider window is sliding along the A-scan; (b) the A-scan and corresponding phase slope.

The time difference $\Delta t(f)$ could be measured with the following equation:

$$\Delta t(f) = \frac{\varphi_1(f) - \varphi_2(f)}{2\pi f}.$$
(50)

These time delays at every frequency can be used to determine the so called signal group velocity (if the travelled distance is known). The slope of the phase within the frequency range of the signal (in given case it lies within 4 MHz to 16 MHz) determines the integral delay of the pulse, the delay of the center of gravity of the pulse, or, the wave-packet delay. This value is more appropriate because the separate frequency components arrive at slightly different times and it is difficult to judge the actual arrival time of the signal based on it. Instead, the group delay (the phase slope) gives more informative values to work with.

(a)   (b)   (c)
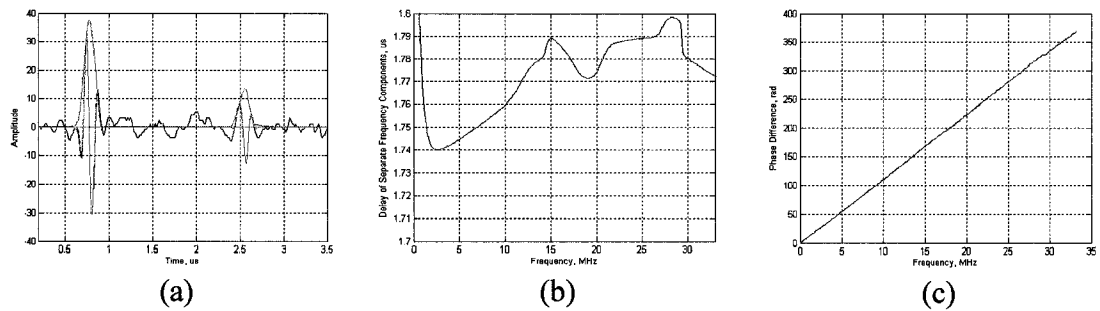
Figure 40. (a) A-scan with frontwall and backwall reflections marked by red and enveloped; (b) time delay of different frequency components; (c) phase difference between the backwall and frontwall reflections.

In the Figure 40 (a) the signal with a backwall reflection is seen. The delay between the envelope peaks is measured to be 1.785 μs, between the maximum peaks is 1.742 μs. With the phase slope difference, the separation was calculated to be 1.770 μs. Part (b) of Figure 40 shows that within the frequency range of the signal (4-12 MHz), most of the separate frequency components demonstrated lower phase velocity than the group

65

velocity calculated from the phase slope. This effect occurs due to some additional processes taking place in the medium such as dispersion.

Figure 41 shows the comparison of different measuring methods at different attenuation degrees of the signal. The model shows that the higher the attenuation slope in frequency domain, the less precise time-domain methods become (those using markers on the wavefrom).
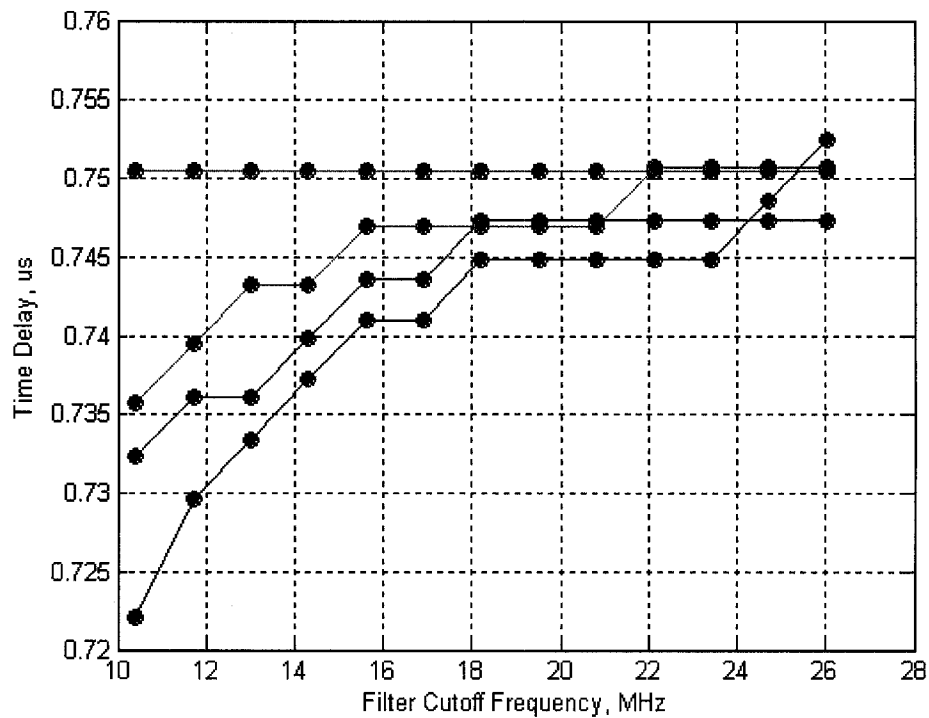
Figure 41. Time delay of the backwall reflection calculated with different methods. Red, blue and black lines show the dynamics of the measured delay at different degrees of attenuation for peak-to-peak, envelope-to-envelope and first-zero-cross-to-first-zero-cross respectively; the cross-correlation and the phase slope methods both gave the same results which are presented in green as they overlap each other.

In the absence of the non-linear phase shifts, which are possible in the dispersive medium, the signal changes its shape primarily due to the frequency-dependent attenuation. Figure 41 presents five techniques used to determine the time delay between the two pulses. Red, blue and black lines show the dynamics of the measured delay at different degrees of attenuation for peak-to-peak, envelope-to-envelope and first-zero-cross-to-first-zero-cross respectively. The cutoff frequency is the point where the frequency response of the medium-modelling linear filter is crossing the horizontal axis, in other words, the highest frequency the attenuated signal contains, see Figure 31 for reference. The cross-correlation and the phase slope methods both gave the same results

66

which are reflected presented in green as they overlap each other. The signal shape deformation did not affect the precision and stability of the measurement. The actual shift of the signal was 0.750 μs.

An additional source of uncertainty in the time-domain method comes from the finite sampling rate used to acquire the signal. At a central frequency around 9 MHz the sampling rate was 66 MHz. It means that for a central wavelength there are about 7.5 measurements. This fact explains the quantized pattern of time delay measurements. This effect of quantization can be counteracted, for instance, by increasing the number of points in the time domain using zero-padding of the signal Fourier spectrum. This method increases the time resolution. But even applying this method, the precision will drift as the signal spreads out in time.

The phase slope method is much more robust as every single frequency carries the same information about the delay of the signal. If some of the frequency components die out, the rest will still possess the information which can be extracted from the phase slope but within the narrower frequency range. There are still some drawbacks of the phase slope method. At the low SNR the phase slope method will be more erroneous.

There is also a way to increase the precision of the time-domain measuring methods. A two-step approach is applied to the signals, for which the delay needs to be measured [6]. The first step is to measure the BUA of the considered signal by comparing it to the reference signal. Then, in a second step, the attenuation filter described above is applied to the reference signal with the measured slope of attenuation. The time delay is then calculated by performing the comparison between this filtered signal (instead of the reference signal for the "classical" measuring method) and the signal which passed through the welded plates (the delayed one). This method is called the amplitude compensation method.

Figure 42 (a) shows the original signal and its STFT image. It can be seen that the central frequency of the backwall reflection is shifted towards the lower frequencies (down). Figure 42 (b) reflects the signal with waveforms of interest depicted in red and enveloped using HT. On Figure 42 (c) the Fourier transform is performed and the frequency-attenuation slope is derived. The slope is determined within the frequency range of the attenuated signal to counteract the artefacts appearing at low SNR regions.

67
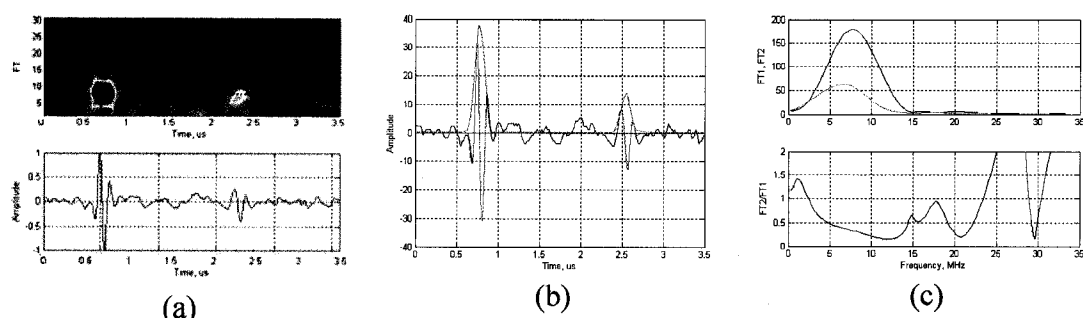
Figure 42. (a) the signal and its STFT; (b) the parts of the signal (red) used for analysis; (c) the Fourier spectrum of the frontwall pulse (blue) and of the backwall reflection (red) (top), and the spectrum ratio (bottom).

Application of the method on real signals demonstrates an increase in precision and brings the measurements by different methods closer together. One of the test results of this compensation method performed on the signal shown on Figure 34 (b) is presented below in the table. The phase slope and cross-correlation measurement gave the same result and were considered as true time separation between pulses. The measurements in time domain were either higher or lower than this value. Application of amplitude compensation on the reference signal brought each of these vales (second row) closer to the phase slope or cross-correlation result of 1.7763 μs.

Delay measured in μs	Envelope	Maximum Peak	First Zero Crossing	Phase Slope, Cross-corr.
Raw measurements	1.7868	1.7417	1.7289	**1.7763**
With attenuation compensation	1.7718	1.7568	1.7389	**1.7763**

Conclusions

The time delay between the two signals can be measured using different techniques. The time-domain measurements using markers on the waveform have shown to be the most sensitive to the pulse shape changes. The enveloping of signal allows the determination of the difference between the "centers of mass" of the signal, which is similar to the definition of the group velocity of the signal. According to Figure 41, the time delay determination using the signal envelope proved to be very stable up to the moderate levels of signal attenuation. The zero-crossing and peak tracing methods gradually shifted the delay value from even low levels of frequency-dependent

68

attenuation. The phase slope and cross-correlation methods have shown much better performance. In the absence of dispersion (which is very low for steel at the given frequency range), these methods demonstrated excellent performance giving a constant time delay at even stronger attenuation levels. According to other tests not shown here, the phase slope technique is capable of providing the highest accuracy for the group delay measurements (or group velocity) among the methods mentioned because it approximates the phase along the whole spectrum of the signal. For the applications with high SNR and good separation between pulses of interest (non-overlapping), this method is frequently the method of choice [12]. Still, at low SNR the phase slope can yield large errors, and it is best not to use it for weak reflections. The best option for signals with average and low SNR would be use of the cross-correlation technique because it provides both high precision and high confidence of measurements [13].

The measurement errors of time of flight using time-domain methods were estimated to be in the range of 2-8%. The high end of 8% errors could arise in case of phase inversion and measurement of the wrong peak. The use of amplitude compensation for attenuation provided improvement of the precision of up to 2-3%.

69

References

1. В.А. Красильников, В.В. Крылов. *Введение в физическую акустику*. Москва «Наука», Главная редакция физико-математической литературы, 1984. (Krasilnikov V.A., Krylov V.V. *Introduction to Physical Acoustics*, 1984, in Russian), pp. 9, 38.

2. Lawrence E. Kinsler et al. *Fundamentals of Acoustics*, fourth edition, Jojn Wiley & Sons, Inc, ISBN 0-471-84789-5, p. 210.

3. B. A. Auld. *Acoustic Fields and Waves in Solids*. Volume 1, second edition. Krieger Publishing Company, Malabar, Florida. ISBN 0-89874-782-1.

4. Karl F. Herzfeld and Theodore A. Litovitz. *Absorption and Dispersion of Ultrasonic Waves*. Academic Press, New York and London, 1959, p. 39.

5. K. A. Wear, *The Effects of frequency-dependent attenuation and dispersion on sound speed measurements: Applications in human tabecular bone*. IEEE Trans. Ultrason,, Ferroelect., Freq. Contr., vol. 47, no. 1, pp. 265-273, 2000.

6. Guillaume Haiat et al, *Effects of frequency-dependent attenuation and velocity dispersion on in vitro ultrasound velocity measurements in intact human femur specimens*. IEEE Trans. Ultrason,, Ferroelect., Freq. Contr., vol. 53, no. 1, pp. 39-51, 2006.

7. K. A. Wear, *A numerical method to predict the effects of frequency-dependent attenuation and dispersion on speed of sound estimates in cancellous bone*. J. Acoust. Soc. Amer., vol. 103, no 3, pp. 1213-1218, 2001.

8. P.M. Nasch and M.H. Manghnani, *Sound velocity measurements in liquid iron by ultrasonic interferometry*. Journal of Geophysical Research, Vol. 99, no. B3, pp. 4285-4291, March 10 1994.

9. Webber, G.M.B. and R.W.B. Stephens, *Transmission of Sound in Molten Metals*, vol. IV(B), edited by W.P. Mason, Academic, San Diego, Calif, 1968, pp. 101, 102.

10. **A. M. Chertov**, R. Gr. Maev, *Investigation of the Effects of Frequency-Dependent Attenuation and Diffraction in the Liquid Nugget of a Spot Weld on the Ultrasonic Signal*. To be submitted to IEEE UFFC.

11. P.H.F. Nicholson et al, *A comparison of time-domain and frequency-domain approaches to ultrasonic velocity measurement in tabecular bone*. Phys. Med. Biol. 41 (1996), pp. 2421-2435.

12. Berndt H. et al, *Using Phase Slope for Arrival Time Determination*. 14th International Symposium on Nondestructive Testing of Wood, May 2005, University of Applied Sciences, Germany, Eberswalde. Published by Shaker Verlag (ISBN 3-8322-3949-9).

13. D.R. Hull et al, *Measurement of ultrasonic velocity using Phase-Slope and Cross-Correlation Methods*. Technical paper presented at the 1984 ASNT Spring Conference, May 1984, Denver, CO.

14. Л. Ф. Лепендин, Акустика. Издательство «Высшая Школа» 1978. (L. F. Lependin, Acoustics, 1978, in Russian).

70

CHAPTER IV

Modelling the Ultrasonic Transducer Field

1. Introduction

The pulse-echo ultrasonic inspection of the materials is usually conducted using ultrasonic transducers. Such transducers convert the energy of electrical pulses into the mechanical vibrations or waves. The waves propagate in different directions depending on the beam configuration. When the wave encounters the acoustic mismatch between two media, part of the wave reflects back. Another part penetrates the second medium and continues its propagation. The wave loses its energy upon striking multiple interfaces and upon attenuating in the media. The reflected pulses return to the generating transducer and the mechanical oscillations convert back to an electrical signal by means of the piezoelectric effect.

A specially designed electronic device (commercially available in different variations) generates the high-voltage signal to induce mechanical oscillations of the piezoelectric crystal. Then, the device keeps silent for a specified time to "listen" for reflections coming back from the inspected sample. The series of reflections (an oscillogram, or A-scan) is sampled with an interval usually 6-10 times higher than the central wavelength of the pulse, or with frequency 6-10 times higher than the central frequency. This is done to satisfy the anti-aliasing criterion to have the Nyquist frequency higher than the signal bandwidth or the highest frequency component of the signal.

Once the signal dies out and all the reflections are received, digitized, and stored in memory, the procedure can be repeated. In the present application, the process repeats itself several hundred times over 0.25-0.50 s to make multiple snapshots of the inspected area. If the interior of the sample changes over time, a picture of the process dynamics can be created.

One of the major considerations to correctly interpret the received reflected signals is to understand what kind of signal is sent into the medium. Depending on both the signal wavelength in the given sample as well as the size of the emitting element, the picture can vary dramatically. The right choice of the signal wavelength and transducer size is important to obtain a meaningful picture of the process. The question is the

71

directivity of the pulse, i.e. what is the direction of propagation of the emitted energy. The sound is irradiated into a semi-infinite volume, and a general understanding of the beam directivity is required to correctly interpret the received reflections.

2. Transducer Field Modelling

To obtain an understanding of the transducer field distribution in semi-infinite space, a numerical model for pressure distribution was developed. It enables the proper design of the sound source in order to obtain the information required in the given experimental setup. The governing element in the transducer design choice is, definitely, the medium and/or the process being tested; they define the wavelength to be used for inspection. In the present case, steel plates of thickness ranging from 0.7 mm to 2.0 mm are commonly used for spot welding. They need to be tested for the internal discontinuities and interfaces. Having an average stack-up thickness near 2.0 mm, usually two plates welded together, the wavelength of use was estimated to be 0.5 mm. Up to 4 wavelengths can fit within the average thickness sample which is enough to distinguish between internal interfaces separated by ~0.3-0.5 mm. Shorter wavelengths may be more beneficial, but the compromise between the short wave and not-too-high attenuation needs to be established. For that reason, a central frequency of 10 MHz was chosen as an acceptable value for the tested medium. 10 MHz transducers are commercially available and can be easily assembled. This frequency yields longitudinal wavelengths of ~0.55 mm in mild steel. Because transverse waves can not propagate in the liquid, which is essential for the setup, longitudinal waves are used. Longitudinal waves can easily propagate in both solids and liquids and thus can be used in the inspection of the materials during phase changes.

Upon selection of the working frequency and the wavelength, the transducer face size needs to be established for proper testing. The beam emitted by the oscillating plate needs to be as narrow as possible to minimize side reflections, which cause undesired interference. There is a general relation that defines the divergence angle of the emitted beam as

$$\theta = \sin^{-1}\left(0.61\frac{\lambda}{a}\right) \tag{1}$$

72

where λ is the central wavelength and a is the transducer face radius. In general, the smaller the emitter, the more divergent the beam. As a rule of thumb, the smaller the emitter, the more it resembles a point source that emits uniformly in all directions; the smaller the ratio between the wavelength and radius, the more collimated the beam. The product of the face radius and the wave number, ka, is sometimes used to characterize the transducer. This number defines the property of the transducer and its applicability for the problem.

The physical arrangement is shown in Figure 43 [1]. A high-frequency, short duration electric pulse is applied to the quartz crystal, which causes the crystal to vibrate by means of the piezoelectric mechanism. This vibration is propagated into the medium and reflected up and down between the top and bottom surfaces. Every time the pulse strikes the quartz, a very small part of its energy is converted back to electrical energy, which is amplified and observed on the oscilloscope.
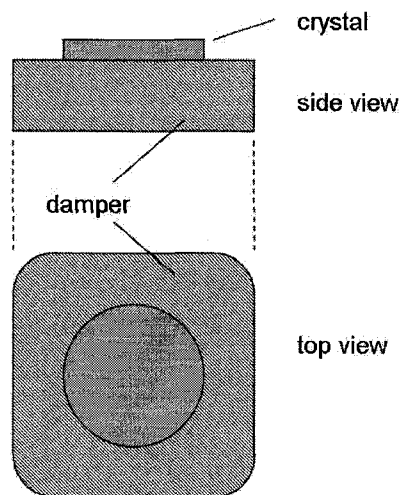
Figure 43. Schematic view of the piezoelectric transducer.

It is assumed here that the crystal vibrates uniformly and harmonically as a circular piston, and that the electrical response of the crystal is proportional to the average pressure over the crystal at a given time.

Although this problem has received considerable attention for a long time, there has been an increasing interest in it within recent years. The fact that the integral form of the solution for the field cannot be expressed in terms of elementary functions has resulted in the development of various expressions and approximation schemes for different cases. Here the main interest is in cases where the values of ka are large, i.e., the wavelength is considerably shorter than the radius of the source.

73

Several exact expressions for the field are used to deal with this problem. The methods used to derive these expressions are essentially the same. They all reduce to finding the solution for the equation

$$\left(\nabla^2 + k^2\right)\psi = 0 \tag{2}$$

which satisfies the boundary conditions $\partial\psi / \partial n = const$ for $x \le a$ and $\partial\psi / \partial n = 0$ for $x > a$ on the boundary.

One of these expressions is due primarily to the analysis made by Bouwkamp [2]. Another exact expression is that due to King [3]. King derives his expression from a generalized solution in cylindrical coordinates

$$\psi_P = V_0 a \int_0^\infty \exp(-i\mu z) J_0(\lambda x) J_1(\lambda a) \frac{d\lambda}{\mu} \tag{3}$$

where ψ_P is the velocity potential at the field point P, $V_0 = \partial\psi / \partial n$ at the source, and $\mu = \sqrt{\lambda^2 - k^2}$. z and x are cylindrical coordinates of the point P.

Another exact expression is the oldest and most widely known. It was introduced by Rayleigh:

$$\psi_P = -\frac{V_0}{2\pi} \int_S \frac{\exp(-ikr)}{r} dS , \tag{4}$$

where r is the distance from the point P to the surface element dS. The same problem was investigated for the light waves and the similar result was derived using Huygens' principle. For the acoustic pressure the Rayleigh integral will take the form

$$p(x,\omega) = \frac{-i\omega\rho v}{2\pi} \int_S \frac{\exp(ikr)}{r} dS . \tag{5}$$

Modelling of the field pressure was performed applying the above formula using computer a numerical integration technique. The emitting circular crystal was divided into small rectangular pieces. Most of the transducers used are circular as is the case in the present work. The important property of the numerical calculation techniques is the fact that any shape of the emitting transducer, including 3-D, can be easily reproduced in the model. For exact analytical models, they represent near impossible challenges.

In the numerical model, the transducer emitting area is divided into small squares. Every square is considered as a point source for mechanical waves. This assumption is valid in cases when the linear size of the surface element is smaller than the emitted

74

wavelength. For the ultrasonic transducer emitting in water at frequency 10 MHz with a central wavelength of ~0.15 mm, the size of the square element was taken as 0.03 mm. In order to calculate the field pressure at a given point in space in front of the transducer the amplitude and phase of the divergent spherical wave emanating from every square element is calculated. The superposition of every wave at a given point yields the field pressure. It should be kept in mind that the superposition principle is valid only in the linear approximation limit when the distortions of the medium caused by the wave do not change the physical properties of the medium. In other words, such linear approximations work only for very small oscillation amplitudes. Still, as long as the regular sound waves used for testing have an amplitude in the range of 10^{-7}-10^{-5} m, the linear approximation works fine for most materials, including water and steel involved in the given setup.

A program written in MATLAB (the MathWorks Inc.) was used to calculate the field distribution in front of the transducer in the region of ± 8.8 mm from the center and 150 mm along the transducer axis (see Appendix A) [4]. The transducer radius was chosen to be 3.0 mm which by technical specifications satisfies the required intensity and the geometry of the transducer housing. The calculations were carried out for the circular transducer emitting into water. To see the difference in the choice of transducer frequency, a set of wavelengths was defined and the field distribution was calculated for each. The first wavelength was chosen well beyond any reasonable limits – 7.0 mm in water (214 kHz); the final wavelength was 0.15 mm (10 MHz), which was thought to fit the tested sample. The task was to see the beam divergence and to predict whether the strong side lobes would affect the measurements. Figure 44 shows the sound field pressure in water created by the transducer emitting a continuous wave of different frequencies. It is easy to see that as the wavelength decreases, the directivity of the emitted beam becomes increasingly defined. The side lobes reduce, and more of the field energy concentrates directly in front of the transducer. The intensity of the beam increases farther away from the emitting surface. The intensity of the pressure is presented using a color marking scheme. Each color defines a specific range of the pressure intensity. The full range of intensities within the figure is divided into equal sub-ranges and a color is assigned to each. Figure 45 represents the color scheme used with dark blue being the lowest intensity and dark brown being the highest. The transducer face is located in the center of the left vertical axis and depicted in yellow.

75
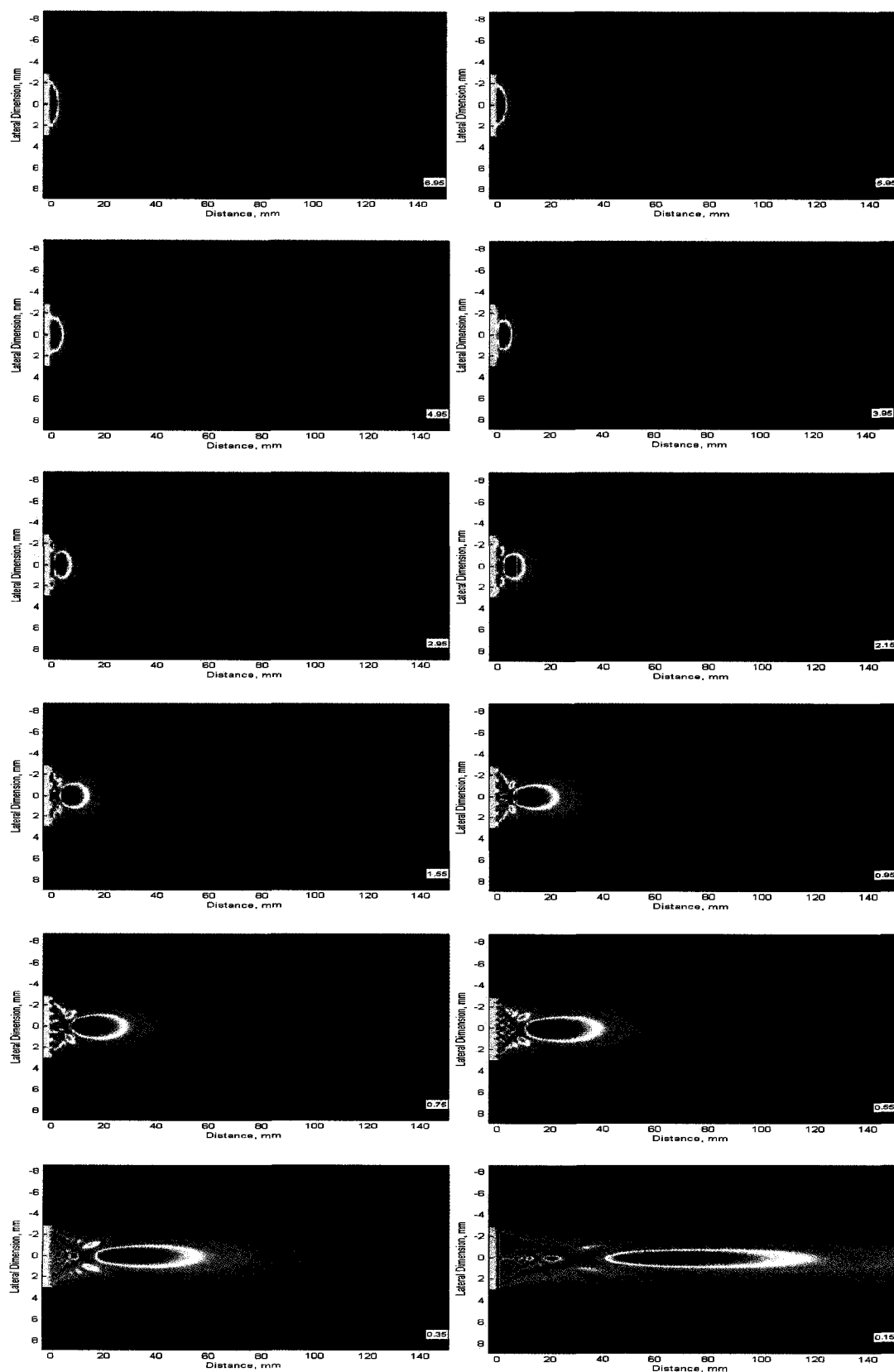
Figure 44. Sound field emitted by the 3.0-mm radius transducer into the water with different frequencies. Corresponding wavelength in mm is shown on each picture in the right lower corner.

76

Figure 45. The colorbar used to mark the sound intensity.

Figure 46 depicts the axial pressure of the transducer emitting at 214 kHz and at 10 MHz, 7.0 mm and 0.15 mm wavelengths respectively. The red line representing the axial field at a 7.0 mm wavelength (emitter radius 3.0 mm) shows the $1/R$ pressure decay much earlier than for the 0.15 mm wavelength (blue line). As such, the field tends to resemble a spherical divergent wave for lower frequencies, or smaller ka products. The 0.15 mm wave ($ka = 125$) begins to diverge as a spherical wave much farther from the emitting piston. In real life transducers, the ka value usually ranges from 50 to 1000. Obviously, this product value of 2.7, which is the case for a 7.0 mm wave, is not applicable for the method in use. Still such emitters can be applied in other areas of testing in cases when a uniform field distribution is needed in all directions.

The blue line of Figure 46, the axial pressure of the 10 MHz transducer, allows the easy visualization of the near and far fields of the transducer, which are also called the Fresnel and the Fraunghofer zones respectively. These two zones are separated by the value

$$S = \frac{a^2}{\lambda} \tag{6}$$

which is a frequently used characteristic of the transducer. The distance from the transducer is often measured in units of S. At this point the last field maximum occurs. Starting from this point and farther into the medium, the field behaves increasingly like a divergent spherical wave with its amplitude dropping inversely proportional to the distance. In the near zone, the field is more diverse and experiences large fluctuations in intensity from point to point.

For the given case of the transducer, the calculated S value is 60 mm ($a = 3.0$ mm, $\lambda = 0.15$ mm). This is the point of the field maximum. The result perfectly matches the numerical model of the field in Figure 47 with the field maximum located 60 mm from the source.

77
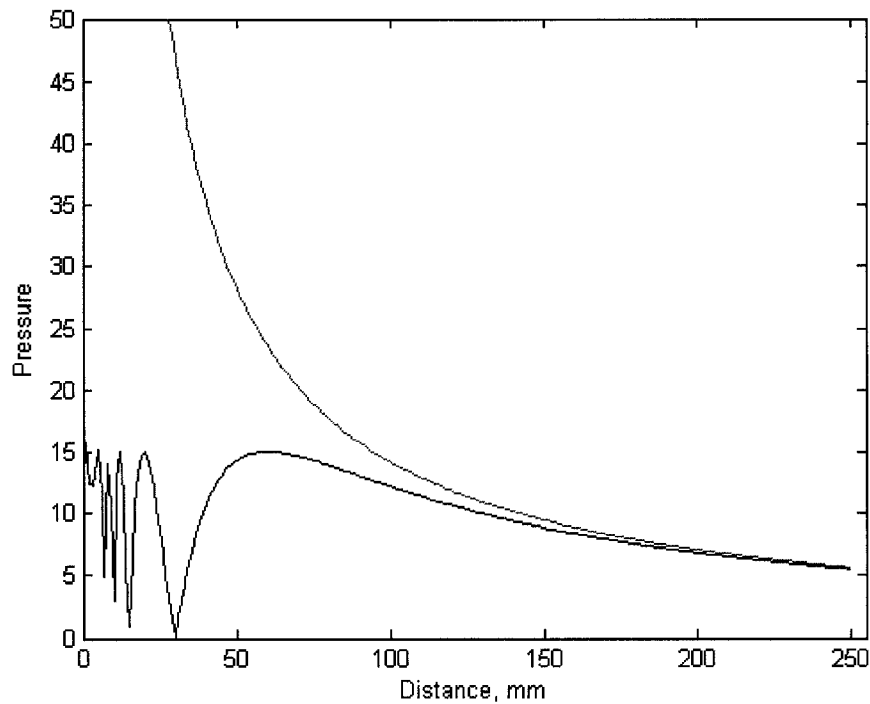
Figure 46. Axial pressure of the transducer field of wavelength 0.15 mm (blue) and 7.0 mm (red).

Figure 47 and Figure 48 present a more detailed analysis of the field calculated up to 250 mm into the water. It shows the pressure distribution for the 3.0-mm radius transducer emitting waves of 0.15 mm in water. The main beam divergence is very low, 1.7 degrees and according to calculations, which is a desirable feature in the given application. Several vertical sections of the field were selected to demonstrate the field distribution perpendicular to the transducer axis; these are shown in Figure 48. The field is very diverse in the Fresnel (near) zone due to large phase variations in the waves coming from different emitter points to the given point in water. It can be observed in the four pictures in the upper row of Figure 48 at distances of 5, 25, 45, and 65 mm from the transducer. The farther the point of interest from the emitter, the smaller the phase difference between the waves emitted from different parts of the piston. The Fraunghofer (far) zone is easily described with regular spherical waves; it can be observed in the four figures in the lower row at distances of 85, 105, 145, and 250 mm. The field distributions become increasingly more uniform and gradually reduce in amplitude, approaching an inverse distance dependence as in regular spherical wave.

78

3. Conclusions

The field analysis shows that the field structure is very non-uniform and has different properties at different distances from the emitting surface. Because of the finite size of the emitter, diffraction effects shine the field in different directions. The field energy is not confined to the geometric shadow area of the transducer but spreads non-uniformly in the semi-sphere. The ratio of the wavelength to the emitter size defines the field structure and the strength of the side lobes. In the given application, the field main lobe needs to be as narrow as possible to concentrate the energy in the region of interest. For the present setup, the sound frequency of 10 MHz satisfies both the wavelength requirements needed to distinguish the closely separated interfaces and also the field structure that is well collimated as seen in the model.

In the following chapters, the question of how such a field structure may affect the time of flight and attenuation measurements will be considered.
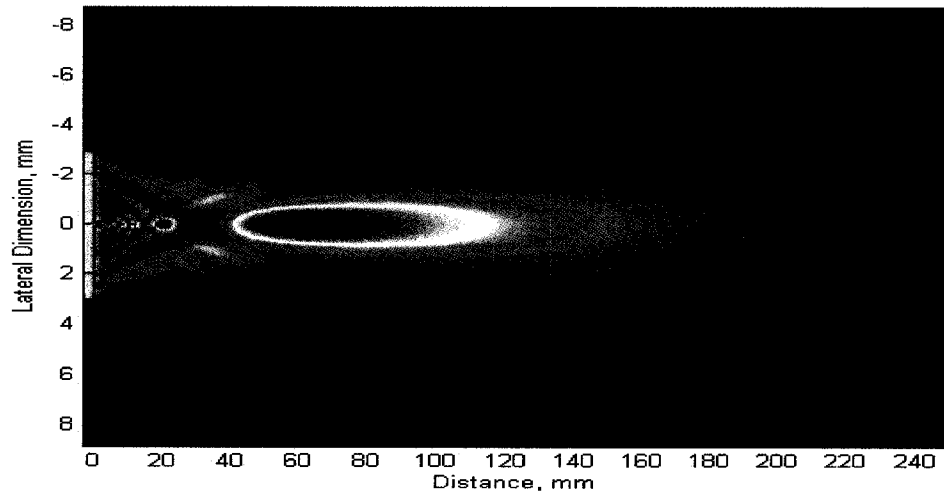
Figure 47. Field pressure in water created by a 6.0 mm transducer; transducer emits at 10 MHz (the wavelength in water is 0.15 mm).

5mm   25 mm   45 mm   65 mm

79

| 85 mm | 105 mm | 145 mm | 250 mm |
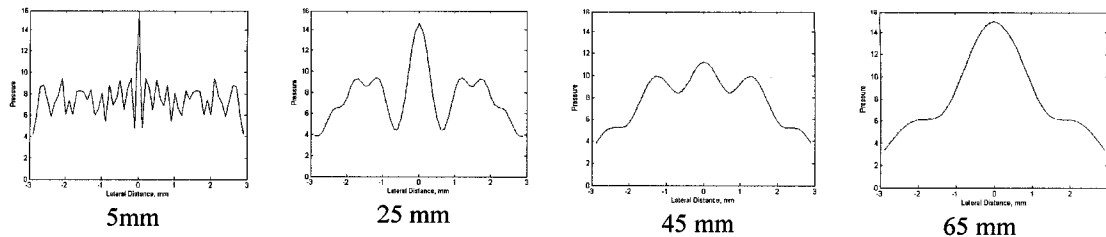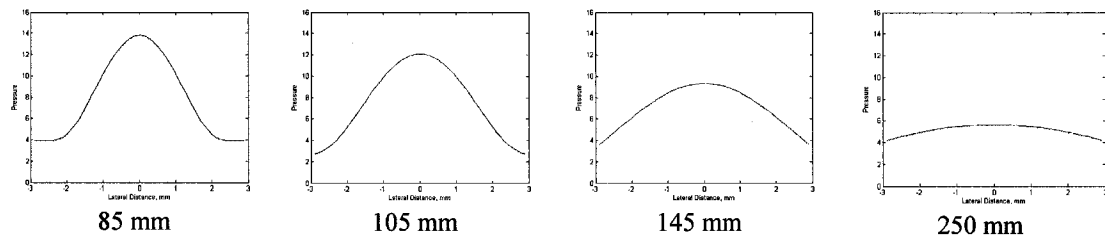
Figure 48. Sections of the field perpendicular to the transducer axis at different distances from the emitter.

References

1. Hajime Seki, Andrew Granato, and Rohn Truell, *Diffraction Effects in the Ultrasonic Field of a Piston Source and Their Importance in the Accurate Measurement of Attenuation*. The Journal of the Acoustical Society of America -- March 1956, Volume 28, Issue 2 pp. 230-238.
2. C. J. Bouwkamp, Dissertation, Groningen (1941), J. Math. and Phys. 26, 79 (1947).
3. L. V. King, Can. J. Research XI (1934).
4. **A. M. Chertov**, *Modelling of the Transducer Field for the Purposes of Resistance Spot Weld Inspection*. Report for DaimlerChrysler, Nov., 2005.

CHAPTER V

Investigation of the Diffraction Effects on the Field Losses

1. Introduction

The measurement of ultrasonic velocity is an important area in nondestructive testing. The information about sound velocity brings a greater understanding of the processes taking place inside the specimen. Various techniques for velocity estimation have been reported, from simple approach using pulse-echo-overlap [1] to more complicated methods using spectral analysis and cross-correlation.

Many factors affect the accuracy and precision of the ultrasonic velocity estimate, including temperature effects, digitization accuracy, methods of measurement [2]. The effects of frequency-dependent attenuation and sound dispersion [3, 4] introduce additional ambiguity into the measurements; these effects were considered in the previous discussion. Another factor influencing the velocity estimate is the effect of diffraction, i.e., the changes with depth of the sound field produced by the ultrasound transducer compared to planar wave propagation. Because of the finite size of the transducer, the acoustic beam spreads out into a complex and depth dependent field pattern, which can produce range-dependent effects associated with ultrasonic measurements. The field structure was considered in some detail in the previous chapter and will be used for reference purposes.

In many practical applications, the diffraction of a sound field is studied as one effect that influences not only the attenuation pattern of the signal by distorting the usual exponential sound attenuation, but and also the velocity measurements [5]. A majority of the publications reported the influence of diffraction on the measurement of ultrasonic attenuation, where its effect is more significant [6-14]. Early work on this subject was reported in [6], in which the diffraction loss was characterized as a function of frequency and the distance from the transducer.

81

2. Diffraction Losses in the Ultrasonic Field

In ultrasonic attenuation experiments carried out by pulse method, it is important to know the part of the measured attenuation that is contributed by diffraction in the ultrasonic field. In certain cases, for example, at the lower megahertz frequencies, the diffraction loss can be much greater than the attenuation intrinsic to the specimen. When attenuation occurs in a medium using the pulse-echo method, the echoes do not return from their round trips through the sample with an exponentially decreasing amplitude as would be expected if the loss in the sample were pure attenuation. Rather, the amplitude of the echoes is lower, and the curve connecting the tops of the echoes shows three peaks and associated points of inflection. The additional loss and fluctuation are ascribed to the diffraction of the ultrasonic beam. It can be computed as a function of penetration distance from the transmitter. The pressure and the decibel loss is seen by a receiving transducer, which is identical to the transmitting transducer and coaxial with it; another situation can involve only one transducer working in the reflection mode.

In order to simplify the analysis, various assumptions need to be made. Since the present concern is only with the diffraction and beam divergence, the medium is considered to be an ideal fluid. This problem will be treated as a circular piston source radiating into a semi-infinite medium, where $\partial \psi / \partial n = const$ the source and $\partial \psi / \partial n = 0$ along the rest of the plane boundary of the medium. ψ is the usual velocity potential without the time factor, and n is the normal to the plane, positive into the medium.

Finding the average pressure over the receiving crystal area involves two integrations: integration over the boundary of the piston source (Green's theorem) to get the diffraction field at the point of interest; and the integration of the field over the receiving crystal to obtain its response. Thus it involves two interference effects. The first is contained in the diffraction pattern, while the second is related to the fact that the wave front is not strictly planar, i.e., positive and negative pressures occurring simultaneously on different parts of the crystal area can give interference.

Therefore, in approaching this problem the ultrasonic field is first found in the medium. This part was accomplished in the previous section when the field pressure distribution was calculated in water. Then, assuming that the field does not change due to the presence of the receiving crystal, the field is integrated over the receiver area:

82

$$< p >= \frac{1}{\sigma} \int_{\sigma} pds \,.$$

(1)

Here, $<p>$ is the space average value of $p(x, z)$ over the crystal area σ. In general, the ultrasonic transducer field is also a function of time, and thus, technically, the calculations need to be performed for the maximum pressure during the period. Because the field was already calculated in the previous chapter for the maximum possible value, the calculations now need to be made only in the space domain.

The integration was carried out over the field previously calculated for the 3.0-mm radius circular transducer emitting into water at 10 MHz. The integration was made assuming the receiving transducer is aligned coaxially with the emitting one and has the same radius. This is a common setup in real world applications and similar to the present case. The integration was done for every pre-calculated point along the emitting transducer axis from 0 to 250 mm, with a step of 1 mm.
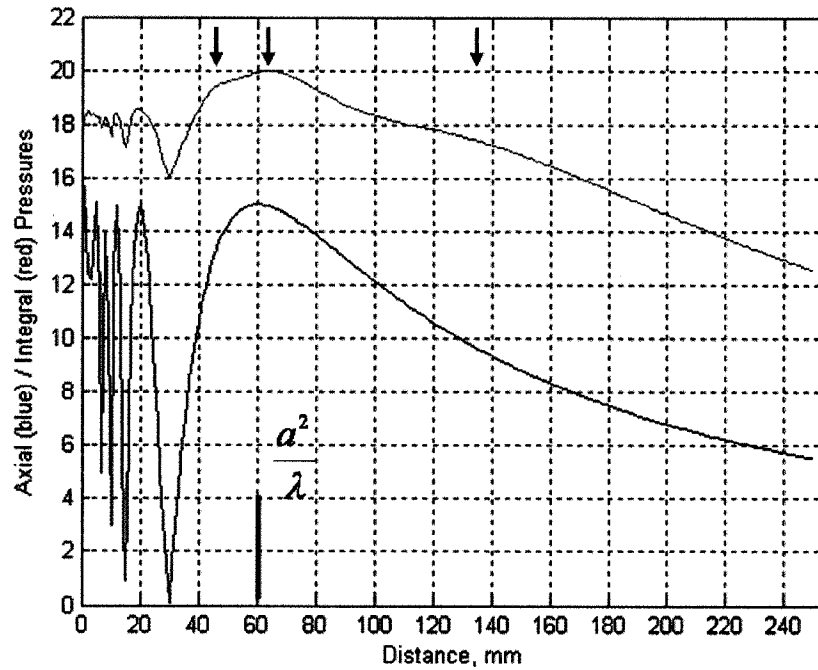
Figure 49. Sound field pressure. Blue – axial pressure, red – integral over the receiving transducer face (red curve amplitude was scaled by a factor of 25 to fit closely to the axial pressure amplitude).

The red line in Figure 49 shows the distribution of the integral pressure along the transducer axis in water. The axial pressure is depicted in blue for the reference. The integral pressure was scaled by factor of 25 to bring it closer to the axial pressure for the sake of demonstration. The inflection of the red line is apparent at around 110 mm. The

83

average sound field pressure does not decrease as steadily as the blue line for the axial pressure. An examination of Figure 50 explains this behaviour of the average (integral) pressure. The three lines depict the sound pressure along the transducer axis. The blue line is the pressure along the line originating from the transducer center; the green line is the pressure originating from a point one-half radius away from the center; the red line is along the very rim of the transducer – one radius away from the center. It can be seen that the last field maximum occurs at different points along the axis, – the farther from the center – the farther away into the medium. The integration of such a distribution along the receiving transducer surface yields uneven pressure distribution along the axis.

According to [6, 11] who partially based their calculations on results from [15], three peaks of the average amplitude at the receiver should be expected. Also, at some frequencies it is possible to observe these experimentally. The locations of these peaks are $0.73S$, $1.05S$ and $2.4S$ ($S = a^2 / \lambda$) and are noted by arrows on Figure 49. The peak at $1.05S$ is the most pronounced, while at $0.73S$ and $2.4S$ for a given frequency some inflections of intensity can be seen.
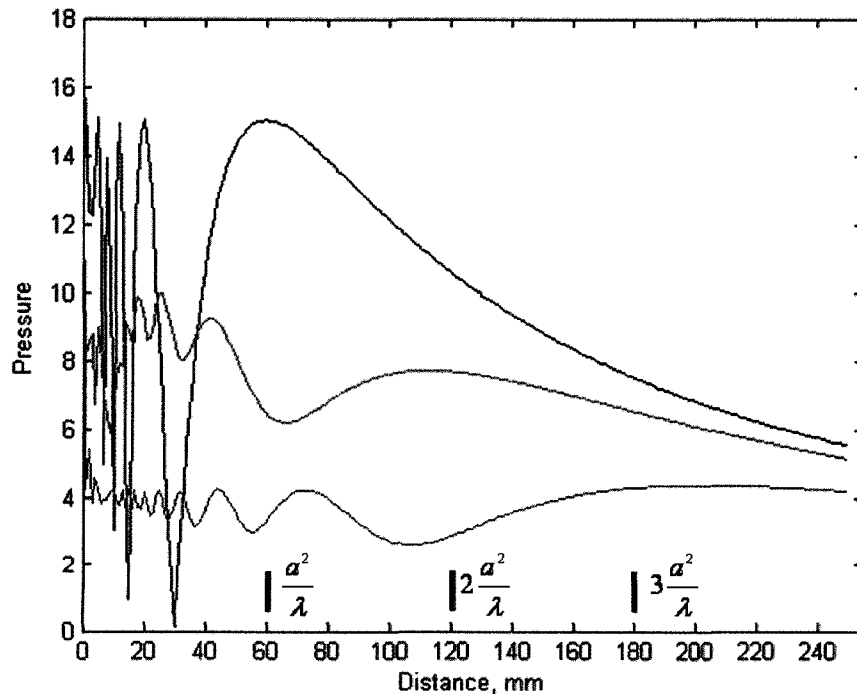
Figure 50. Sound pressure along the transducer axis; blue – in the circle center; green – half a radius from center; green – one radius from center.

The experimental measurements allowed a check of the calculations between 10 and 110 mm, which is the usual working range in the setup. The ultrasonic transducer was

84

attached to the transducer holder of the SONIX HS-1000 scanning acoustic microscope. The transducer was immersed in the water, and the reflection from the polished metal plate on the tank bottom was received by the same transducer. In such an arrangement (reflection mode), the distance between the emitter and the reflector needs to be multiplied by two to obtain the actual wave travel distance. The position of the transducer holder was gradually changed in the vertical direction and the amplitude readings were taken with a step of 0.5 μs (0.75 mm). The acquired measurements and the calculated results (red line of Figure 49) are presented in Figure 51. The overall picture of the measurements shows that calculations are very close to the experimental results.

The dB loss relative to the amplitude at $S = 1.05$ is plotted in Figure 52. This curve is important in determining the corrections necessary between any two points of measurement. As the curve seems uneven in different regions, its practical use starts approximately $1S$ distance away from the emitter. A linear approximation can be established as a good tool to estimate the attenuation caused by diffraction of the transducer beam. It is estimated to be around 1 dB per every S distance, which in the present case is 60 mm. The beam experiences reduction in amplitude by 1 dB as the test point is moved 60 mm away from the previous test point.

It is obvious that this amplitude reduction, accompanies the attenuation caused by the medium. These two mechanisms that cause amplitude drop are additive, and in linear problems can be considered as independent processes. The derived dB loss dependence can be utilized to estimate the diffraction effects on amplitude reduction compared to the attenuation in the medium. In highly attenuating samples the diffraction effects can be considered negligible. If the test is carried out on low-attenuating materials, such as single crystals of germanium, silicon or quartz, the diffraction effects can lead to different experimental and calculation errors.

This correction decreases with increasing frequency. In most cases, the attenuation of the specimen increases with frequency so that the diffraction correction is important only at the lower frequencies and becomes negligible at higher frequencies.

85
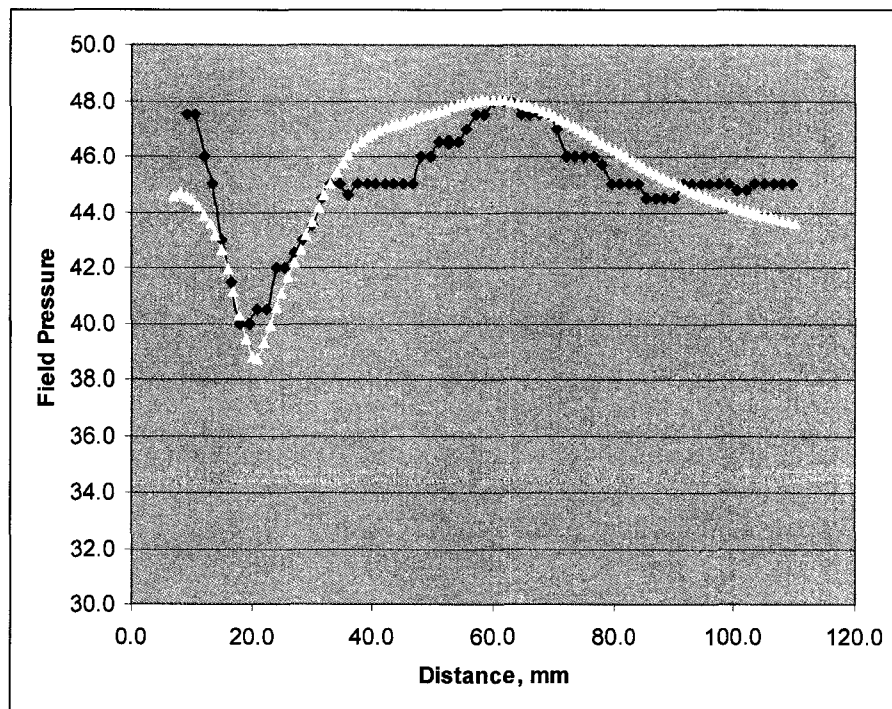
Figure 51. Modelled (yellow) and measured (blue) field pressure of the radius 3.0 mm circular transducer emitting in water at 10 MHz.
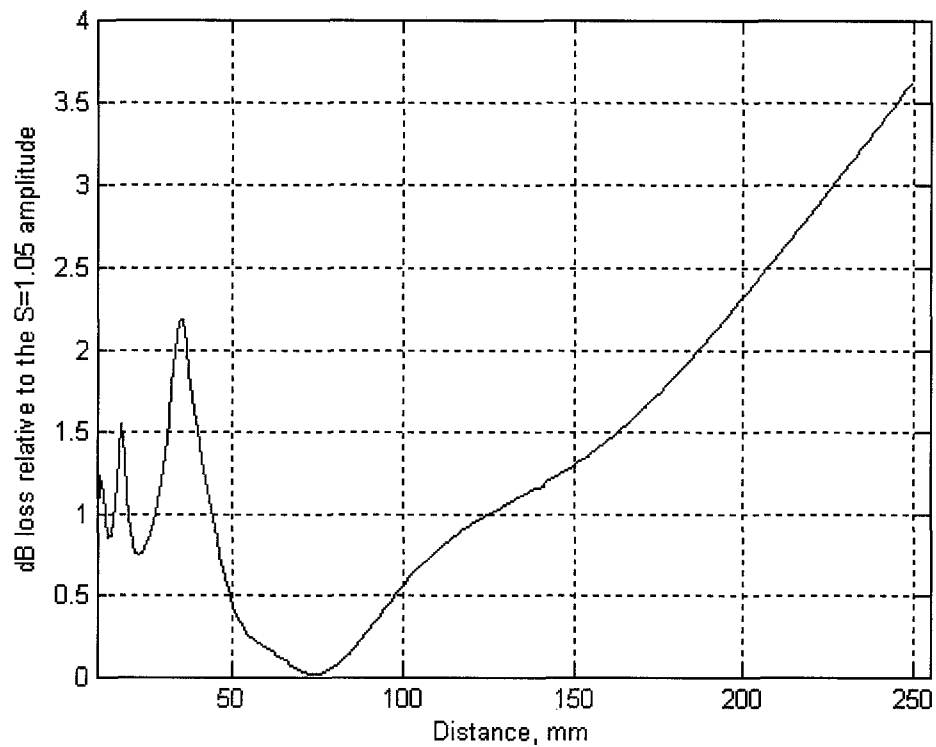
Figure 52. dB loss relative to the S=1.05 amplitude (S = 60 mm). The estimated loss is 1 dB per S starting from 60 mm away from emitter.

86

3. Diffraction Losses in the Ultrasonic Field. Analytic Approach

The axisymmetric solution of the wave equation for longitudinal waves in cylindrical coordinates (r, θ, z) for waves changing in time like $exp(i\omega t)$ takes the form [16]

$$\phi(\alpha r, \beta z) = A(\alpha)J_0(\alpha r)\exp(-i\beta z). \qquad (2)$$

Parameters α, β are called the radial and axial spatial frequencies. Differentiation of (2) by z allows waves in liquid to be expressed as

$$u_z(\alpha r, \beta z) = -i\beta A(\alpha)J_0(\alpha r)\exp(-i\beta z), \qquad (3)$$

where $J_0(x)$ is a Bessel function of the order zero, and

$$\alpha^2 + \beta^2 = k^2 . \qquad (4)$$

The complete spatial solution for $u_z(r,z)$ can be presented in the form

$$u_z(r,z) = -i\beta \int_0^\infty A(\alpha)J_0(\alpha r)\exp(-i\beta z)d\alpha . \qquad (5)$$

The Hankel transform of the function $g(r)$ is defined as

$$G(\alpha) = \int_0^\infty g(r)J_0(\alpha_r)rdr \qquad (6)$$

where

$$g(r) = \int_0^\infty G(\alpha)J_0(\alpha r)\alpha d\alpha \qquad (7)$$

Thus, from (5)-(7) is obtained the expression

$$\frac{-i\beta A(\alpha)}{\alpha} = \int_0^a u_z(r,0)J_0(\alpha r)rdr , \qquad (8)$$

where $A(\alpha)$ is the amplitude of the additive with the radial spatial frequency α, and $u_z(r,0)$ takes only finite values on the interval 0 to a. For the cylindrical piston source the value $u_z(r,0) = u_0$ is an homogeneous function. The integration of (8) taking into account the identity $xJ_1(x) = \int xJ_0(x)dx$ yields

$$-i\beta A(\alpha) = u_0 aJ_1(\alpha a), \qquad (9)$$

where $J_1(x)$ is a Bessel function of the first order. From (5) and (9), it is obtained that at any z-plane

87

$$u_z(r,z) = au_0 \int_0^\infty J_1(\alpha a) J_0(\alpha r) \exp(-i\beta z) d\alpha. \tag{10}$$

This formula allows the calculation of $u_z(r,z)$ for the arbitrary point r, z. The average value of $u_z(r,z)$ can also be found along the radius a, which is proportional to the signal registered by the receiving transducer. This value is often of greater practical application; it can be defined as $\bar{u}_z(z) = 2/a^2 \int_0^a u_z(r,z) r dr$, and in this case, the signal registered by the second receiving transducer will take the form

$$u_z(z) = 2u_0 \int_0^\infty \frac{J_1^2(\alpha a)}{\alpha} \exp(-i\beta z) d\alpha. \tag{11}$$

To check the formula, $z = 0$ can be substituted to obtain $\bar{u}_z(r,0) = u_0$ as it is supposed to be, taking into account the identity $\int_0^\infty \frac{J_1^2(\alpha a)}{\alpha} d\alpha = \frac{1}{2}$.

The Fresnel parameter $S = z\lambda / a^2$ is often used to measure the distance from the emitter. The present analysis will set $a\alpha = Y$ and will use the paraxial approximation

$$\beta = \sqrt{k^2 - \alpha^2} \approx k - \frac{\alpha^2}{2k}. \tag{12}$$

This approximation assumes that only the waves propagating along the axis, or under small angle to axis, contribute to the integral field. The formulas (10) and (11) become

$$\bar{u}_z(r,z) = u_0 \exp(-ikz) \int_0^\infty J_1(Y) J_0\left(\frac{rY}{a}\right) \exp(-iY^2 S / 4\pi) dY. \tag{13}$$

Formulas (10) and (13) yield identical results, and the calculations are shown below. The field pressure distribution shown in Figure 53, and the average field within the radius of 3.0 mm shown in Figure 54, are the same as for the numerical simulation described above using the Raileigh-Sommerfeld integral. In Figure 55, the calculations for the axial pressure are shown. The last maximum hits at exactly the 60-mm value, which is the limit of the near field of the given transducer. Some minor irregularities in the 2D pressure distribution picture and also the axial pressure come from numerical integration errors, which are inevitable especially for infinite limits.

88
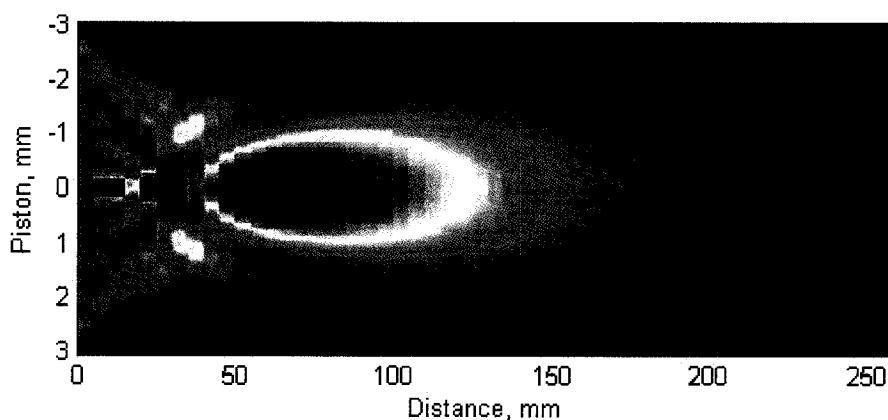
Figure 53. Sound field of the circular piston emitting in water; radius – 3.0 mm, at 10 MHz. Analytical model.
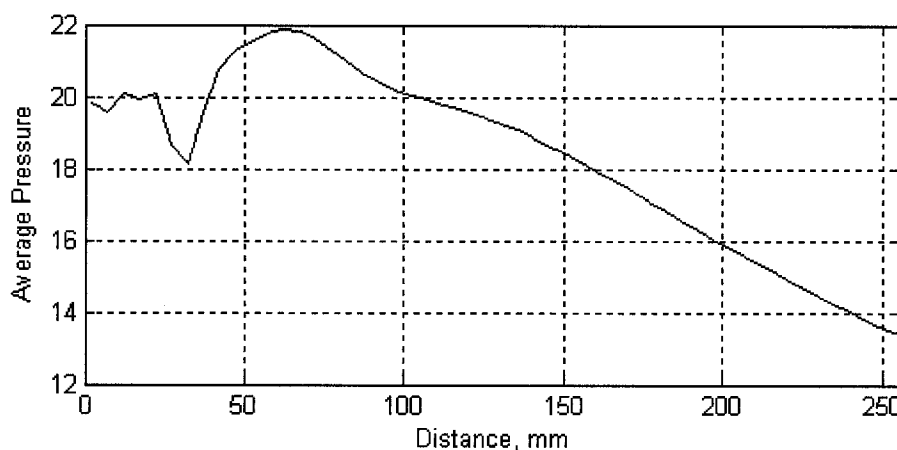
Figure 54. Average pressure at the receiving transducer of the same 3.0 mm radius as the emitter.
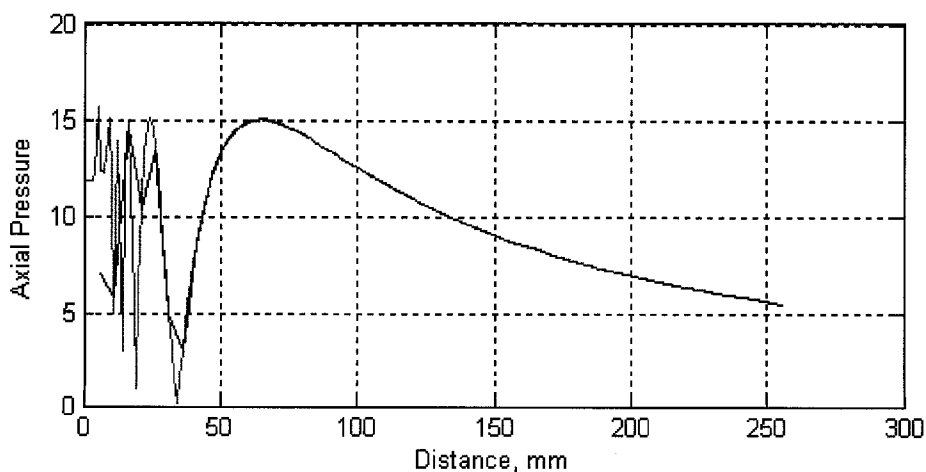
Figure 55. Axial pressure of the sound field; blue – analytic, red – numeric model. Some differences come from the use of paraxial approximation.

The average value of particle displacement along z-direction within the limits of the receiving transducer of radius a is

89

$$\overline{u}_z(r,z) = 2u_0 \exp(-ikz) \int_0^{\infty} \frac{J_1^2(Y)}{Y} \exp(-iY^2 S / 4\pi)dY \ . \qquad (14)$$

This formula (if divided by u_0) can be used to estimate the diffraction losses of the acoustic pressure with respect to $z = 0$ value.

The computer calculations of the far field for the circular emitting and receiving transducers were made using (14). The dB loss is calculated for the field received by the ultrasonic transducer in water, analogous to the numerical calculations performed above.

The calculations were performed for the same settings used in the numerical calculations. The integrals were evaluated on a PC with quadrature integration using MATLAB (The Math Works Inc.) The results are presented for distances below the Fresnel zone – that is for the far field. Estimation of the average dB loss per distance a^2 / λ, which is in the present case equals to 60 mm, yields the results very close to those calculated in the numerical model and presented in the literature. The value is ~1dB per a^2 / λ, which confirms the validity of the numerical calculations.

This loss needs to be added to the loss estimation due to other mechanisms, including attenuation in the material and losses at interfaces.
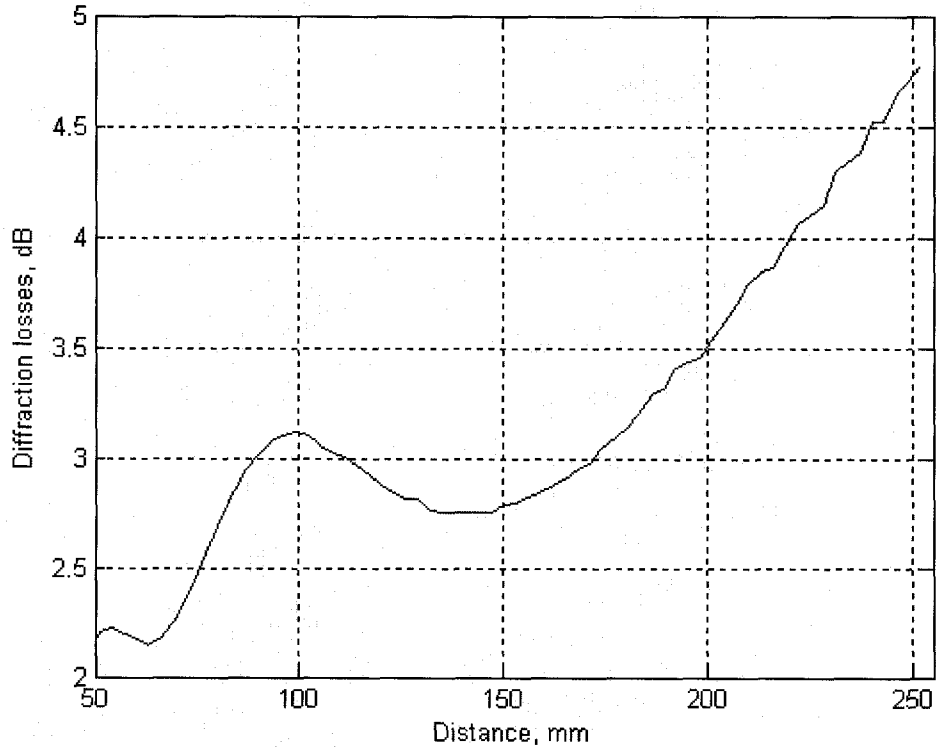
Figure 56. The dB loss at the receiver, $a^2 / \lambda = 60$ mm. Analytical model.

3. Conclusions

Overall, the analytic and numerical solutions yield almost identical results and support each other in that sense. Both methods carry some error, each of a different nature. In direct numerical simulations, quantization of the integration introduces errors in the final results. Reducing the step size or the elementary surface area of the transducer increases the precision, and in principle can yield any required level of precision. Still, in many practical applications, the mesh sizes used in this model are more than satisfactory to develop a correct understanding of the problem. Field calculations performed for the analytic solutions still involve numerical integration. In this case, though, there was no need to break up the emitter surface into small elements because it was accomplished in numerical model. Also, the analytical solution does not require direct numeric integration of the field over the area of the receiving transducer.

References

1. E. P. Papadakis, *Ultrasonic attenuation and velocity in three transformation products in steel*, J. Appl. Phys., vol. 35, pp. 1474-1482, 1964.
2. C. R. Hill, Ed., *Physical Principles of Medical Ultrasonics*. New York: John Wiley, 1986, pp. 176-194.
3. K. A. Wear, *The Effects of frequency-dependent attenuation and dispersion on sound speed measurements: Applications in human tabecular bone*. IEEE Trans. Ultrason,, Ferroelect., Freq. Contr., vol. 47, no. 1, pp. 265-273, 2000.
4. Guillaume Haiat et al, *Effects of frequency-dependent attenuation and velocity dispersion on in vitro ultrasound velocity measurements in intact human femur specimens*. IEEE Trans. Ultrason,, Ferroelect., Freq. Contr., vol. 53, no. 1, pp. 39-51, 2006.
5. Jonathan J. Kaufman, Wei Xu, Alessandro E. Chiabrera, and Robert S. Siffert, *Diffraction Effects in Insertion Mode Estimation of Ultrasonic Group Velocity*. IEEE Transactions on UFFC, Vol. 42, No. 2, March 1995, pp. 232-242.
6. H. Seki, A. Granato, and R. Truell, "Diffraction effects in the ultrasonic field of piston source and their importance in the accurate measurement of attenuation," J. Acoust. Soc. Am., vol. 28, No. 2, pp. 230-238, Mar. 1956.
7. I. Cespedes and J. Ophir, "Diffraction correction methods for pulse-echo acoustic attenuation estimation," Ultrasound in Med. Biol., vol. 16, no. 7, pp. 707-717. 1990.
8. M. O'Donnell, "Effects of diffraction on measurements of the frequency dependent ultrasonic attenuation," IEEE Trans. on Biomedical Eng., vol. BME-30, no. 6, pp. 320-326, June 1983.
9. E. P. Papadakis, "Correction for diffraction losses in the ultrasonic field of a piston source," J. Acoust. Soc. Am., vol. 31, no. 2, pp. 150-152, Feb. 1959.
10. R. Kuc, "Diffraction effects in reflected ultrasound spectral estimates," IEEE Trans. Biomedical Eng., vol. BME-31, no. 8, pp. 537-545, Aug. 1984.
11. R. Bass, "Diffraction effects in the ultrasonic field of a piston source," J. Acoust. Soc. Am., vol. 30, no. 7, pp. 602-695, July 1958.
12. R. A. Mountford and M. Halliwell, "Physical sources of registration errors in pulse-echo ultrasonic systems-Part 11: Beam deformation, deviation and divergence," Medical and Biological Eng., pp. 33-38, Jan. 1973.
13. M. Fink and J. Cardoso, "Diffraction effects in pulse-echo measurement," IEEE Trans. Son. and Ultrason., vol. SU-31, no. 4, pp. 313-329, July 1984.
14. R. C. Chivers and C. R. Hill, "Ultrasonic attenuation tomography of soft tissue," Ultrason. Imag., vol. 1, pp. 1633, 1979.
15. A. O. Williams, Jr., *The piston source at high frequencies*. J. Acoust. Soc. Am., vol. 23, no. 1, pp. 1-6, Jan. 1951.
16. G. K. Kino, Acoustic Waves: Devices, Imaging, and Analog Signal Processing. Englewood Cliffs, NJ: Prentice-Hall, 1987.

CHAPTER VI

Study of Diffraction Effects on the Estimation of Ultrasonic Group Velocity and Time of Flight

1. Introduction

Ultrasonic transducer beam divergence and diffraction affect the emitted pulse in different ways. The main two are: the excessive dB loss of the signal on the top of the attenuation in the medium; and the effective increase of the phase and group velocity compared to the plane wave [1, 2]. The first effect was considered in the previous section. This section will deal with the velocity, hence time of flight, measurements and the way they are affected by the beam diffraction.

Several papers have reported on diffraction effects in ultrasonic velocity estimation [3-6]. Mostly, these deal with phase velocity corrections, which are useful in, for example, elastic modulus measurements. For ultrasonic nondestructive characterization using the pulse-echo technique, the precise group velocity measurement is often of interest [1].

Diffraction effects can usually be neglected in insertion methods when the respective velocities of ultrasound in the unknown and reference media are approximately equal. For example, when insertion measurements are carried out to identify the velocity of ultrasound in biological soft tissue, and the reference medium is water, diffraction effects are so small as to be essentially insignificant [1, 2]. However, if the two media have velocities that differ by more than 50%, then diffraction can contribute up to 1% errors in the velocity estimates. This is valid in the present case when the difference in longitudinal wave velocity between water and steel is more than four times, 1450 m/s and 5900 m/s respectively.

In order to reduce the error in time of flight measurements, the influence of diffraction on the estimation of the differential phase spectrum (ultrasonic group velocity) needs to be estimated. If the estimated error exceeds the requirements of the NDT method for the spot weld characterization, corrections in the signal processing routine may need to be implemented.

93

2. Analytic Description

For description simplicity the following setup was chosen. A circular piston emitter immersed in water emits sound. The wave travels through the water, and enters a steel plate that is oriented perpendicular to the transducer axis and to the direction of sound propagation. The wave penetrates the steel plate, reflects off its back wall and returns to the emitting transducer following the same path in the inverted order.

Let $v(t)$ denote the input electrical signal to the piezoelectric crystal. The spectrum of the received waveform after it has propagated through the water-steel-water complex is given by $Y_e(f,z)$:

$$Y_e(f,z) = H_W^1(f)H_S(f)H_W^2(f)H_D^e(f,z)H_T(f)H_R(f)V(f) \qquad (1)$$

Here, f is the frequency and z is the distance between the emitting transducer and the back wall of the metal plate. $V(f)$ is the Fourier transform of the input signal, $v(t)$. $H_T(f)$, and $H_R(f)$ are the transfer functions of the transmitting and receiving transducer loaded with water. In the given case, the transmitting and receiving transducer are the same; but in general there can be two separate ones. $H_W^1(f), H_W^2(f)$ and $H_S(f)$ are the acoustic transfer functions of an incident planar wave in the water path between the transmitting transducer and sample, in the water path between the sample and receiving transducer (on the way back), and in the sample itself, respectively. All diffraction effects are incorporated in $H_D^e(f,z)$, which characterizes the effect of diffraction on the ultrasound pulse for the water-steel-water propagation path, and which is a function of the transducer separation distance, z, transducer radius, a, and also the acoustic properties of the water and specimen.

Similarly, $Y_r(f,z)$ is the Fourier transform of the ultrasound signal that has propagated through the water path only, i.e., without the sample present, and is given by

$$Y_r(f,z) = H_W^1(f)H_W^S(f)H_W^2(f)H_D^r(f,z)H_T(f)H_R(f)V(f) \qquad (2)$$

Here, $H_D^r(f,z)$ characterizes the effect of diffraction on the received acoustic waveform for the water path only. $H_W^S(f)$ is the acoustic transfer function of an incident planar wave in the water, which is displaced by insertion of the steel plate into the reference medium. In these formulae, any acoustic transmission and reflection coefficients were neglected. It is possible to omit them because these coefficients are

94

frequency-independent and will not affect the analysis. In practice, the acoustic transmission and reflection coefficients provide constant gain factors, which will not affect the phase estimates used in the group velocity estimation procedure. This is essentially the same strategy that was accepted when the frequency-dependent attenuation was considered: the interfaces only reduce the overall signal amplitude regardless of the frequency content of the signal (all frequency components are reduced by the same factor). Also, possible multiple reflections have been neglected assuming that proper time gating can effectively isolate the primary incident acoustic waveform.

An estimate, $\hat{H}_S(f,z)$, of the sample's acoustic transfer function, $H_S(f)$, is obtained by dividing (1) by (2) and multiplying the result by $H_W^S(f)$:

$$\hat{H}_S(f,z) = \frac{Y_e(f,z)}{Y_r(f,z)} H_W^S(f) = H_S(t) \frac{H_d^e(f,z)}{H_d^r(f,z)} . \tag{3}$$

In this formula it is assumed that $H_W^S(f)$ is known and is equal to $\exp(-i2\pi f d / v_W)$ where v_W is the ultrasonic velocity in the water reference media, and d is the sample thickness. The estimated sample transfer function is seen to be modified by the effect of diffraction. This can be characterized by the diffraction transfer function, $H_D(f,z)$, defined by

$$H_D(f,z) \equiv \frac{H_d^e(f,z)}{H_d^r(f,z)} \tag{4}$$

and thus

$$\hat{H}_S(f,z) = H_S(f)H_d(f,z). \tag{5}$$

Let the transfer function of the sample be written as

$$H_S(f) = A_S(f)\exp(-i\varphi_S(f)) \tag{6}$$

where $\varphi_S(f)$ is the phase of the specimen's acoustic transfer function measured in radians, and $A_S(f)$ is its magnitude. The phase function can be expressed in terms of the specific phase function, $\beta_S(f)$, as

$$\varphi_S(f) = \beta_S(f)d \tag{7}$$

where d is the sample thickness. The group velocity is defined as

$$v_g(f) \equiv 2\pi \left(\frac{d\beta_S(f)}{df} \right)^{-1} \tag{8}$$

95

Neglecting the effect of diffraction, the group velocity estimate, $\hat{v}_g(f,z)$, can be evaluated as

$$\hat{v}_g(f,z) = -2\pi d \left[\frac{d}{df} \arg\left(\frac{Y_e(f,z)}{Y_r(f,z)} H_W^S(f) \right) \right]^{-1}. \tag{9}$$

In this formula it is assumed that the *arg* function produces a continuous function of frequency f, or that the phase is appropriately unwrapped. As may be seen, the estimate of the group velocity, $\hat{v}_g(f,z)$, is a function of the distance z at which the insertion measurement is made. The actual value of the group velocity, $v_g(f,z)$, is given by

$$v_g(f,z) = -2\pi d \left[\frac{d}{df} \arg\left(\frac{Y_e(f,z)}{Y_r(f,z)} \frac{H_W^S(f)}{H_d(f,z)} \right) \right]^{-1}. \tag{10}$$

The error associated with using (9) instead of (10), $\hat{v}_g(f,z) - v_g(f,z)$, is due to the diffraction of ultrasound wave. Neglecting this effect can result in errors in the group velocity estimate.

3. Group Velocity Diffraction Correction

3.1. Basic Diffraction Theory

The acoustic waves emitted by a transducer into a specimen are not confined to a region contained within the geometrical shadow of the transducer, and are not perpendicular to its emitting surface. Because of the transducer's finite size, the ultrasonic wave spreads out into a diffraction field, a phenomenon that can introduce errors in both attenuation and velocity measurements. The diffraction effect is related to the ratio of the source size to the acoustic wavelength and thus is especially important for low frequencies and small transducer faces. A similar diffraction phenomenon occurs for the acoustic wave impinging on the receiver. In general, there is a further contribution to diffraction due to the mismatch between the sample and the reference media, and due to the sample's finite size and possible surface irregularities.

A number of investigations have been performed on the effect of diffraction on attenuation and velocity measurements (both group and phase). Usually, the transducer is

96

treated as a finite piston source radiating into a semi-infinite medium. The acoustic field is found at each point of the propagation medium and integration is performed over a specified area, usually concentrically located with respect to the source transducer.

Assume, a transducer of radius a on the $z = 0$ plane. The velocity potential $\Phi(x,y,z)$ can be expressed as

$$\Phi(x,y,z) = -\frac{1}{2\pi} \int_S u_z(x',y',0) \frac{\exp(-ikR)}{R} dS' \tag{11}$$

where R is the distance between the source point and the field point *(x, y, z)*; *u* is the displacement of the transducer surface in the normal direction at $x=x'$, $y=y'$, $z = 0$; and S' is the differential element of the transducer surface S. Using the Hankel transform, an expression for the acoustic displacement $\mu_z(r,z)$ in cylindrical coordinates *(r, θ, z)* can be found and expressed in terms of the parameters k_r and k_z, the radial and axial spatial frequencies respectively:

$$\mu_z(r,z) = a\mu_0 \int_0^\infty J_1(k_r,a)J_0(k_r,r)\exp(-ik_z z)dk_r \tag{12}$$

and

$$k_r^2 + k_z^2 = k^2. \tag{13}$$

Here, J_0, J_1 are the zeroth and first order Bessel functions respectively, $k = 2\pi/\lambda$ is the wave number, and λ is the wavelength of the wave. The response of a receiving transducer of radius a located a distance z from the transmitting transducer is proportional to the average displacement over its surface, $\bar{\mu}_z(z)$, where

$$\bar{\mu}_z(z) = \frac{2}{a^2} \int_0^a \mu_z(r,z)rdr. \tag{14}$$

Using (12) and the Fresnel approximation,

$$k_z = \sqrt{k^2 - k_r^2} \cong k - \frac{k_r^2}{2k} \tag{15}$$

the average displacement $\bar{\mu}_z(z)$ at a distance z (at the receiver) is given by

$$\mu_z(r,z) = 2\mu_0 \exp(-ikz) \int_0^\infty \frac{J_1^2(Y)}{Y} \exp(iY^2 S/4\pi)dY. \tag{16}$$

Here $S = z\lambda/a^2$ is the Fresnel parameter and μ_0 is the displacement at $z = 0$. This formula includes the plane wave propagation term $\exp(-ikz)$. Because this term has already been

97

incorporated in (1) and (2) through the complex transfer functions $H_W^1(f), H_W^2(f), H_W^S(f)$, and $H_S(f)$, the modified average displacement function, $\bar{\mu}_z^*(z)$, can be defined as

$$\mu_z^*(r,z) = 2\mu_0 \int_0^\infty \frac{J_1^2(Y)}{Y} \exp(iY^2 S/4\pi)dY .$$ (17)

This formula will be used below to derive the diffraction correction technique.

3.2. Diffraction Correction

In order to introduce corrections to the velocity measurements, the group velocity diffraction correction technique can be used. This technique numerically evaluates $H_d(f,z)$ and uses it to adjust the measurements. Once $H_d(f,z)$ is known, it may be used in (10) to obtain the diffraction corrected group velocity.

In order to evaluate $H_d(f,z)$, (17) is used with appropriate parameter values. Specifically, values for the Fresnel parameter, S, must be determined. Two cases must be considered. The first case deals with the values associated with the water-sample-water complex, and the second with the values associated with the water path only. In the following analysis, it is assumed that the Fresnel approximation (15) holds. Accordingly, the use of this approximation makes it straightforward to evaluate the result when an ultrasonic wave propagates through layered media. The total value of S is found by adding the values of S determined for each region, using the appropriate values of z and λ in these regions (p.175 in [7]). This analysis assumes also that the frequency dependence can be ignored for the transmission and reflection coefficients associated with each of the layered media. Also, the incidence is primarily normal, and mode conversion does not occur. The latter two assumptions are closely related to the use of the Fresnel approximation itself (p. 173 in [7]).

In view of the above assumptions, the value for S in the case of the water-sample-water path, namely $S = S_e$, may be obtained by adding together the individual contributions from each layer of the propagation medium, using the appropriate values of z and λ in these regions.

98

$$S_e = S_{W1} + S_S + S_{W2} \qquad (18)$$

Here, $S_{W1} = z_{W1}\lambda_W / a^2$ and is the Fresnel parameter for the water layer between the transmitter and sample; $S_S = d\lambda_S / a^2$ is the Fresnel parameter for the sample layer; $S_{W2} = z_{W2}\lambda_W / a^2$ and is the Fresnel parameter for the water layer between the sample and the receiver, which in the reflection mode will be identical to the transmitter-water region. z_{W1}, d, z_{W2} are the thickness of the water layer between emitter and the sample, the thickness of the sample, and, the thickness between the sample and the receiver, respectively. λ_W, λ_S are the wavelengths of ultrasound in water and sample, respectively.

A similar evaluation can be used to determine the value of S for the water only path, $S = S_e$. In this case, $S_r = z\lambda_W / a^2$. These parameters can then be used to evaluate $H_d^e(f, z)$.

The diffraction effect for the water-sample-water path which was characterized earlier by $H_d^e(f, z)$ in (1) can now by analytically described by

$$H_d^e(f, z) = \frac{\overline{\mu}_{ze}^*(z)}{\mu_0} = 2\int_0^\infty \frac{J_1^2(Y)}{Y}\exp(iY^2 S_e / 4\pi)dY \qquad (19)$$

where $\overline{\mu}_{ze}^*(z)$ is the modified average displacement function on a concentric receiver of radius a located at a distance z from the source for water-sample-water complex. Similarly, the diffraction effect for the water path only, $H_d^r(f, z)$ (2), can be described by

$$H_d^r(f, z) = \frac{\overline{\mu}_{zr}^*(z)}{\mu_0} = 2\int_0^\infty \frac{J_1^2(Y)}{Y}\exp(iY^2 S_r / 4\pi)dY \qquad (20)$$

where $\overline{\mu}_{zr}^*(z)$ is the modified average displacement function on a concentric receiver of radius a located at a distance z from the source for the water path only. The diffraction transfer function (4) can then be derived using

$$H_d(f, z) = \frac{\left(\dfrac{\overline{\mu}_{ze}^*(z)}{\mu_0}\right)}{\left(\dfrac{\overline{\mu}_{zr}^*(z)}{\mu_0}\right)}. \qquad (21)$$

Substitution of (19) and (20) into (21) yields

99

$$H_d(f,z) = \frac{\int_0^\infty \frac{J_1^2(Y)}{Y} \exp(iY^2 S_e / 4\pi)dY}{\int_0^\infty \frac{J_1^2(Y)}{Y} \exp(iY^2 S_r / 4\pi)dY} \tag{22}$$

$H_d(f,z)$ can be closely approximated using standard numerical integration procedures.

3.3. Calculation Results

The calculation of the phase of the transfer function $H_d(f,z)$ was performed in the frequency range 7.5 to 15 MHz to cover the working frequency of the 10 MHz transducer. The distance ranged from 35 mm to 350 mm. Again, the transducer used was the 3.0-mm radius circular piston emitting in water (sound speed 1493 m/s). The sample was modelled to be a steel plate, 3.0-mm thick with longitudinal speed of sound equal to 5900 m/s. The integrals in (22) were evaluated by a quadrature integration method using MATLAB. Figure 57 shows the simulation results. The plot shows that the largest diffraction effect is localized to lower frequency values and shorter distances.
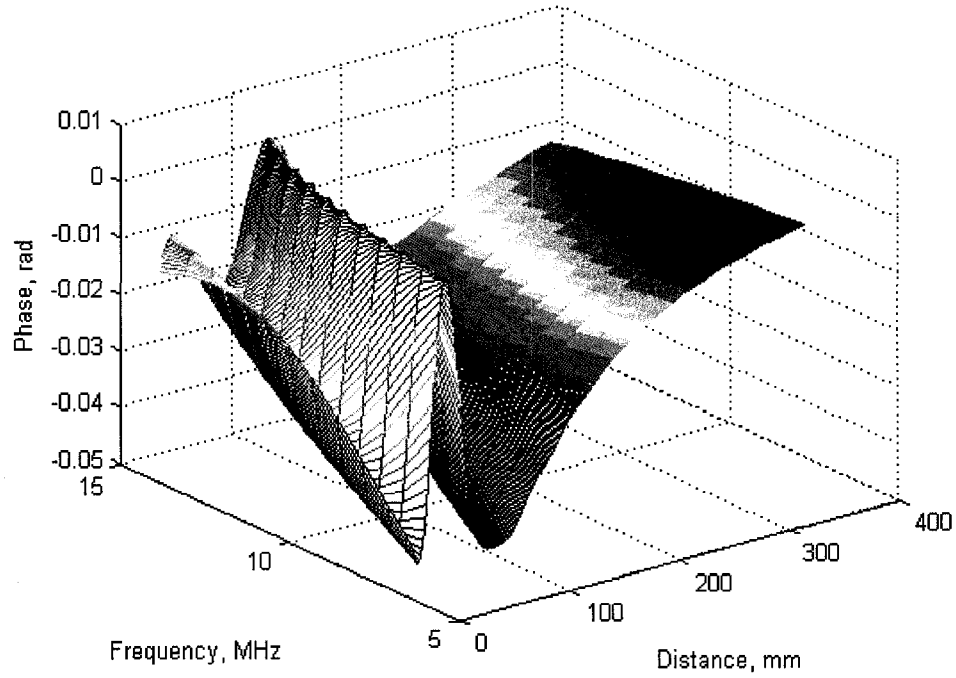
Figure 57. The phase of the diffraction transfer function, $H_d(f, z)$, for the frequency range 5-15 MHz and distance 35 to 350 mm, with transducer radius 3.0 mm and sample thickness 3.0 mm.

Now, the effect of $H_d(f, z)$ on the ultrasonic group velocity estimate can be calculated. In this simulation, the phase of the sample acoustic transfer function $H_S(f, z)$ was modelled as

$$\phi_S(f) = \frac{2\pi f d}{v_S} \tag{23}$$

where v_S is the velocity of ultrasound in the sample. $H_S(f, z)$ was then multiplied by $H_d(f, z)$ as in (5), to obtain the diffraction corrupted acoustic transfer function, $\widehat{H}_S(f, z)$, of the sample. Then, a linear least squares curve fit of the unwrapped phase of $\widehat{H}_S(f, z)$ was performed over the frequency range covering the 10 MHz; then the ultrasonic group velocity, $\widehat{v}_g(f, z)$ was evaluated, as in (9), as a function of distance z. The time of flight calculation is contained within this procedure is obtained from

$$t = \frac{1}{2\pi} \frac{d\varphi}{df}. \tag{24}$$

The frequency range is always chosen to include the central frequency of the signal spreading equally on both sides of it. For the broadband transducer a working bandwidth

101

of about 5 MHz is usually used, thus requiring a frequency range from 7.5 MHz to 12.5 MHz.

This same procedure estimates the time of flight error as these two values have the same nature. The results of this simulation are shown in the following pictures [8]. Figure 58 presents the variability in group velocity determination in steel as a function of distance from the emitting transducer. Because of diffraction effects, the group velocity will deviate from the plane wave velocity in the material. In Figure 59, the relative error for the velocity evaluation is shown. The reference value was taken to be 5900 m/s for steel. Precise measurements can suffer an uncertainty in velocity values of up to 0.5% if corrections are not applied. Figure 60 presents the time of flight deviation when the receiving transducer is at some specific distance from the emitter. For 3.0-mm steel plate in the water, the TOF error can be up to 2.5 ns due to diffraction of the ultrasonic beam.

It can be seen from all of these figures that most of the errors due to diffraction come from the area within two a^2 / λ, which is 60 mm in the present case. Still, many applications, including spot weld characterization, work within this range. Diffraction of the beam adds further error to the measurements of time of flight and consequently to the group velocity. The error in the group velocity measurement can reach 0.5%. Depending on the application, the error can be considered negligible or critical. In the current case, taking into account the diffraction correction for time of flight measurements can improve the accuracy by 2-3%.
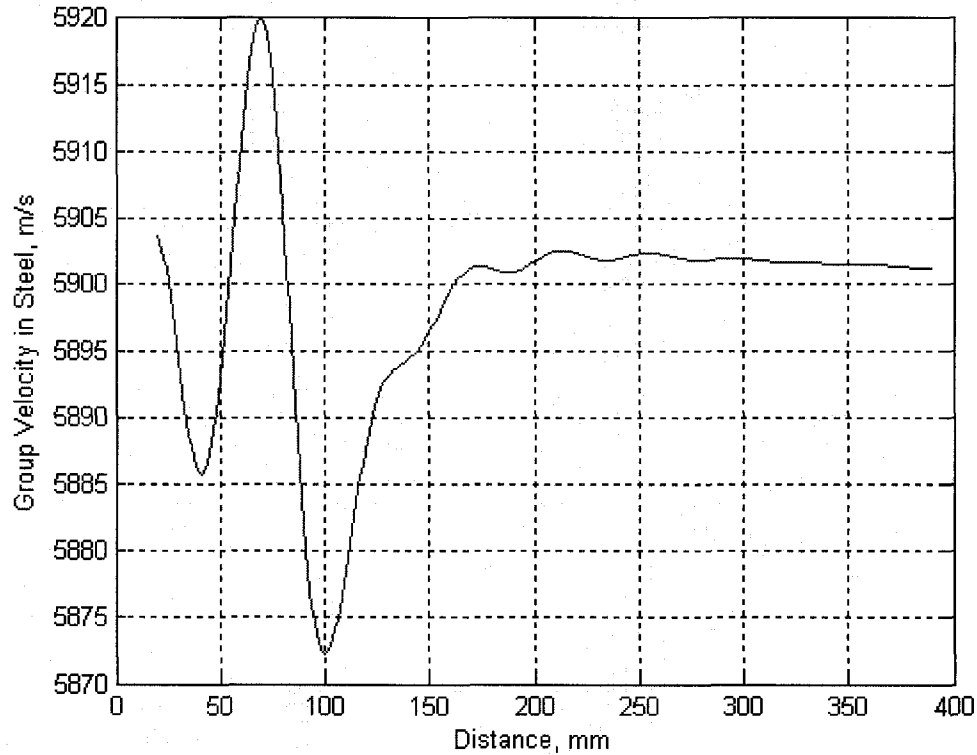
Figure 58. Variation of the group velocity due to diffraction as a function of distance from the emitter.

To measure the difference arising from the use of different sample materials, the same calculations were performed for the sample imitating biological tissue in the sense of sound velocity. As most tissues are comprised of up to 95-98% water, acoustic properties of soft biological tissues are often very close to that of the water. Particularly, the sound speed differs from that of water by 5-7%. Calculations were performed for a flat sample having a speed of sound of 1600 m/s; the steel sample used 5900 m/s. Results have shown that when the speeds in the reference medium (water) and the sample are close, the effects of diffraction become negligible for virtually any application.

103
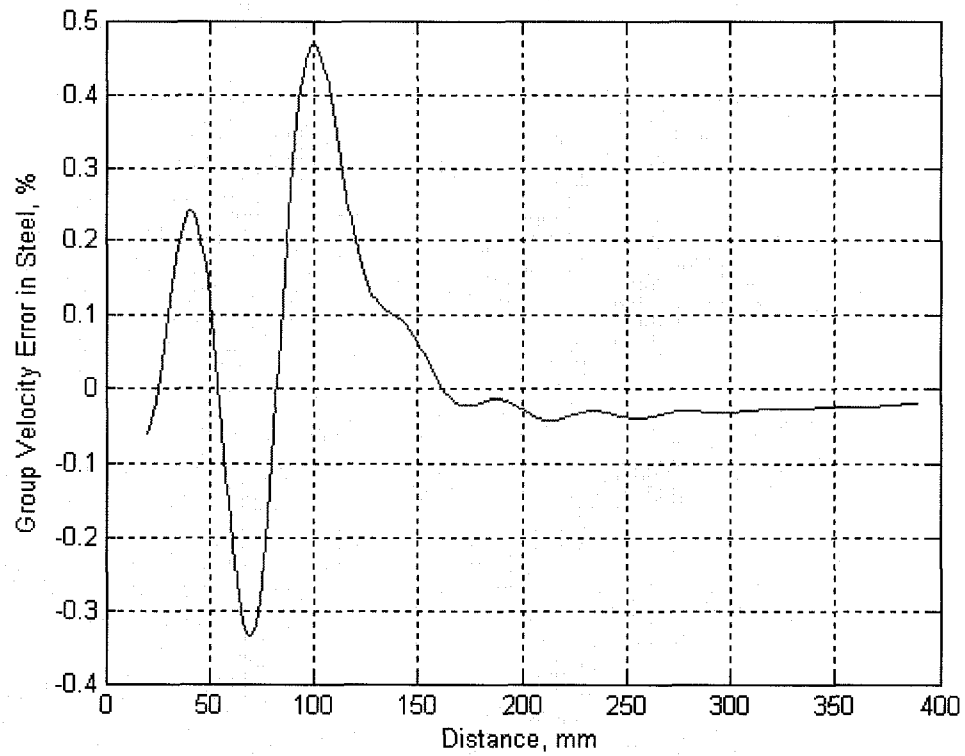
Figure 59. Error in group velocity measurement compared to the plane wave velocity of 5900 m/s.

Figure 60. Variation in time of flight measurement due to diffraction as a function of distance from the emitter.

104

Figure 61. Variation of the group velocity due to diffraction as a function of distance from the emitter. Imaginary biological tissue with sound speed of 1600 m/s (close to water).
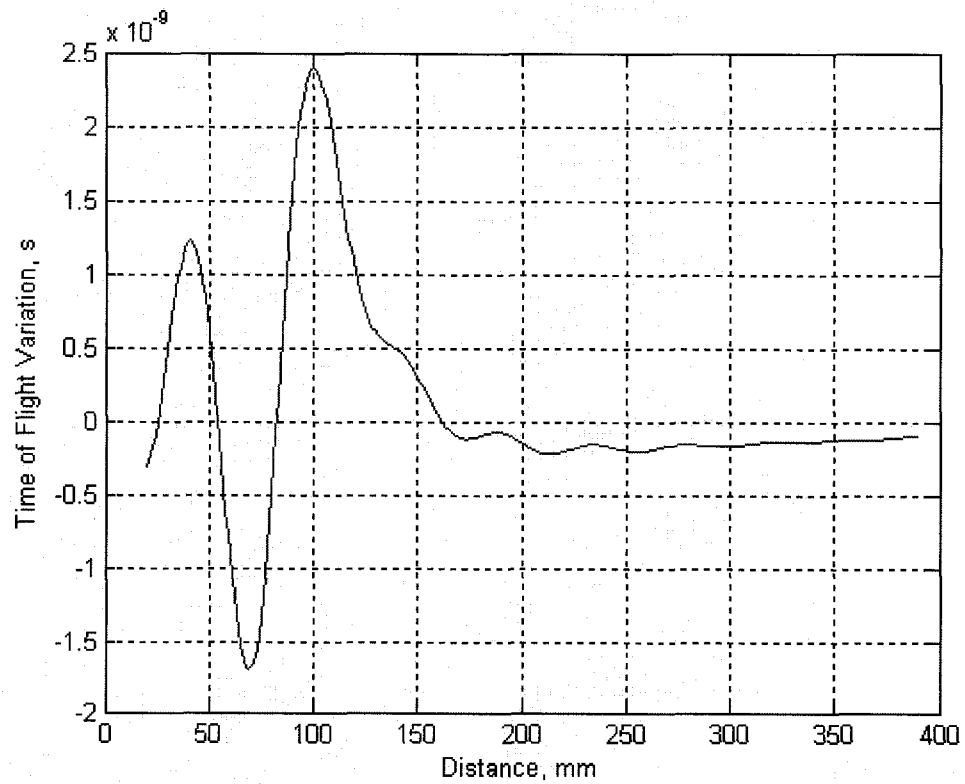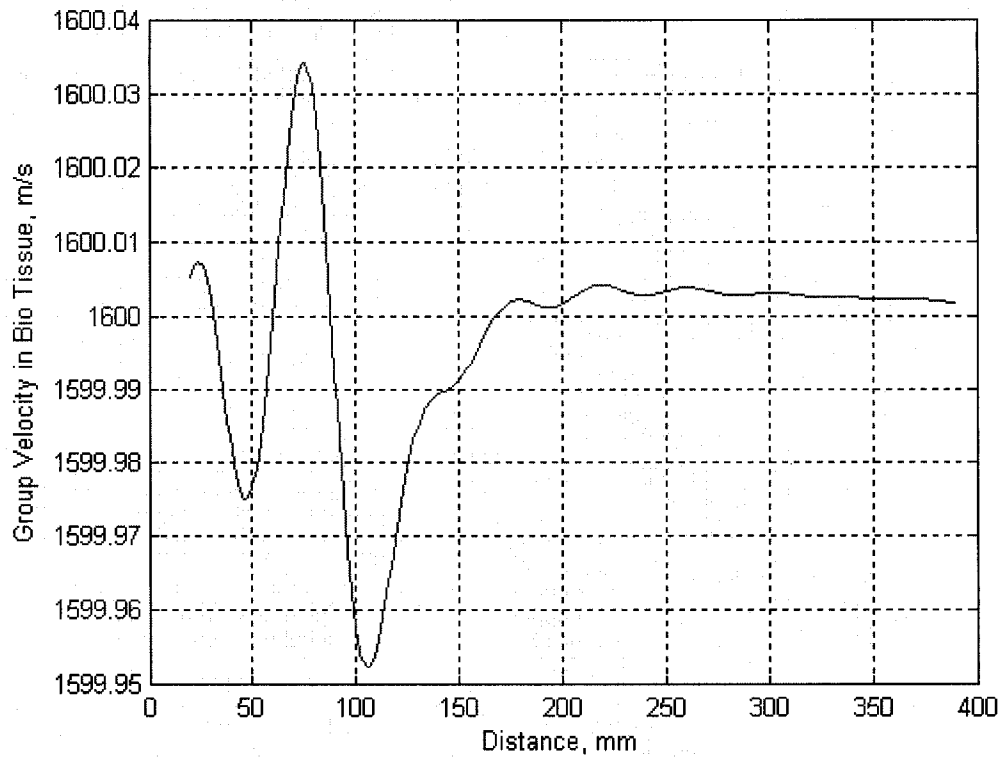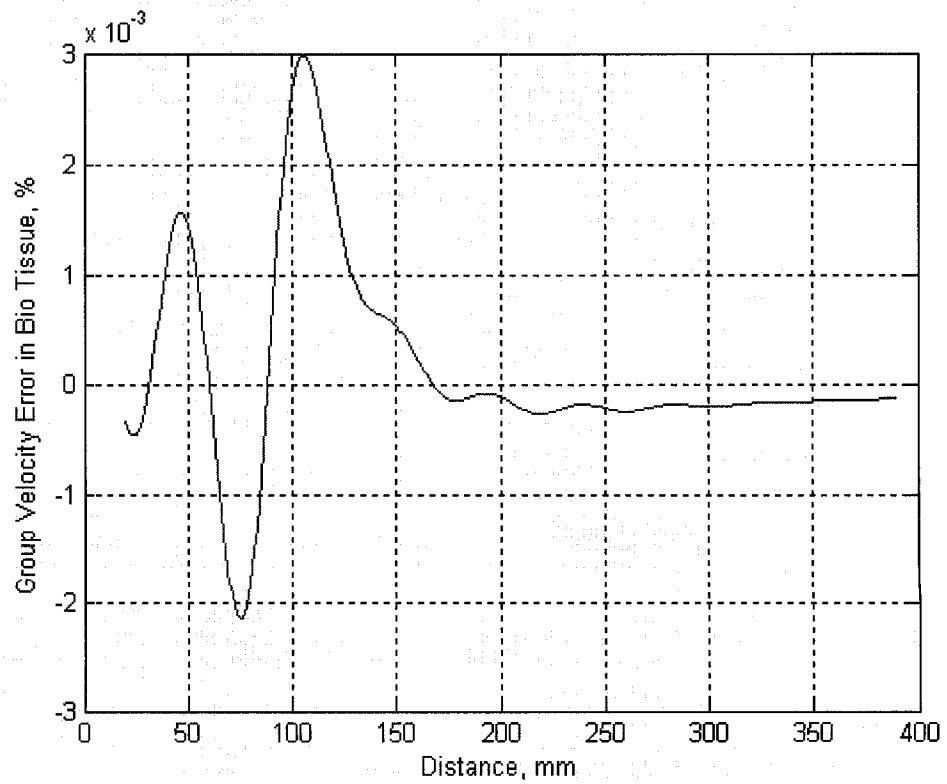

Figure 62. Error in group velocity measurement compared to the biological tissue velocity of 1600 m/s.

105

4. Conclusions

This chapter described the diffraction effects arising from the use of a sound source of finite size. Beam diffraction was noted to affect both the attenuation of the wave and the time of flight measurements, as well as the group velocity if it is needed to characterize the material properties. It was shown that the error in time of flight measurements is relatively small. Still, in the described field of application for resistance spot weld evaluation, including this correction will benefit the method.

Simulations have shown that the relative diffraction error depends on the difference between the velocities in the reference and sample media. For materials such as biological tissues measured in water, the diffraction errors would be almost nonexistent. For materials with much greater sound velocities than in water, however the diffraction effect might be important when the measurement is carried out in water. Diffraction correction can improve the accuracy of the velocity and time of flight measurements. Since it has been shown that the maximum error for the medium combination of water-steel is no more than 0.5%, a first estimate of the velocity can be obtained by direct measurement without any diffraction correction procedure. Once this initial estimate of the velocity is obtained, it can be corrected using the calculated results to increase the accuracy of the empirical estimate.

Also, it is useful to note, that diffraction correction is not necessary when measurements can be made with transducers separated by sufficiently large distances. The abovementioned analysis can be used to determine the minimum distance necessary to avoid diffraction effects, or at least minimize them. The calculations show that at a distance of up to 160 mm, about $2.5S$, the variations due to diffraction are largest. Beyond that limit, the deflections reduce significantly; even for the high velocity mismatch case of steel-water, the group velocity error will not exceed 0.05%. Still, for this particular situation with a working distance range of some 50-60 mm the diffraction correction can be a relevant issue for consideration.

The diffraction correction technique developed does not require the emitting and receiving transducers to have the same face diameter. The method will readily work for a different transmitter and receiver, if needed, simply by changing the integration limits in (14) and recomputing the diffraction transfer function. Also, coaxial misalignment is not a

106

problem for the method, and if required can also be applied to solve for a particular geometric configuration.

Diffraction effects, besides other disturbances caused by frequency-dependent attenuation and noise, can cause small additional errors in time of flight and velocity measurements. The described technique can be used to apply corrections relatively easily during measurements in different insertion mode experiments.

References

1. C. R. Hill, Ed., *Physical Principles of Medical Ultrasonics*. New York: John Wiley, 1986, pp. 176-194.
2. Jonathan J. Kaufman, Wei Xu, Alessandro E. Chiabrera, and Robert S. Siffert, *Diffraction Effects in Insertion Mode Estimation of Ultrasonic Group Velocity*. IEEE transactions of UFFC, Vol. 42, No. 2, March 1995, pp. 232-242.
3. H. J. McSkimin, *Empirical study of the effect of diffraction on velocity of propagation of high-frequency ultrasonic waves*. J. Acoust. Soc. Am.vol. 32, no. 11, pp. 1401-1404, Nov. 1960
4. W. A. Verhoef, M. J. Cloostermans and J. M. Thijssen, *Diffraction and dispersion effects on the estimation of ultrasound attenuation and velocity in biological tissues*. IEEE Trans. Biomed. Eng., vol. BME-32.
5. E. P. Papadakis, *Ultrasonic phase velocity by the pulse-echo-overlap method incorporating diffraction phase correction*. J. Acoust. Soc. Am.
6. E. P. Papadakis, *Ultrasonic diffraction loss and phase change for broad-band pulses*. J. Acoust. Soc. Am., vol. 52, pp. 847-849, Jan. 1972.
7. G. K. Kino, Acoustic Waves: Devices, Imaging, and Analog Signal Processing. Englewood Cliffs, NJ: Prentice-Hall, 1987, pp. 158-175.
8. **A. M. Chertov**, R. Gr. Maev, *Investigation of the Effects of Frequency-Dependent Attenuation and Diffraction in the Liquid Nugget of a Spot Weld on the Ultrasonic Signal*. To be submitted to IEEE UFFC.
9. W. Xu and J. J. Kaufman, "Diffraction correction methods for insertion ultrasound attenuation estimation," IEEE Trans. Biomedical Eng., vol. 40, no. 6, pp. 563-570, July 1993.

107

CHAPTER VII

Development of the Spot Weld Quality Characterization Algorithm Based on the B-Scan Analysis

1. Automatic Resistance Spot Weld Quality Characterization

Using a set of weld parameters provided by the ultrasonic B-scan, it is possible to qualify the weld nondestructively. This is the primary goal of the method – to characterize the weld non-destructively and to use this information for quality assurance on the assembly line. All of the features of a weld pattern are easily recognized by the human. It would take little effort even for a novice to localize the copper-steel and solid-liquid interfaces, the moment of central interface disappearance, and of current shutdown. Still, this task is not trivial for a machine. Teaching the computer to recognize the pattern of interest on often noisy B-scans has required a considerable amount of work. The main idea is make the machine extract separate features of the pattern based on some a priori knowledge of the approximate locations of different interfaces. Afterwards, the machine assembles them into a pattern and characterizes the weld.

At different stages during the pattern recognition procedure, the software applies 1D and 2D filters to extract features from the B-scan. As long as this recognition is a probabilistic process, there remains a chance that the software will not recognize the pattern element. Thus, the higher the signal-to-noise ratio on the B-scan, the higher the detection probability. Figure 63 shows three scans with corresponding detected patterns.

In most of the cases, the pattern of interest can be divided into a set of straight line segments. The detection of segments instead of the full pattern at once is preferable as long as the majority of the scans have low SNR. The application of the Radon transform can significantly increase the detection probability in a pattern recognition procedure as it allows the detection of the straight line segments from the image segment [1]. A priori knowledge of the moment of current on and off allows the image to be split into the segments containing only one or two straight line components of the pattern.

108
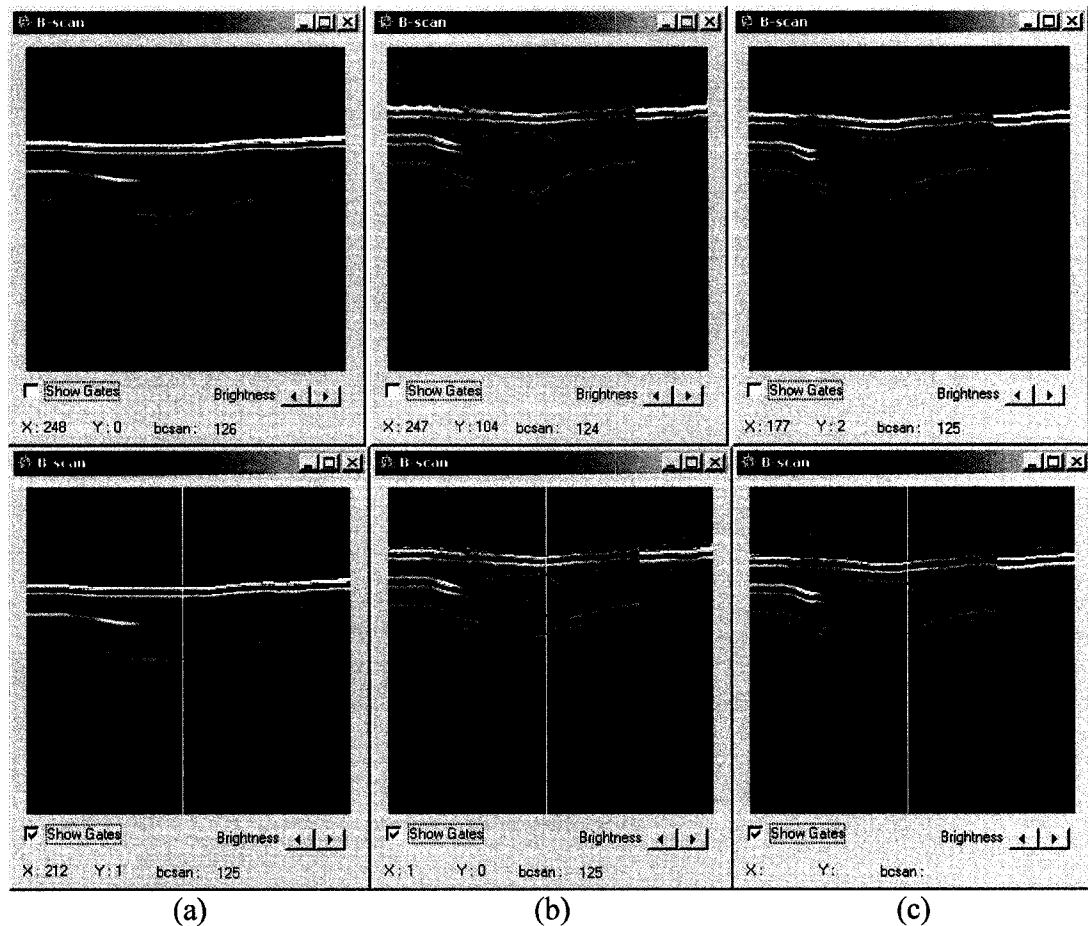
Figure 63. The ultrasonic B-scans of the welds and corresponding recognized patterns. (a) stick weld, no internal structure is detected; (b) good weld with both solid-liquid interfaces detected; (c) good weld with only one internal interface detected.

Figure 64 presents a sub-image of the bigger image acquired during ultrasonic real-time testing of resistance spot weld growth. The low-contrast tilted line in the center is the one that needs to be detected.

Figure 64. Example of the image segment with the low-contrast tilted line in the center.

109

If the image is gradually rotated around its center and projected on the fixed line, a set of projections at different angles is obtained. The projections can be put together one after another to form a two-dimensional picture. On the x-axis there is the degree of rotation; on the y-axis is the projection corresponding to that angle. Figure 65 (a) shows a square with a straight line at 22 degrees with respect to the negative y-axis. Numerically, the black background of the image is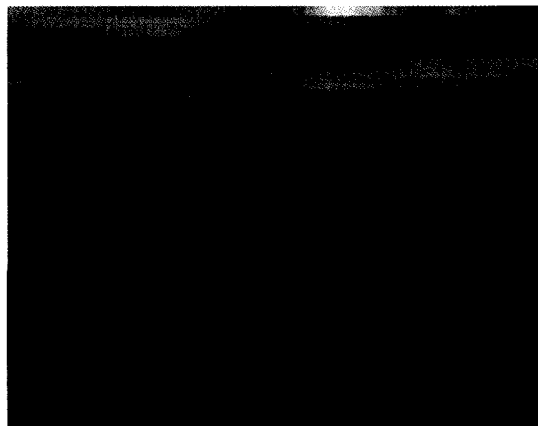 composed of zeros, and the line is composed of ones. Gradual rotation of this image clockwise around its center from 0 to 90 degrees and projection on the horizontal axis generates a Radon transform (RT) picture shown at Figure 65 (b). This transform shows a maximum at 22 degrees. The vertical axis is the projection whose length is $\sqrt{2}$ longer than the side of the square. The position of the maximum in the Radon transform allows the direction of the line (angle) in the image to be found. The position at the projection axis (y-axis) defines the distance, D, of the line from the center of the image, see Figure 65 (c). Projection of the image on the horizontal line (plane of projection) in this figure creates one vertical line of data of the RT. When image is rotated by an angle β, the transform will have a maximum corresponding to the strongest projection of the image line. Thus, the Radon transform can provide enough information to draw a line through the image along the discovered line.
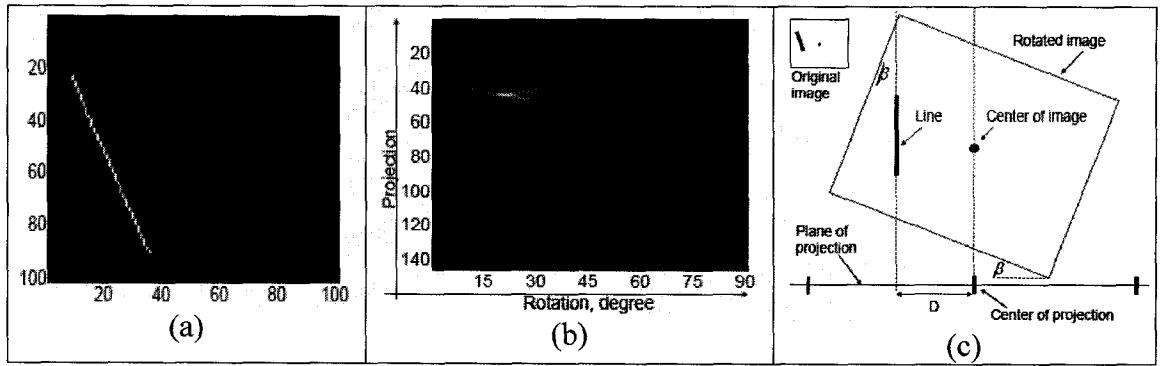
Figure 65. Explanation of the Radon transform principle. (a) image with the straight line; (b) Radon transform of the image; (c) schematic representation of the process of image rotation.

The Radon transform is defined as

$$R(p,\tau)[f(x,y)] = \int\limits_{-\infty}^{\infty}\int\limits_{-\infty}^{\infty} f(x,y)\delta[y-(\tau+px)]dydx, \tag{1}$$

where $f(x, y)$ is the image to process, p is the slope of a line, and τ is its intercept. Another way to get the same result is to apply the following equations:

$$R(\theta,x') = \int\limits_{-\infty}^{\infty} f(x'\cos\theta - y'\sin\theta, x'\sin\theta + y'\cos\theta)dy', \tag{2}$$

110

$$\begin{bmatrix} x' \\ y' \end{bmatrix} = \begin{bmatrix} \cos\theta & \sin\theta \\ -\sin\theta & \cos\theta \end{bmatrix} \begin{bmatrix} x \\ y \end{bmatrix}.$$ (3)

These formulas can be understood as performing the line integration along vertical directions (along every column) of the gradually rotated image [3]. The computer algorithm consists of two steps: rotation of the image and finding the "projection" of the rotated image on horizontal axis. The image should always be rotated around its center. If the image contains a straight line, the projection of the image when the line is perpendicular to the horizontal axis will have a strong maximum. The angle of rotation and the position of the maximum with respect to the image center are the two variables required to locate the line position in the image. These two variables are used to find a and b coefficients in the linear approximation equation

$$y = ax + b.$$ (4)

Figure 66 shows the gradually rotated image segment and its normalized projections on the horizontal axis at different angles of rotation. Projection of the straight line in the image is a maximum when this line is perpendicular to the horizontal axis. When the absolute maximum is found, the rotation angle is recorded. This angle will be used in calculations of the slope of the approximation line, a. The position of the peak with respect to the center of rotation of the image provides information needed to calculate the intercept b. These two coefficients provide enough information to locate the straight line (4) in the image segment, and then map it to the original image from which the image segment was taken.

111
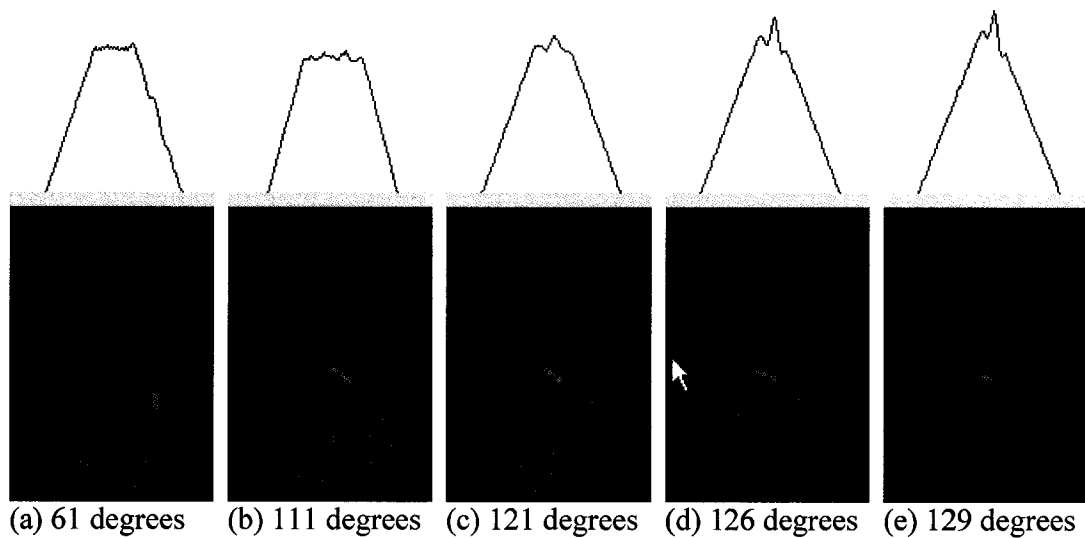
(a) 61 degrees   (b) 111 degrees   (c) 121 degrees   (d) 126 degrees   (e) 129 degrees

Figure 66. Rotated image segment (bottom) and corresponding normalized projections of the image on the horizontal axis (top).

Figure 67 represents the image segment and its Radon transform image in the range of 0-180 degrees. The point shown with the arrow is the location of the strongest or maximum projection found in the given angle range. From this image the straight line slope and intercept can be obtained. An example of the image with its recognized line segments is shown in Figure 68.
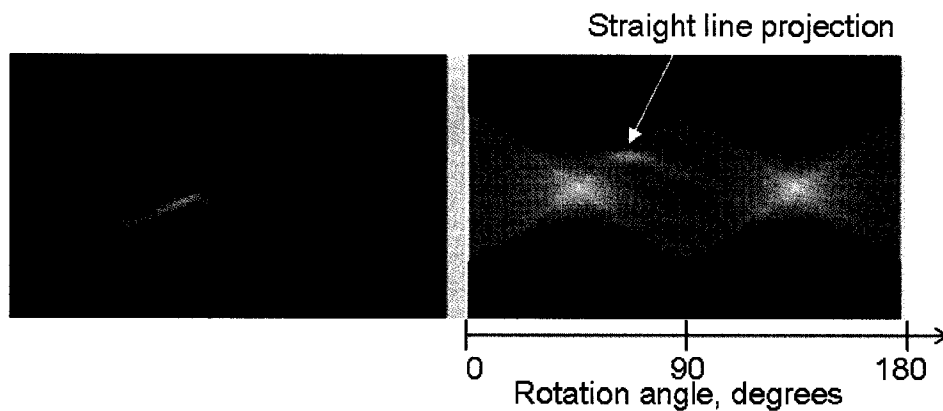

Figure 67. Image with line segment (left) and Radon transform image (right).
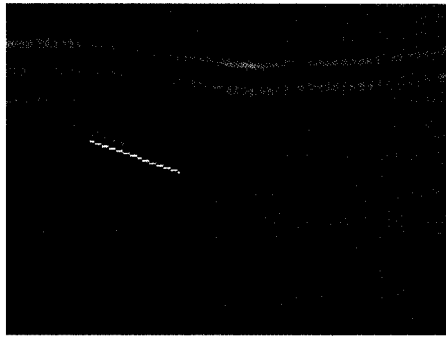
112

Figure 68. B-scan of the weld with the segments of lines located using Radon transform technique.

Once the pattern is recognized, weld interpretation needs to be performed. The idea of qualitative characterization of the process or the sample is not new. In this approach the exact measure of the quality in terms of specific numbers, such as nugget diameter, is not provided to the user. In many cases such a detailed quantitative characterization is not necessary and might be redundant or misleading. The qualitative interpretation would provide the exact nugget diameter of the weld such as 3.3 mm or 4.8 mm. In some cases it might be misleading when, for example, different thickness plates are welded at different spots. For different plate thicknesses, a 3.8-mm nugget might be either acceptable or unacceptable. An additional step is required to determine whether to call the weld good or bad. This step will be based on knowledge of the plate thickness and the minimum required button size.

Still, calling the nugget either good or bad is not the best approach. For example, suppose that the minimum acceptable nugget diameter is 4.0 mm. Further, suppose there are two welds measured 3.9 mm and 4.1 mm. The YES-NO system would call the first one bad and the second one good. But, there are errors in measurements, there are tolerances and there is common sense. The mechanical properties of the button of 3.9 mm and 4.1 mm might be identical or the smaller weld might be stronger. Should the first weld be called bad and the second good? Many inspectors on the production floor would call both of them good. There is an uncertainty in the measurements and based on statistical studies, the diameter prediction has a probabilistic nature. If, as in the present case, the standard deviation is 0.4 mm, the measurement of 3.9 mm can turn out to be 3.5 mm or 4.6 mm or any other value within the range of two standard deviations for 95% confidence.

The process of spot welding usually results in gradual weld diameter reduction due to the natural process of electrode tip degradation. As time advances and the electrodes

113

degrade, the spot welder begins to produce undersized welds. This is an undesirable situation that needs to be controlled. If the two-color (red-green) nondestructive system is installed on the spot welder, at a certain moment it will suddenly start calling the welds bad, see Figure 69.
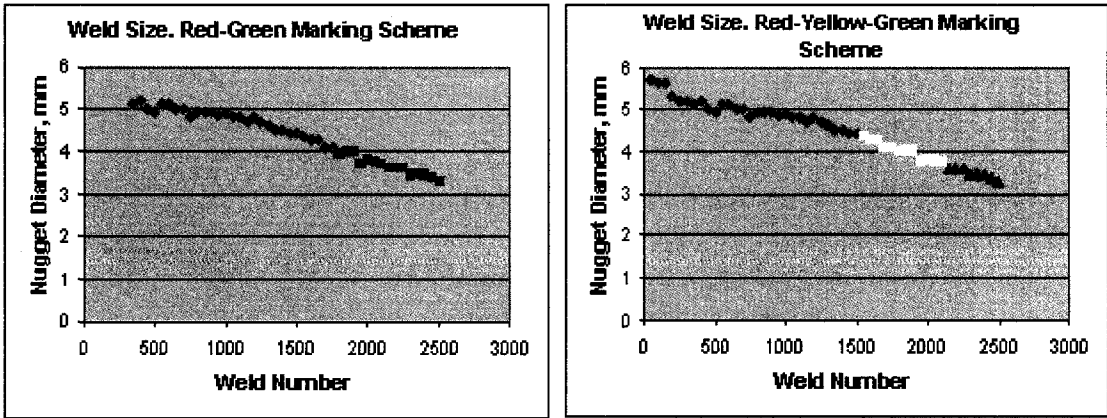
Figure 69. Two approaches of qualitative weld characterization. The diameter of 4.0 mm is the minimum size.

There is a need to introduce an intermediate quality, a "yellow zone" that will be a margin between good and bad welds. This will allow the operator time to react. If the number of "yellow" welds increases with time, this is a sign that the weld production is deteriorating and needs be adjusted before unacceptable welds are produced.

The width and location (center) of the yellow zone are defined by the measuring method precision and the given application. The Gaussian curve width on Figure 70 is defined by the standard deviation of the measurements. The location of the curve can be shifted by management to ensure a better identification of bad welds. This method results in a slightly higher level for the green zone.

Figure 70. Determination of the yellow zone. (a) centered at the minimum size; (b) shifted towards bigger size.

114

2. Fuzzy Logic for Weld Characterization

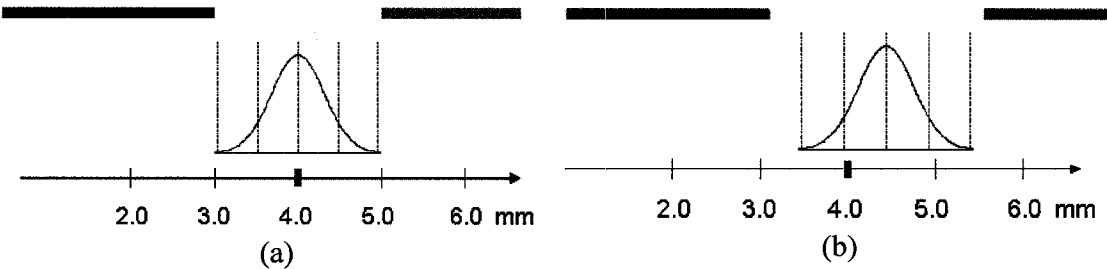The figures presented above provide a linear dependence of color as a function of size. As such, while the nugget size prediction increases, the colour moves from yellow closer to the green. Still the Gaussian curve is not linear which implies higher probability of the event at the mean point than away from the center of distribution. For example, when the prediction is 4.1 mm, the probability of an undersized weld (under 4.0 mm) is high. If prediction is 4.8 mm, this is most probably a good weld. But, both of these values are in the yellow zone, see Figure 70 (a). These two "yellow" measurements have a different "degree" of "yellow". One can say that the 4.8-mm measurement is much "greener" than the 4.1 mm measurement.

In order to resolve this fuzzy interpretation the fuzzy logic model was developed for better weld quality interpretation [4]. Fuzzy logic is a convenient way to map an input space to an output space. It is a very powerful tool for dealing quickly and efficiently with imprecision and nonlinearity. Fuzzy logic can be built on the experience of experts. In direct contrast to neural networks, which take training data and generate opaque, impenetrable models, fuzzy logic allows reliance on the experience of people who already understand the system.

In the general fuzzy logic approach, there are five parts to the fuzzy inference process: fuzzification of the input variables, application of the fuzzy operator (AND or OR) in the antecedent, implication from the antecedent to the consequent, aggregation of the consequents across the rules, and defuzzification.

The first step is to take the input (size prediction) and determine the degree to which it belongs to each of the appropriate fuzzy sets (red, yellow and green) via membership functions. In fuzzy logic, the input is always a crisp numerical value limited to the universe of discourse of the input variable (in this case the interval between 0 mm and 8 mm); the output is a fuzzy degree of membership in the qualifying linguistic set (always the interval between 0 and 1). Fuzzification of the input amounts to either a table lookup or a function evaluation.

The given approach is built on three rules, and each of the rules depends on resolving the input into a number of different fuzzy linguistic sets: the weld is bad, the weld is neither bad nor good and the weld is good. Before the rules can be evaluated, the

115

input must be fuzzified according to this linguistic set. The unaltered chart for fuzzification is presented on Figure 71.
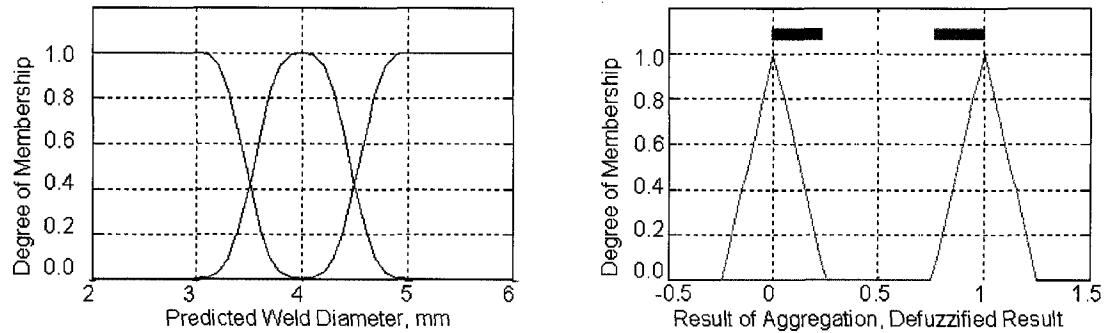
Figure 71. Fuzzification chart.

For example, to what extent is weld is good (green)? Figure 72 shows how well the predicted weld size, rated on a scale of 0 mm to 8 mm qualifies via its membership function as the linguistic variable "green". The membership function is taken in the form of a Gaussian curve. In this case, the weld diameter was estimated to be 3.7 mm; given the graphical definition of "red", "yellow" and "green", this value corresponds to μR = 0.1 for the red membership function and μY = 0.83 for the yellow membership. These two μ's are the result of fuzzification.

Figure 72. Fuzzification of the predicted number of 3.7 mm.

Figure 73. Fuzzification of the predicted number of 4.0 mm.

116

Figure 74. Fuzzification of the predicted number of 4.7 mm.

Figure 73 and Figure 74 present another two examples of fuzzification of the 4.0-mm and 4.7-mm weld size predictions. For the 4.0-mm prediction, the weld is called 100% yellow. For the 4.7-mm prediction the weld is qualified as 10% yellow and 83% green.
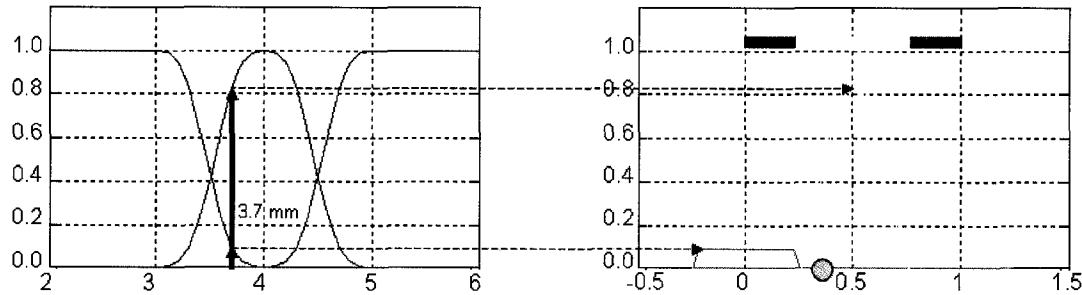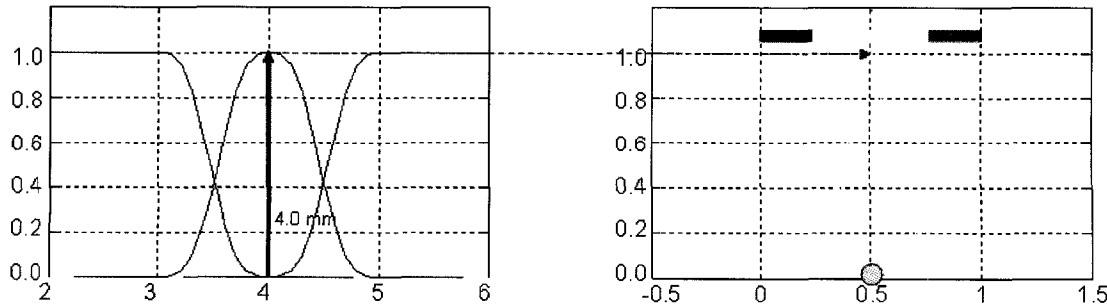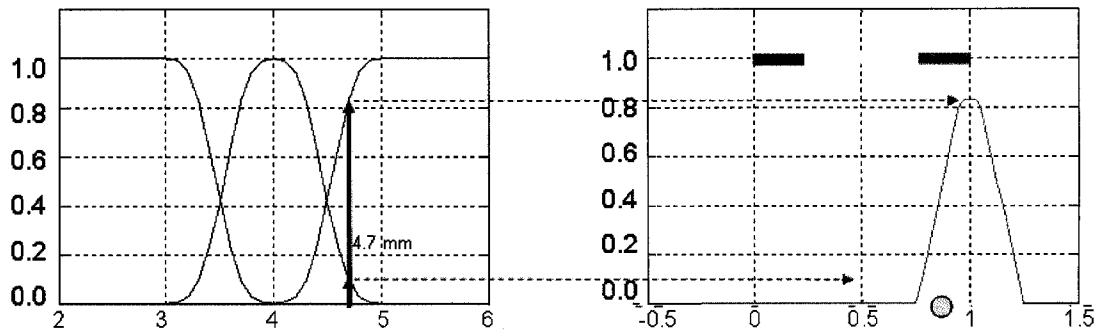
Once the inputs have been fuzzified, the degree to which each part of the antecedent has been satisfied for each rule is known. If the antecedent of a given rule has more than one part, the fuzzy operator is applied to obtain one number that represents the result of the antecedent for that rule. This number will then be applied to the output function. The input to the fuzzy operator is two or more membership values from fuzzified input variables. The output is a single truth value.

There can be, as is usually the case, more than one input to the fuzzy logic algorithm. Because decisions are based on testing all of the rules, the rules themselves must be combined in some manner in order to make a decision. Aggregation is the process by which the fuzzy sets that represent the outputs of each rule are combined into a single fuzzy set. Aggregation only occurs once for each output variable, just prior to the final step of defuzzification. The input of the aggregation process is the list of truncated output functions returned by the implication process for each rule. The output of the aggregation process is one fuzzy set for each output variable.

As long as the aggregation method is commutative, then the order in which the rules are executed is unimportant. The method used in this model is the sum – simply the sum of each rule's output set.

In the present case, the degree of liquid nugget penetration expressed as a percent of the plate thickness is the second input. Suppose that the penetration was measured to be 53%, and at the same time the size was predicted to be 4.0 mm (see Figure 73). Then, the

117

weld will be assigned a 100% green value according to the penetration and 100% yellow according to the size prediction based on the time-of-flight parameter, see Figure 75.
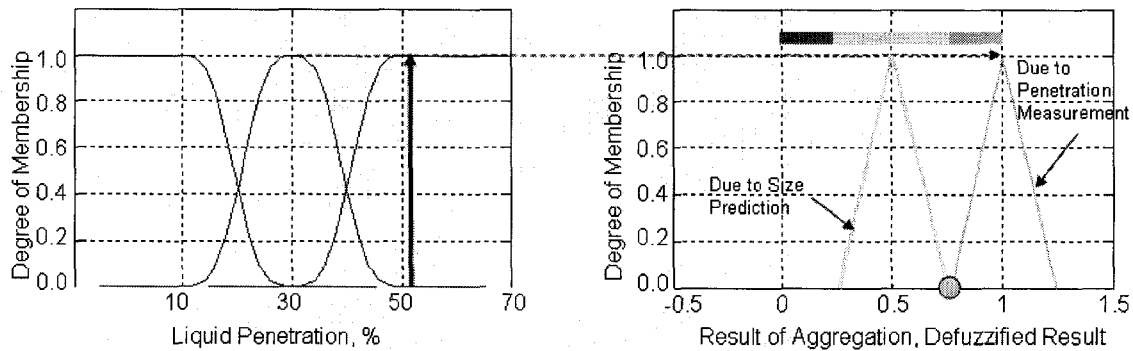

Figure 75. Fuzzification of the measured penetration; use of two input parameters.

The input for the defuzzification process is a fuzzy set (the aggregate output fuzzy set) and the output is a single number. As much as fuzziness helps the rule evaluation during the intermediate steps, the final desired output for each variable is generally a single number. However, the aggregate of a fuzzy set encompasses a range of output values, and so must be defuzzified in order to resolve a single output value from the set.

There are five defuzzification methods: centroid, bisector, middle of maximum or the average of the maximum value of the output set, largest of maximum, and smallest of maximum. The defuzzification method used here is the centroid calculation, which returns the center of area under the curve. Thus, based on the measurements of a 4.0-mm time-of-flight-based prediction, and 53% nugget penetration, the weld was classified at the level 0.75 on the 0 to 1 scale.

On the top of this scale, the red-yellow-green color coding is applied. In this case, the weld is still qualified as yellow as long as the centroid lies at 0.75 – exactly the border between the yellow and green. Here, the floor function is applied to be on the safe side and to not call a bad weld good.

If only time-of-flight based size prediction was used, then the prediction of a 3.7-mm size (Figure 72) would be called yellow, 4.0 mm (Figure 73) would be called yellow, and 4.7 mm (Figure 74) would be called green.

The performance of the two-parameter fuzzy algorithm based on both the time-of-light prediction and the penetration measurement is presented on Figure 76. Here, using the PC, all the possible values for size prediction and liquid penetration have been evaluated to generate a 3-dimensional surface of possible fuzzy logic outputs. Suppose, the weld was measured to be 3.8 mm using TOF, which is a little below the minimum.

118

The liquid penetration is measured at 25%. These two values will yield a red color according to the Figure 76. At the same time, if the measured penetration was increased to 80% for the 3.8-mm size, the weld will be called green. If penetration is 20%, but the size prediction is 5.5 mm, well above the minimum, the weld will not be called red but will be called yellow. The possible combinations of diameter and penetration are schematically presented in Figure 77.

Thus, such a system provides for a highly nonlinear decision making algorithm capable of mapping several inputs into a single output. 3, 4, or 10 input parameters can easily be employed and combined to characterize the weld quality.
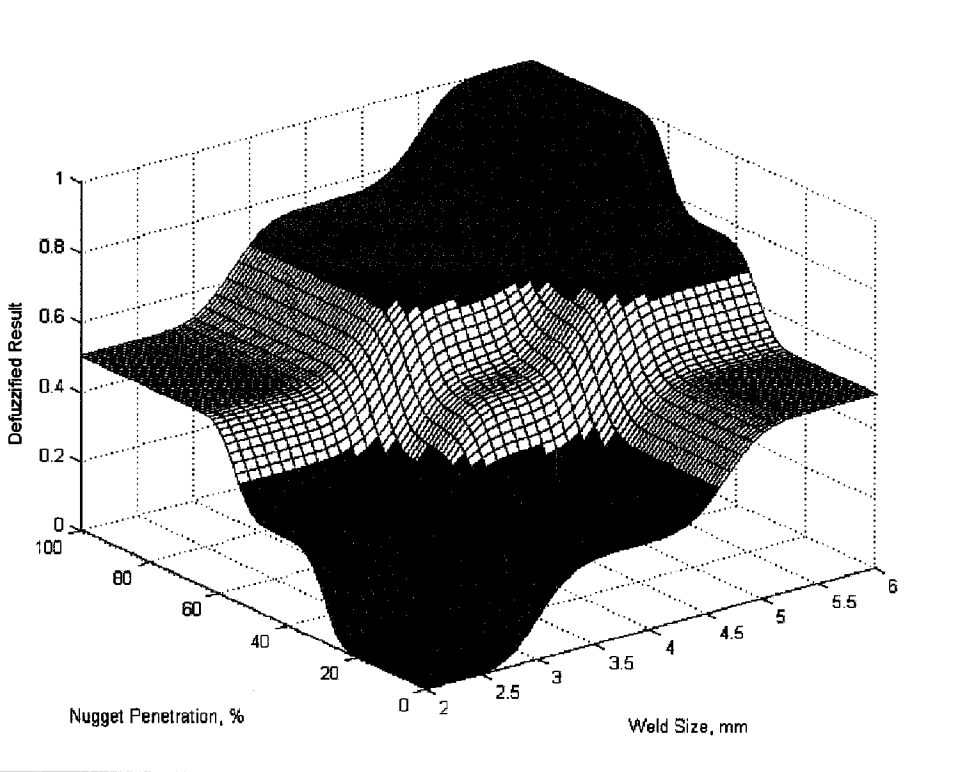
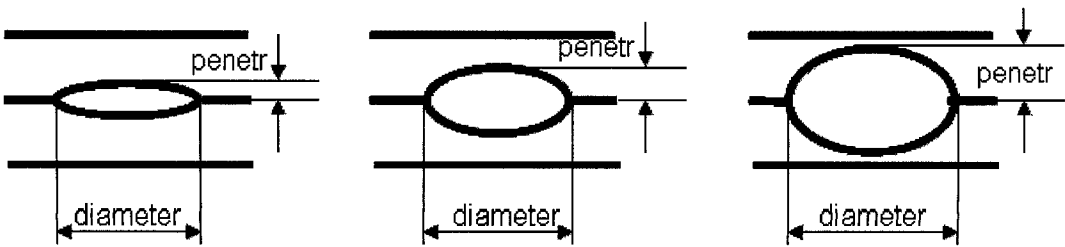Figure 76. Defuzzification with two-parameter input.

Figure 77. Schematic view of possible combinations of weld diameter and penetration level.

119

Conclusions

The use of red-yellow-green color characterization is intended to ease the process of decision making by the operator. It eliminates the stepwise discrimination between bad and good welds, which never occurs in reality. Qualification of one weld as good, and another only 0.01% smaller as bad, makes sense only for a machine with a strictly programmed threshold. But it makes little sense in actual production. For this reason, the yellow zone becomes a transition zone between good and bad welds.

If a set of parameters is provided like TOF prediction of weld size, liquid penetration, indentation degree, moment of melting start, and others, it will be difficult for humans to properly qualify the weld. Such multiparameter input is no problem for a machine, provided that the proper algorithm (like fuzzy logic described above) is implemented. The output in terms of three colors can be used by the welding operator to make a decision on the proper maintenance of the application. For example, if the green outputs begin to mix with yellows from time to time, then it would be appropriate to have a closer look at the machine during the next shift break. If suddenly the green switches to red – the weld application should be examined immediately.

The same concept can be implemented in a closed loop feedback algorithm. In this case, the machine will be trying to cure itself, trying to ensure production of good welds. Detection of "yellow" or "red" welds will trigger current or weld time increase for the following welds or other activities in the effort to improve the weld quality.

120

References

1. **A. Chertov**, R. Maev, *Extraction of Straight Line Segments from Noisy Images as a Part of Pattern Recognition Procedure.* Advances in Signal Processing for NDE of Materials. Aug 2-4 2005, University of Laval, Quebec city, Quebec, Canada.

2. **A.M. Chertov**, R.Gr. Maev, *Inverse Problem Solution to Find Real-Time Temperature Distribution Inside the Spot Weld Medium Using Ultrasound Time of Flight Methods..* Review of Progress in Quantitative Nondestructive Evaluation. 2003, pp. 1492-1498.

3. 16th World Conference on Nondestructive Testing held in August 30 – September 3 2004 in Montreal, Canada. *Determination of Resistance Spot Weld Quality in Real Time Using Reflected Acoustic Waves. Comparison with Through-Transmission Mode,* by **Andriy Chertov**, Roman Gr. Maev.

4. R.Gr. Maev, **A. M. Chertov**, L.Barsanti, G. Shu., *Real-Time Quality Monitoring of Resistance Spot Weld Using Integrated Ultrasonic Weld Analyzer (RIWA).* ASNT topical conference – Automotive Industry Advancements with NDT, May 16-17 2007, Dearborn, MI, USA.

CHAPTER VIII

Conclusions and Recommendations for Future Research and

Development

Dissertation Summary

Resistance spot welding is a common way of joining metal parts in industry. Quality monitoring of the joints is crucial for successful and reliable production. For this reason there is a high demand in industry for robust methods for the nondestructive testing of welds.

In this dissertation, a newly developed method of real time spot weld characterization was presented. The physical setup arrangement was described in detail in Chapter II. An ultrasonic transducer built into a weld gun electrode allows a real time B-scan of the weld to be obtained and the weld quality to be characterized. The features of the ultrasonic scan carrying the information are thoroughly investigated and explained.

The ultrasonic wave is modified by the multilayered structure of the spot weld. The constantly varying physical properties of the layers further alter the wave as it travels through the weld structure. The mechanisms and the means to counteract the effects of frequency-dependent attenuation and diffraction are considered in depth in Chapters III, IV, V and VI. Taking into account these effects increases the accuracy of the ultrasonic testing and constitutes an important part of proper signal processing.

Taking into account the aforementioned corrections, the B-scan is processed and used to extract important information using the pattern recognition procedure described in Chapter VII. Once the weld growth parameters are extracted, a fuzzy logic algorithm is employed for proper evaluation of the weld quality. A new red-yellow-green characterization scheme is presented, which both eliminates the stepwise discrimination between discrepant and good welds, as well as makes a more appropriate estimation from a common sense standpoint.

What was not Mentioned in the Dissertation

The research was conducted as a collaboration CRD project; significant work has been accomplished towards applying the developed physical concepts to industrial applications. The importance of this specific work is critically high for the overall project. Due to strong competition in the NDT field, some results are confidential and cannot be presented here. Still, a brief listing of the project achievements is presented below.

During my involvement in the research, I have developed special algorithmic/software techniques for signal and image processing needed at different stages during B-scan processing. The pattern recognition procedure for the given case requires different approaches and filtering techniques to extract separate elements from the image. The detection of the pattern and checking for correct recognition are also important elements, which are running behind the scenes in the processing software. A special PC board was developed, which is capable of generating and receiving electrical impulses for ultrasound signals, converting them into digital form, and sending them to the PC for further processing. The software for running this PC board was also developed by the research team. The transducer housing has passed through several designs and currently constitutes a state-of-the-art product from a mechanical engineering standpoint.

The installation of the prototype at a Chrysler assembly plant in Windsor, Canada was a great success for the entire team. Transition of the research project from the laboratory level to the industrial environment is a huge step for any R&D process. It is the most important part of the development after the invention of the technology. There is a great sense of pride in achieving this step as it involved the efforts of many people in many branches of science. Significant work was required in materials engineering, computer engineering, electronics engineering, and hardware design before the beta-version of the device became available for trials at the industrial floor. In its current state, the developed technology is a real-time quality monitoring system for spot welds.

Future Work

As a next logical step in the development of the system, the implementation of the closed loop feedback can be considered. Based on the quality monitoring results, the device would send a command to the weld controller to correct the welding parameters to

123

ensure the production of good welds. This is a promising approach as long as the weld growth can be monitored in real time. If the weld does not reach the required dimensions, the current or welding time can be adjusted.

Another possible implementation of the technology is as a smart machine for academic research for spot welding. Welding research institutions would be eager to have a device capable of looking inside metal plates during welding and revealing the processes taking place inside. A concept for this device is currently under development. On top of the existing monitoring system, the device will include sophisticated software capable of analyzing the physical processes occurring during welding. A specially developed finite element model will use the ultrasonic information to describe the actual processes in three dimensions. Parameters such as the rate of liquid growth and solidification, degree of liquid penetration into the plates, indentation formation, and integral degree of plate heating will be available for researchers in real time for the development of optimal welding regimes for new materials and welding processes.

124

Appendix A

MATLAB Program for Transducer Field Modelling

```
% Circular emitter.
% The radial field is being formed by the integration of fields of small parts of
% circular emitter. Due to symmetry only 1/2 of the circle is used.
% Pressure along radius and z-axis.


clear
R = 3.5;
side = 0.1;
Pressure = 1;
%---------------------- the first quadrant ------------------------
len = floor(R/side);
for x = 1:len
    for y = 1:len
        if (ceil(side*sqrt((len - y + 0.5)*(len - y + 0.5) + (x - 0.5)*(x - 0.5)))<=R)
            array(y, x) = 1;
        else array(y, x) = 0;
        end
    end
end
array = 128*array;
%---------------- Make semicircle from one quadrant ----------------------
semicirc = zeros(len, 2*len);
for i = 1:len
    for j = 1:len
        semicirc(i, j) = array(i, len - j + 1);
    end
end
for i = 1:len
    for j = (len+1):2*len
        semicirc(i, j) = array(i, j - len);
    end
end
%---------------------------------------------------------------------------

cnt = 1;
step = 1;
zmax = 250;
xx = -3:(zmax/step);
yy = (-87:88)*0.1;
lambda = 0.15;
k = 2*pi/lambda;
countZ = 1;
pressure = zeros(177, 153);
```

125

```
for z = 0:step:zmax
    sinpressure = zeros(1, 5*len+1);
    cospressure = zeros(1, 5*len+1);
    countRadx = 1;
    for radx = -1.5*len:3.5*len % covers the range -1.5..+1.5; shifted by +1 because of
semicirc coords;
        for y = 1:len
            for x = 1:2*len
                if (semicirc(y, x) > 1)
                    rhosq = side*side*((x-radx)*(x-radx) + (len-y+0.5)*(len-y+0.5));
                    dist = sqrt( rhosq + z*z );
                    sinpressure(countRadx) = sinpressure(countRadx) +
(Pressure/dist)*sin(dist*k);
                    cospressure(countRadx) = cospressure(countRadx) +
(Pressure/dist)*cos(dist*k);
                end
            end
        end
        pressure(countRadx, countZ+3) =
sqrt(sinpressure(countRadx)*sinpressure(countRadx)...
            + cospressure(countRadx)*cospressure(countRadx) );
        countRadx = countRadx + 1;
    end
    countZ = countZ + 1;
    z
end
figure;
gg = max(max(pressure));
pressure(60:118, 1:3) = gg/1.5;
h = imagesc(xx, yy, pressure);
set(gca, 'xtick', [0:20:160]);
set(gca, 'ylim', [-8.75 8.85]);
xlabel('Distance, mm');
ylabel('Lateral Dimension, mm');
```

126

Vita Auctoris

Name: Andriy M. Chertov

Place of birth: Simferopol, Ukraine

Date of birth: May 18, 1976

EDUCATION

- Summer 2003 began Ph.D. degree program in Physics at the Department of Physics and High Technology, University of Windsor (Canada).
- Master degree in Applied Physics. (2000-2003) from the University of Windsor (Canada), Department of Physics and High Technology.
- Electronics Engineer. Honors Bachelor degree (1993-1998) from Sevastopol State Technical University (Ukraine), Department of Microelectronics and Semiconductor Devices.
- Economics of Enterprise. Bachelor degree (1997-1999) from Sevastopol State Technical University (Ukraine), Department of Economics.

127